

POLITECNICO DI TORINO

Master of Science in Energy and Nuclear Engineering

Master of Science Thesis

**Numerical study of heat and mass transfers
in the reactor building of a PWR
during Design Basis Accidents**



Supervisor PoliTO

Prof.ssa Cristina Bertani

Supervisors ECL - LMFA

Prof. Christophe Corre

Ph. D. Cristina Ghitu

Candidate

Filippo Bentivegna

A.Y. 2020/2021

Abstract

The containment building for fission nuclear reactors represents the last confinement barrier against the release of fission products into the external environment in the event of an accidental situation. Therefore it is designed to withstand extreme mechanical and thermal loads corresponding to hypothetical accidents called Design Basis Accidents (DBA).

The DBA considered in this work is a Main Steam Line Break (MSLB) in a Pressurized Water Reactor (PWR): the break leads to the injection of superheated steam inside the reactor containment building causing an increase in the pressure and temperature of the building's atmosphere. In order to mitigate this increase and ensure the (eventual) removal of fission products, several safety systems and natural mechanisms can be considered. In this work, an active safety system and a passive safety mechanism are considered, respectively: the Containment Spray System (CSS) and the Condensation on the containment structures (Wall Condensation).

The main aim of this work is to develop Python codes to analyze the Heat and Mass (H&M) transfer mechanistic models for CSS and Wall Condensation (WC) and to perform a simulation of a MSLB including these models. The following three steps are followed:

1. Analysis of H&M transfer mechanistic models for the CSS based on the mass, energy and momentum balance equations applied to a single droplet of water in free fall in a gas mixture (air and superheated steam). The equations are solved numerically by developing Python codes and a parametric analysis is performed; the results are compared with numerical and experimental results presented in literature.
2. Analysis of H&M transfer mechanistic models for WC based on the calculation of heat fluxes (latent and sensible) exchanged between a gas mixture (air and superheated steam) and the walls of the containment building using correlations taken from the literature for the calculation of heat transfer coefficients.
3. Development of an H&M transfer model for a containment volume with steam injection (MSLB simulation) incorporating the models of CSS and WC. Mass and energy balance equations applied to the containment volume are solved numerically to simulate a MSLB-like scenario including the wall condensation phenomenon and the activation of the CSS (extending the single-drop approach to a multiple-drop approach to simulate spray injection in containment). Several results are presented to quantify the potential effectiveness of CSS and WC in mitigating the effects of the accident.

Keywords: containment building, DBA, MSLB, H&M transfer, CSS, wall condensation

Contents

Abstract	4
Contents	5
List of Symbol	10
Introduction	17
1 H&M transfers between the CSS drops and the atmosphere	19
1.1 Phenomena identification	19
1.2 Working perimeter	20
1.3 H&M transfer models	20
1.3.1 One-drop model	20
1.3.1.1 Heat transfers	21
1.3.1.2 Mass transfers	23
1.3.1.3 Momentum balance equation	26
1.3.2 Bestion-Lopez model	27
1.3.2.1 Conservative approach	27
1.3.2.2 Mechanistic approach	28
1.4 Implementation	32
1.4.1 One-drop model	32
1.4.1.1 Input parameters	32
1.4.1.2 Definition of constants	32
1.4.1.3 Loops on the input parameters	32
1.4.1.4 Initialization of the variables	33
1.4.1.5 <i>While</i> loop for the one-drop H&M transfers during the fall	34
1.4.2 Bestion-Lopez model	35
1.4.2.1 Initialization of the energy balance at the interface	35
1.4.2.2 Drop balance equations time discretization	35
1.4.2.3 Calculation of the interface temperature	36
1.5 Validation of the models	36
1.5.1 One-drop model: parametric analysis	36

1.5.2	Bestion-Lopez model	42
1.5.3	Comparison with ISRN CARAIDAS experimental results	43
1.5.3.1	Comparison 1	43
1.5.3.2	Comparison 2	47
1.5.3.3	Uncertainty quantification one-drop model	50
1.6	Spray repartition maps	52
1.6.1	Definition of spray repartition	52
1.6.2	Input parameters and case study	53
2	H&M transfers between the structures and the atmosphere	59
2.1	Review of key physical phenomena	59
2.1.1	Liquid film component	61
2.1.2	Diffusive gas boundary layer component	61
2.1.3	Bulk flow	62
2.1.4	Geometric configuration	63
2.2	Working perimeter	63
2.3	H&M transfers models	63
2.3.1	Mechanistic model: Chilton and COPAIN correlations	63
2.3.1.1	Chilton correlation	65
2.3.1.2	COPAIN correlation	65
2.3.2	Historical model: Tagami and Uchida correlations	66
2.4	Implementation	68
2.5	Validation of the models	69
2.5.1	Delhaye problem	69
2.5.2	Benteboula-Dabbene: Test-1	73
2.6	Condensation ratio maps	78
2.6.1	Definition of condensation ratio	78
2.6.2	Input parameters and case study	78
3	Containment H&M transfers model	83
3.1	OD containment model for a LOCA with spray system and wall condensation	83
3.1.1	Configuration 0: no spray, no wall condensation	84
3.1.1.1	Mass conservation	84
3.1.1.2	Mass and molar fractions	85
3.1.1.3	Pressure in the containment	86
3.1.1.4	Energy conservation	86
3.1.1.5	Steam described by the IAPWS tables	87
3.1.2	Configuration 1: no spray, with wall condensation	88
3.1.2.1	Preliminary remarks	88
3.1.2.2	Mass conservation	88
3.1.2.3	Energy conservation	89
3.1.2.4	System to solve	90
3.1.3	Configuration 2: with spray, with wall condensation	90
3.1.3.1	Mass conservation	90
3.1.3.2	Energy conservation	91
3.1.3.3	System to solve	92
3.2	Comparison with literature	93

3.2.1	Delhaye problem	93
3.2.2	Benteboula-Dabbene: Test-1	94
3.2.2.1	Chilton and COPAIN correlations	94
3.2.2.2	Tagami and Uchida correlations and condensation ratio maps	95
3.3	Main case study: MSLB simulation with spray activation and wall condensation	96
3.3.1	Mechanistic models for spray and wall condensation	98
3.3.2	Historical (conservative) models for spray and wall condensation using the 92/8 repartition	102
3.3.3	Historical models for spray and wall condensation using the MAPS	106
	Conclusion	114
	A Derivation of mixture model equations	115
	Bibliography	117
	Acknowledgements	120

List of Symbol

Acronyms

ALARA	As Low As Reasonably Achievable
APWR	Advanced Pressurized Water Reactor
BWR	Boiling Water Reactor
CSS	Containment Spray System
DBA	Design Basis Accident
DiD	Defence in Depth
DOE	Design Of Experiments
EAS	Enceinte Aspersion Système (corresponding to CSS in French nomenclature)
EoS	Equation of State
EPR	European Pressurized Reactor
FBR	Fast Breeder Reactor
H&M	Heat and Mass
HTC	Heat Transfer Coefficient
IAPWS	International Association for the Properties of Water and Steam
LOCA	Loss-Of-Coolant Accident
LWR	Light Water Reactor
MSLB	Main Steam Line Break
NRC	Nuclear Regulatory Commission
PAHR	Post Accident Heat Removal
PARR	Post Accident Radioactivity Removal
PCE	Polynomial Chaos Expansion
PDF	Probability Density Function
PG	Perfect Gas
PWR	Pressurized Water Reactor
RCS	Reactor Cooling System
RPS	Reactor Protection System
SG	Steam Generator
SMR	Small Modular Reactor
UQ	Uncertainty Quantification
WC	Wall Condensation

Introduction

Nuclear fission reactors

A nuclear fission reactor is a device capable of starting and controlling a fission nuclear chain reaction. It is mainly used at nuclear power plants (thermal power stations in which the heat source is a nuclear reactor) for electricity generation. Heat from nuclear fission is passed to a working fluid (water or gas), which in turn runs through steam turbines connected to a generator that produces electricity.

The thermal energy generated in the reactor is converted into electrical energy through an indirect process, as in conventional thermal power stations: the fission reactions that take place in the reactor core heat up the reactor coolant (water or gas, or even liquid metal, depending on the type of reactor), which in turn goes to a steam generator and heats water to produce steam. The pressurized steam is then usually fed to a multi-stage steam turbine that expands and partially condenses the steam, then the remaining vapor is condensed in a condenser that works as a heat exchanger which is connected to a secondary side such as a river or a cooling tower. The water is then pumped back into the steam generator and the cycle begins again. The water-steam cycle corresponds to the Rankine cycle.

The most widely used nuclear reactor for electricity production is the Pressurized Water Reactor (PWR), whose simplified design is shown in figure 1.

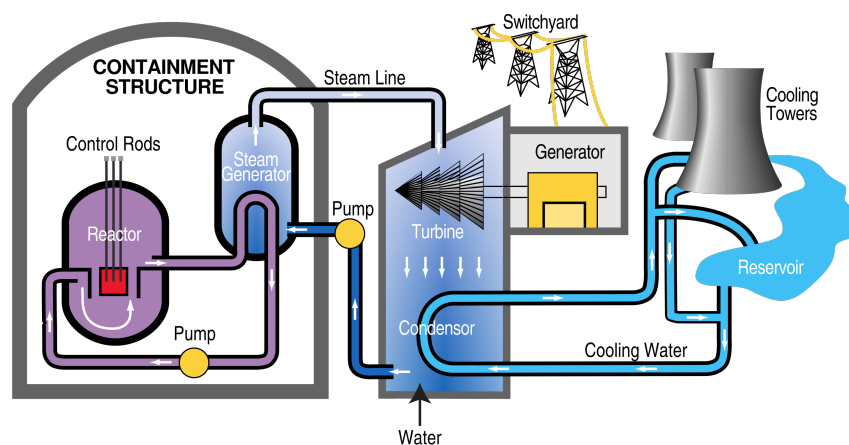


Figure 1: PWR nuclear power plant diagram. [Wikimedia Commons]

The main characteristic of a PWR is that it has two separate circuits: the primary circuit in which pressurized liquid light water flows, with the dual purpose of cooling the reactor core and moderating the fission reactions; the secondary circuit, also fed by water, which this time is converted into steam inside a Steam Generator (SG) to feed the turbines. The two circuits come into (non-direct) contact within the SG where the primary fluid transfers the heat extracted from the reactor core to the secondary fluid, causing it to evaporate. From a safety point of view, this configuration has the advantage that, in the event of a release of fission products, only the fluid in the primary circuit is contaminated, assuming the SG is intact.

Another widespread type of nuclear reactor is the Boiling Water Reactor (BWR), in which there are not two separate circuits as in the PWR, but a single circuit which, as its name suggests, allows the water to boil once it has passed through the core of the reactor and to convert into steam within the circuit itself. It can be said that in this case the SG's task is carried out directly by the reactor itself. The simplified design of a BWR is shown in figure 2.

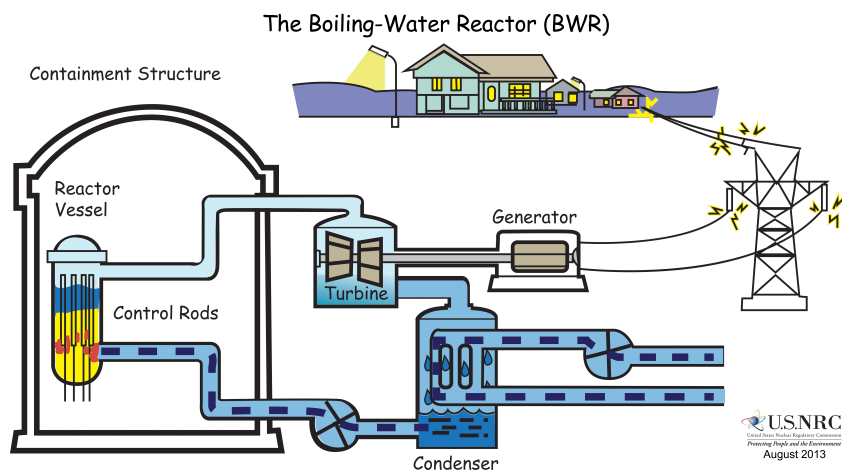


Figure 2: BWR nuclear power plant diagram. [Wikimedia Commons]

Thus, PWRs and BWRs are the most widespread type of reactor to date and belong to the category of reactors known as Generation I and II. In order to improve the safety, cost-effectiveness and ease of construction of nuclear power plants, new types of reactors, known as Generation III and III+, are now being designed and studied, e.g.: Advanced PWR (APWR, like Westinghouse AP600 and AP1000), European Pressurized Reactor (EPR). In addition, research is developing further advanced Generation IV reactors, the main innovations of which are the use of alternative coolants to water (liquid metals, gases or molten salts) and the further improvement of passive safety. Examples of this type of reactor are Fast Breeder Reactors (FBR) and Small Modular Reactors (SMR).

For reference purposes, a brief description of the AP1000 reactor and SMR is given below.

The AP1000 (upgraded version of the AP600) is a two-loop APWR with approximately 1154 MW of electrical power output. The safety systems focus on the passive safety of the reactor and simplification in terms of safety and construction, which allows high safety coefficients without the need to use generators in the event of a power failure from outside (as is necessary today to ensure power supply to internal systems). In the event of an accident, the reactor does not require the intervention of an operator for a long period, which means that the possibility of human error in an emergency is very low, and also gives time for the mobilisation of assistance from outside the plant.

The SMR is a type of nuclear fission reactor which is smaller than conventional reactors, allowing them to be manufactured at a plant and brought to a site to be assembled. They allow for less on-site construction, increased containment efficiency, and enhanced safety due to passive nuclear safety features.

Safety of nuclear power plants

The main purpose of nuclear reactor safety is to minimize the possibility of fission products being released into the external environment in case of an accidental event, following the *As Low As Reasonably Achievable* (ALARA) principle.

The term *Defence in Depth* (DiD) summarises the philosophy behind the design of nuclear plants expressed through three (or more) levels of safety, which are often not entirely independent, indeed they are mutually reinforcing, but are generally useful in establishing the successive stages that must be put in place before there is an accident affecting the health of the public. The **first level** of safety consists in *preventing the accidents*: the design must be at such a level of quality (both for the system as a whole and for the individual components and materials) that the system has a high degree of reliability and a low probability of failure, once built and in operation; the design must be inherently stable and have a high tolerance for abnormal conditions. The **second level** deals with *protection*: if, however, faults and malfunctions do occur, the plant must be able to report them in good time and cope with them with its instrumentation and protection systems, which, by intervening, restore normal operating conditions; these protection systems must be continually checked to ensure that, if required, they function correctly; conservative design, serviceability, redundancy are characteristics of a reliable protection system. The **third level** is the *mitigation*: it is complementary to the other two and replaces them in the event of an unlikely but more serious accident involving significant damage to the core, mitigating its effects; this involves analyzing the plant's response to a large number of hypothetical events, with the additional assumption of a failure of the redundant core protection system; the plant must be provided with equipment to mitigate the accident, further protecting the population; from these events, a number of accidental chains are chosen to form the group of **Design Basis Accidents** (DBA), meaning that they form the basis for incorporating additional systems for public health safety; the potential consequences of such accidents are analyzed conservatively to determine the adequacy of systems to mitigate the effects; mitigation also includes all emergency actions (as set out in the so-called emergency plans) to be taken by the political authority to mitigate the effects of the spread of a radiotoxic substance (and this applies to all toxic substances) in the territory.

According to US regulations, the following four physical **containment barriers** to the release of radioactivity can be identified for Light Water Reactors (LWRs), such as PWRs and BWRs: the ceramic uranium dioxide (UO_2) pellets are the **first barrier**; in normal operation they retain about 98% of the radioactivity of the fission products; noble gases (Krypton and Xenon) and Iodine tend to be released slowly; the **second barrier** is the Zircaloy cladding; despite the care taken in the design and construction of the fuel rods and the checks carried out during operation, the cladding can occasionally crack slightly, especially towards the end of the life of the fuel element, releasing small quantities of radioactive gases into the refrigeration fluid of the primary circuit, which must be continuously monitored and controlled by the appropriate chemistry control systems; the **third barrier** is the primary circuit; if the radiation detectors reveal too high radioactivity level in the coolant, it means that too many fuel rods have lost

their integrity and the reactor must be stopped and replaced; minor leaks from the primary circuit, valves and seals may occur, in which case the liquid is drained and treated to reduce radioactivity; if, on the other hand, the loss is significant due to a breakage, i.e. if the integrity of the third barrier is lost, the **fourth barrier** comes into operation; the latter barrier is the containment building, which must contain the gases and vapours, even under pressure, and minimise their escape to the outside environment; the containment can also be double. These barriers are passive safety systems, as they operate without the need for any actuation requiring a power source or moving parts. However, they can lose their integrity; the design of the entire reactor system and safety engineering safeguards must make such loss of integrity unlikely, with decreasing probability from the first to the last barrier.

The safety of a plant is not limited to the study of the serious and unlikely DBAs. Also the most serious accidents, named *severe accidents*, have been the subject of studies and research in order to improve the protection of the plant also in case of the most serious accidents and understand phenomenologies and evaluate probabilities of these accidents so that better evaluations of the global risk of a plant can be performed.

Accidents are usually grouped as follows: accidents of internal or external origin; area accidents (fires, internal floods); accidents of natural origin; accidents of human origin (sabotage, explosion of a tank near the plant, etc.); Design Basis Accidents, Beyond Design Basis Accidents, Severe Accidents.

DBAs are usually subdivided into 4 categories: *Operational transients (category 1)*, where operating conditions may occur frequently or regularly during reactor operation, refueling or maintenance (e.g. occasional and limited fuel elements ruptures, fast load changes, etc.); *Moderate frequency sequences (category 2)*, that are incidental events that do not occur ordinarily during the plant operation, but that can reasonably occur during the life of a plant (e.g. inadvertent withdrawal or misalignment of control rod assembly, loss of main feedwater to SGs, etc.); *Rare sequences (category 3)*, that represent accidental conditions that are not believed to occur during the life of a single plant, but that can occur in the nuclear industry in a time period of 30-40 years (e.g. small break in the primary or secondary circuit, forced reduction in the reactor coolant flow, etc.); *Limiting accidents (category 4)*, that include events whose probability is so low that they are not expected in the nuclear industry over 30-40 years.

DBAs belonging to **category 4** can cause significant damages in the plant and radioactivity can be released to the external environment, but the amount of released radioactivity must be lower than the limits fixed by regulations, since they could cause severe damages to population. They represent a limiting case, notwithstanding their very low likelihood, and require safety systems. The main accidents in this category are as follows: Main Steam Line Break (MSLB), Main feedwater line break, Reactor coolant pump locked rotor, Loss-Of-Coolant Accident (LOCA) up to and including double-ended guillotine failure of largest Reactor Cooling System (RCS) pipe, etc.

The main **safety system** for LWRs is represented by the Reactor Protection System (RPS). This system is dedicated to shutting down the chain of fission reactions using Control Rods. These rods, which can be made of metals such as silver, cadmium, indium or silicon carbides, are inserted as required in alternation with the fissile fuel rods, for example to modulate the power output of the reactor. In practice, they act by capturing the neutrons released by fission and thus also controlling any unstable chain reactions during the entire process of creating energy by transmutation. They can eventually stop the fission process in the event of a criticality, making them a primary safety mechanism in the reactor.

Other main **engineering safeguards** are:

- Residual Heat Removal System (RHRS);
- Emergency Core Cooling System (ECCS);
- Emergency power supply system;
- Containment system, which includes the containment building itself, the Containment Spray System (CSS), the Post Accident Heat Removal System (PAHR), the Post Accident Radioactivity Removal System (PARR), etc.

MSLB inside the containment building

The work proposed here deals with the numerical modeling of containment thermal-hydraulics related phenomena. The containment thermal-hydraulics domain covers the study of the fluid mechanics and thermodynamics phenomena occurring in the containment building during normal operation as well as during accident conditions.

The containment building for fission nuclear reactors represents the last confinement barrier against the release of fission products into the external environment in the event of an accidental situation. Therefore it is designed to withstand extreme mechanical and thermal loads corresponding to hypothetical accidents (DBAs).

The DBA considered in this work is a MSLB in a PWR: the break leads to the injection of superheated steam inside the reactor containment building causing an increase in the pressure and temperature of the building's atmosphere. The pressure and temperature evolution in the reactor building are driven by 3 main phenomena:

- Liquid-vapor separation at the break (flashing);
- Heat and Mass (H&M) transfers between the atmosphere and the containment structures;
- H&M transfers between the atmosphere and the CSS drops.

The work proposed in this Master thesis is a numerical study of the two latter main phenomena occurring in the reactor building during a MSLB, namely H&M transfers between the atmosphere and the containment structures and H&M transfers between the atmosphere and the CSS drops. The liquid-vapor separation at the break is not addressed in this work. Conditions of a MSLB are used, so that the fluid coming from the break is in the vapor phase (steam). Detailed description of the containment thermal-hydraulics domain and the associated phenomena can be found in [1].

In order to mitigate the pressure and temperature increase in the containment building and ensure the (eventual) removal of fission products, several safety systems and natural mechanisms can be considered. In this work, an active safety system and a passive safety mechanism are considered, respectively: the CSS and the Condensation on the containment structures (Wall Condensation).

The CSS is an engineered safety features system that maintains containment building integrity, helps to maintain containment sump pH neutrality, and cools the containment building recirculation sump water. Containment integrity is assured by a reduction in building pressure. The reduction in containment building pressure is achieved by condensation of the steam released from the reactor coolant system during a LOCA or from the SG during a MSLB by the spray droplets from the containment spray nozzles (see figure 3).

The containment building's atmosphere is composed of air only before the accident and a mixture of air and superheated steam afterwards. The main steam line of a PWR is located in its secondary circuit at the outlet of the steam generator, that is the component in which the fluid circulating in the primary circuit (circuit in which the pressurized liquid water circulates through the core of the reactor, therefore potentially contaminated by fission products) transfers its heat to the water circulating in the secondary circuit, causing the latter to vaporize. The two fluids exchange heat through a tube bundle and therefore never come into direct contact unless there is a break in the tube bundle. It can therefore be reasonably assumed that, under normal conditions, the secondary circuit fluid is not contaminated by fission products. Consequently, in this work it is assumed that the superheated steam released through the MSLB is not contaminated by fission products, but the mechanical and thermal loads on the containment building still remain an issue to be addressed and mitigated.

As superheated steam is injected into the containment, a so-called **superheated atmosphere** (mixture of air and superheated steam) is generated. Subsequently, with the interruption of steam injection and the action of mitigation systems, the atmosphere will return to saturation conditions. The atmosphere can be defined as superheated when the temperature of the gas mixture T is higher than the saturation temperature at the steam partial pressure $T_{\text{sat}}(P_{\text{steam}})$. The **superheating degree** of the atmosphere can be defined as $\Delta T_{\text{sat}} = T - T_{\text{sat}}(P_{\text{steam}})$, so that if $\Delta T_{\text{sat}} > 0$ the atmosphere is superheated, while if $\Delta T_{\text{sat}} = 0$ the atmosphere is saturated.

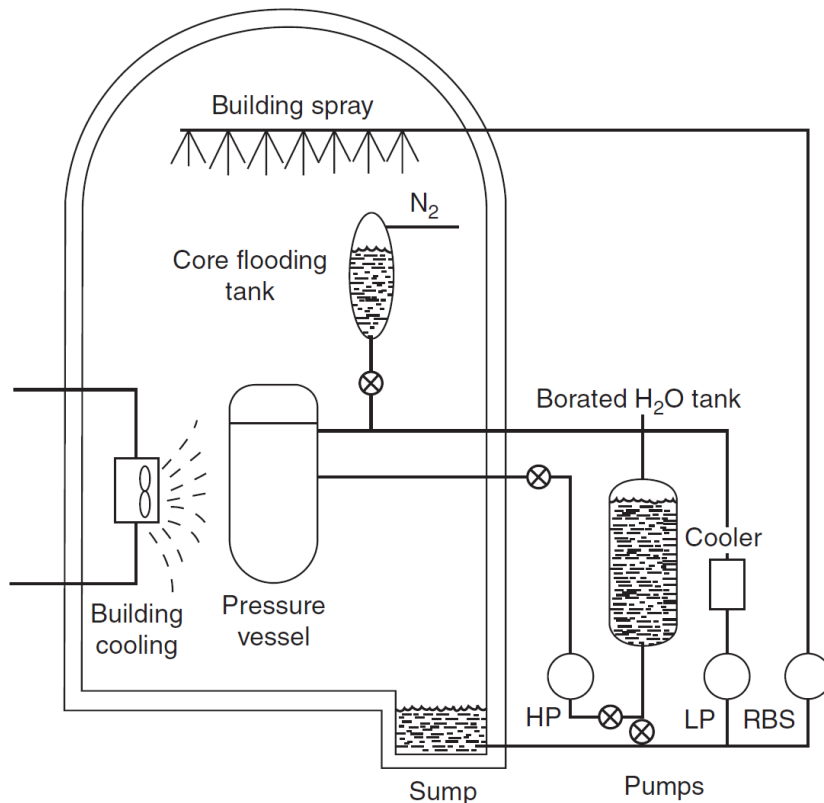


Figure 3: Emergency core cooling system. Pumps: HP, high pressure; LP, low pressure; RBS, reactor building spray. [2]

The main aim of this work is to develop Python codes to analyze the Heat and Mass (H&M)

transfer mechanistic models for CSS and Wall Condensation (WC) and to perform a numerical simulation of a MSLB including these models. The following three steps are followed, respectively developed in the three chapters of the work:

1. Analysis of two H&M transfer mechanistic models for the CSS based on the mass, energy and momentum balance equations applied to a single droplet of water in free fall in a gas mixture (air and superheated steam): One-drop model and Bestion-Lopez model [3]. The equations are solved numerically by developing Python codes and a parametric analysis is performed; the results are compared with similar results presented in [3] and with the IRSN CARAIDAS experimental data showed in [4]. An Uncertainty Quantification (UQ) analysis is carried out on the One-drop model, using the data on the uncertainty of the initial droplet diameter provided in [4]. Since the heat exchange between the spray droplets and the atmosphere can be divided into two contributions, one latent (condensation/vaporization) and one sensible (conduction/convection/radiation), Spray repartition MAPS are finally constructed by means of one-way calculations on the One-drop model. These maps are a kind of look-up tables from which it is possible to derive the ratio between the latent contribution and the total contribution (latent + sensible) to the heat transfer for different sets of parameters that identify the thermodynamic condition of the containment atmosphere (total pressure, air partial pressure, superheating degree).
2. Analysis of H&M transfer mechanistic models for WC, based on the calculation of heat fluxes (latent and sensible) exchanged between a gas mixture (air and superheated steam) and the walls of the containment building using correlations taken from the literature for the calculation of heat transfer coefficients (Chilton and COPAIN [5]). The models are validated by implementing them in Python codes to reproduce two case studies found in the literature: Delhaye problem 11.2 [6] and Benteboula-Dabbene: Test-1 [5]. Where possible, the results obtained are compared with those presented in the articles mentioned. In addition to the mechanistic models mentioned, two historical models (Tagami and Uchida [5]) are also analyzed, whose approach is to calculate the total heat flux exchanged between the walls and the atmosphere using correlations for the calculation of the total heat transfer coefficient. Then this total heat flux can be split into latent and sensible contributions according to a conservative assumption proposed by the U.S. Nuclear Regulatory Commission (NRC) in [7]: in case of superheated atmosphere, it can be assumed that the 92% of the total heat flux is of latent nature and the remaining 8% is of sensible nature; while, in case of saturated atmosphere, the total heat flux can be entirely considered of latent nature. Finally, similar to the One-drop model, Condensation ratio MAPS are constructed.
3. Development of an H&M transfer model for a containment volume with steam injection (MSLB simulation) incorporating the models of CSS and WC. Mass and energy balance equations applied to the containment volume are solved numerically by developing Python codes to simulate a MSLB-like scenario including the wall condensation phenomenon and the activation of the CSS (extending the single-drop approach to a multiple-drop approach to simulate spray injection in containment). Several results are presented to quantify the potential effectiveness of CSS and WC in mitigating the effects of the accident.

Chapter 1

H&M transfers between the CSS drops and the atmosphere

Contents

1.1	Phenomena identification	19
1.2	Working perimeter	20
1.3	H&M transfer models	20
1.3.1	One-drop model	20
1.3.2	Bestion-Lopez model	27
1.4	Implementation	32
1.4.1	One-drop model	32
1.4.2	Bestion-Lopez model	35
1.5	Validation of the models	36
1.5.1	One-drop model: parametric analysis	36
1.5.2	Bestion-Lopez model	42
1.5.3	Comparison with ISRN CARAIDAS experimental results	43
1.6	Spray repartition maps	52
1.6.1	Definition of spray repartition	52
1.6.2	Input parameters and case study	53

1.1 Phenomena identification

In this part, it is proposed to set the framework of the problem studied and to make an inventory of the interactions between a drop of liquid in motion and its environment.

The interactions between the drops and their environment can be grouped together and broken down into several categories:

- forces;
- heat transfers;

- mass transfers;
- multiple drop phenomena.

This last category will be less developed because it represents a low overall impact compared to the nature of the problem posed and a high degree of complexity.

1.2 Working perimeter

This chapter defines the perimeter of the study in order to limit the physical domain that interests us in this chapter. To do this, we rely on the safety studies carried out, the geometric characteristics of the reactor buildings and the characteristics of the Containment Spray System (CSS, or *circuit d'Aspersion de Secours dans l'enceinte du bâtiment réacteur* (EAS) in French nomenclature, according to the French Nuclear Safety Authority (*Autorité de Sûreté Nucléaire*, ASN)) systems for the pressurized water reactors of the French nuclear power plants in operation.

Thermodynamic conditions of the gas phase of the reactor building in an accident situation are expected to be in the following ranges:

- the total (absolute) pressure is between 1 and 6 bar;
- the temperature of the gas phase is between 20 and 250 °C;
- the relative humidity is between 10 and 100 %.

Geometric characteristics of the area directly swept by spraying:

- the height of fall under the dome is between 20 and 30 m.

Characteristics of the enclosure spraying system:

- the spraying speed of the drops is between 10 to 30 m/s;
- the water temperature is between 7 and 100 °C, depending on the phase of the accident;
- the diameter of the drops is less than 2 mm.

1.3 H&M transfer models

This section presents the different theoretical models used to analyze the heat and mass transfers between the containment atmosphere and the CSS drops.

1.3.1 One-drop model

The one-drop model is a single-volume 0D model which considers the fall, due to gravity, of an individual liquid drop inside a gaseous mixture. In our case of interest, the drop is liquid water, while the gaseous mixture is composed by steam and air. The aim is to build a mechanistic model to analyze the H&M transfers between the drop and the surrounding atmosphere. This model will be implemented into a Python code.

1.3.1.1 Heat transfers

As mentioned previously, the temperature of the spray droplets is between 7 and 100 °C, while the temperature of the gas phase of the reactor building is between 20 °C (normal situation) and 250 °C (accidental situation). The temperature difference between these two fluids induces heat exchanges by conduction, convection and thermal radiation. In addition, in an accidental situation, the release of hot steam in the reactor building leads to a two-phase situation allowing a phase change for the water. The temperature difference between the spray droplets and the water steam therefore induces heat exchanges associated with the phase change. Under these conditions of pressure and temperature, two phenomena of phase change that can occur in the reactor building are identified: the condensation of steam on the droplets and the vaporization of the spray droplets.

Thus, a spray droplet can exchange heat with the gas phase by:

- Sensible heat transfer between the droplet and the gas phase, grouping together the conduction, convection and thermal radiation mechanisms;
- Latent heat transfer associated with the phase change, grouping together the condensation mechanisms for steam and vaporization for the droplet.

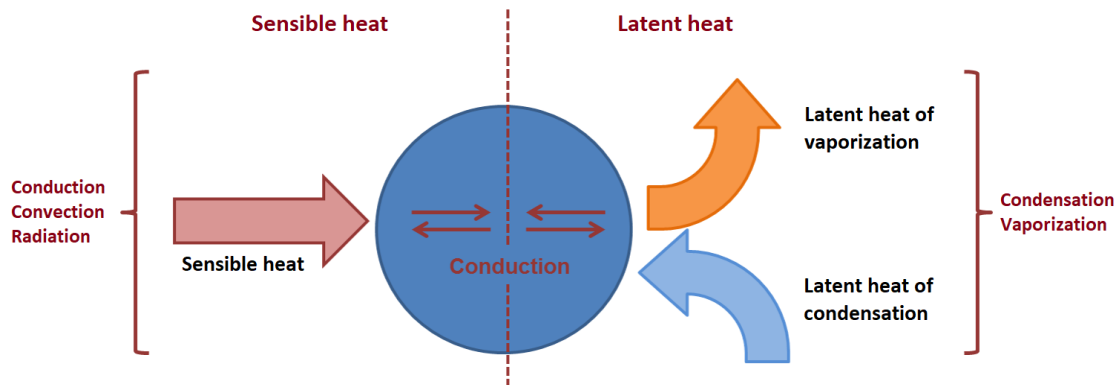


Figure 1.1: Illustration of the heat transfer mechanisms between a droplet and the gas phase, in the case of a cold spray or cooled by a heat exchanger.

Conventionally, latent heat transfers are defined as:

- The latent heat released by condensation of the steam on the surface of the droplet will be fully absorbed by the droplet;
- The latent heat used for the vaporization of the water in the droplet will be taken entirely from the droplet.

In the following, I propose to distinguish heat transfer at the interface of the droplet from heat transfers within the droplet.

Heat transfer within the drop

The temperature difference between the drop surface and the gas mixture is the driving term of the sensible heat transfer between the drop and the atmosphere. This difference also provides

information on the passage from the condensation on the drop to the vaporization of the drop. Here in the propagation of heat in the drop is analysed, in order to properly represent the temperature of the surface of the drop.

The heat conduction in the droplet is described by the heat equation:

$$\frac{DT}{Dt} - \alpha \nabla^2 T + \text{source term} = 0 \quad \text{with} \quad \alpha = \frac{\lambda}{\rho_d C_{p,d}} \quad (1.1)$$

where α (m^2/s) is the thermal diffusivity, λ ($\text{W}/\text{m}/\text{K}$) is the drop thermal conductivity, ρ_d (kg/m^3) is the drop (water) density, $C_{p,d}$ ($\text{J}/\text{kg}/\text{K}$) is the drop specific heat capacity at constant pressure.

Carrying out a dimensional analysis on the heat equation, taking into account the size of the droplets considered and the average height of delivery of the droplet in a reactor building, the conduction phenomenon in the droplets can be neglected. The temperature of the droplet can therefore be considered homogeneous during the entire falling time.

Heat transfers at the liquid/gas interface

We are interested here in the heat transfers due to the temperature difference between the gas phase and the surface of the drops. In this part it is assumed that the temperature of the surface of the drop is equal to the bulk temperature of the drop (i.e. we make the assumption that the conduction in the drop is instantaneous).

The heat transfer equation can be written as follows:

$$m_d C_{p,d} \frac{dT_d}{dt} = \text{sensible power} + \text{latent power} = hS(T_g - T_d) + \dot{m}_d h_{fg} \quad (1.2)$$

where m_d (kg) is the mass of the drop, $C_{p,d}$ ($\text{J}/\text{kg}/\text{K}$) is the drop specific heat capacity at constant pressure, T_d (K) is the temperature of the drop, h ($\text{W}/\text{m}^2/\text{K}$) is the total heat transfer coefficient between the drop and the surrounding atmosphere, S (m^2) is the surface of the drop, T_g (K) is the temperature of the gaseous mixture, \dot{m}_d (kg/s) is the total mass transfer flow rate, h_{fg} (J/kg) is the enthalpy of phase change.

According to the definition of the Nusselt number, the heat transfer coefficient between the droplet and the atmosphere can be expressed as follows:

$$h = \frac{\lambda_g Nu}{d} \quad (1.3)$$

where λ_g ($\text{W}/\text{m}/\text{K}$) is the thermal conductivity of the gaseous mixture, Nu (-) is the Nusselt number, d (m) is the diameter of the drop.

There are various correlations in the literature to calculate the Nusselt number in the case of a drop falling by gravity in a gas and carrying out mass and heat transfers with it.

The most widely used correlation is that established by Ranz and Marshall in 1952:

$$Nu = 2 + 0.6 Re_d^{1/2} Pr_g^{1/3} \quad (1.4)$$

$$Re_d = \frac{\rho_g v_d d}{\mu_g} \quad Pr_g = \frac{\mu_g C_{p,g}}{\lambda_g} \quad (1.5)$$

where Re_d (-) is the Reynolds number, Pr_g (-) is the Prandtl number of the gaseous mixture, ρ_g (kg/m^3) is the gaseous mixture density, v_d (m/s) is the relative velocity of the drop, μ_g ($\text{Pa} \cdot \text{s}$) is the gaseous mixture dynamic viscosity, $C_{p,g}$ ($\text{J}/\text{kg}/\text{K}$) is the gaseous mixture specific heat capacity at constant pressure.

1.3.1.2 Mass transfers

In an accidental situation, the presence of hot steam and cold liquid water droplets in the reactor building leads to latent heat transfers accompanied by mass transfers.

Under the accidental pressure and temperature conditions considered, two phase change phenomena can occur in the reactor building: the condensation of steam on the droplets and the vaporization of the spray droplets.

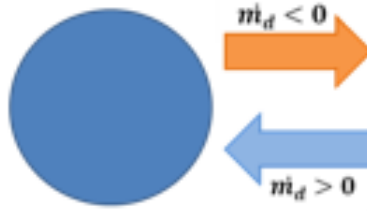


Figure 1.2: Illustration of the mass transfer mechanisms between a droplet and the gas phase.

Conventionally, mass transfers are defined so that:

- if the droplet loses mass, the mass flow will be negative.
- if the mass of the droplet increases, the mass flow will be positive.

The mathematical expressions for mass transfers between a drop and its environment can be written as follows:

$$\dot{m}_d = \pi d \cdot Sh \cdot D_v \cdot \rho_g \cdot H_M \quad (1.6)$$

where d (m) is the droplet diameter, Sh (-) is the Sherwood number, D_v (m^2/s) is the mass diffusivity of steam in the gaseous mixture, ρ_g (kg/m^3) is the gas mixture density, H_M (-) is the mass transfer “driving term”.

Sherwood number

There are several correlations in the literature allowing to calculate the Sherwood number in the case of a drop falling by gravity in a gas and carrying out mass and heat transfers with it.

The most used correlation is the one by Ranz and Marshall in 1952:

$$Sh = 2 + 0.6 \cdot Re_d^{1/2} \cdot Sc^{1/3} \quad (1.7)$$

$$Re_d = \frac{\rho_g v_d d}{\mu_g} \quad Sc = \frac{\mu_g}{\rho_g D_v} \quad (1.8)$$

where Sc (-) is the Schmidt number of the gaseous mixture.

Mass diffusivity

The diffusivity of the steam in the gaseous mixture plays a primary role in the mass transfer between the droplet and the atmosphere. So one is interested in its variation with the pressure and temperature conditions of the atmosphere in which the drop falls.

From kinetic theory of gases, at low and moderate pressures, binary diffusion coefficients in gas vary inversely with pressure or density and they are independent of the mixture composition [5]. The binary diffusion coefficient of one gas in another varies with pressure and temperature as follows:

$$D_v \propto \frac{T^b}{P} \quad (1.9)$$

In this work it is proposed to use three different formulations for the calculation of the diffusivity. They are resumed in table 1.1.

Table 1.1: Mass diffusivity

Model	Diffusivity
0	$D_{v-0} = (T_g^b/P) (P_{\text{ref}}/T_{\text{ref}}^b) D_{v,\text{air,ref}}$
1	$D_{v,g} = \frac{1}{\sum_j (X^j/D_v^j)}$ with $D_v^j(P, T_g) = \frac{a}{10^{-5}P} \left(\frac{T_g}{273.15} \right)^n$
2,3	$D_{v,\text{nc}} = \frac{1-X_v}{\sum_{j,j \neq v} (X^j/D_v^j)}$ with $D_v^j(P, T_g) = \frac{a'}{10^{-5}P} \left(\frac{T_g}{273.15} \right)^{1.75}$

-• **Model 0**

This model directly exploits the proportionality described in equation 1.9: finding in literature a reference value for the diffusivity of steam in air $D_{v,\text{air,ref}}$ one can calculate its values in any configuration of pressure and temperature.

With $b = 2.334$ in the case of steam and another non-polar gas. In this expression, the diffusivity D_{v-0} is in (cm²/s), the pressure P is in (atm) and the temperature T is in (K). $D_{v,\text{air,ref}} = 0.282$ cm²/s is obtained at $P_{\text{ref}} = 1$ atm and $T_{\text{ref}} = 25$ °C = 298.15 K.

Models 1 and 2,3 are both based on the evaluation of the mole fractions of steam X_v (-) and noncondensable (air) components X^j (-) and on the calculation of the binary diffusion coefficient D_v^j (m²/s), where j identifies the different noncondensable species. The mole fractions are determined at the bulk conditions. The pressure P and temperature T_g are expressed in (Pa) and (K), respectively.

-• **Model 1** [5]

This model includes steam in the gas mixture (steam self-diffusion) in addition to the noncondensables. The coefficients a and n associated to each species are reported in table 1.2.

Table 1.2

gas	H ₂ O	N ₂	O ₂
a	2.77×10^{-5}	2.27×10^{-5}	2.40×10^{-5}
n	0.0	1.75	1.71

-• **Model 2,3** [5]

This model does not include steam in the gas mixture (no steam self-diffusion, $j \neq v$), i.e. in the calculation of $D_{v,\text{nc}}$ we will not have the term X_v/D_v^v in the denominator, where

D_V^v is the diffusivity of the steam in itself. The coefficient a' associated to each species is reported in table 1.3.

Table 1.3

gas	H ₂ O	N ₂	O ₂
a'	2.78×10^{-5}	2.24×10^{-5}	2.28×10^{-5}

Mass transfer “driving term”

The term H_M expresses the imbalance between the properties of the steam near and far from the drop (steam pressure, mass fraction of the steam, density of the steam). This imbalance represents the “driving term” of mass transfer: the greater the imbalance, the greater the mass flow. If the imbalance no longer exists, there is no more mass transfer.

In this work, five models for the calculation of H_M are used (table 1.4).

Table 1.4

Model	Driving term
M0	$H_M = \ln\left(1 + \frac{\rho_{\text{sat}}(T_d, x=1) - \rho_{\text{steam}}}{\rho_{\text{sat,air}}}\right)$
M1	$H_M = \ln(1 + B_{M,\text{eq}})$ with $B_{M,\text{eq}} = \frac{Y_{s,\text{eq}} - Y_G}{1 - Y_{s,\text{eq}}}$
M3	$H_M = B_{M,\text{eq}}$
M5	$H_M = (Y_{s,\text{eq}} - Y_G)$
M9	$H_M = \frac{\rho_{\text{sat}}(T_g, x=1) - \rho_g Y_G}{\rho_g}$

The names of the models (M0, M1, M3, M5, M9) derive from the nomenclature used in [8], in which eight models for the calculation of H_M are presented and named from M1 to M8. Here it was chosen to use exactly the models M1, M3 and M5 from [8], so, to be consistent with the nomenclature, the baseline model is called M0 and the last model used, taken from [9], is called M9.

• Model M0

The driving term considered in this model is based on density gradients. In the formulation, $\rho_{\text{sat}}(T_d, x = 1)$ (kg/m³) is the steam density at the drop surface (saturation conditions, with x (-) the steam quality), ρ_{steam} (kg/m³) is the steam density away from the drop, $\rho_{\text{sat,air}}$ (kg/m³) is the air density at the drop surface.

In order to calculate $\rho_{\text{sat,air}}$ it can be assumed that the air behaves as an ideal gas and that the density of humid air remains constant:

$$\rho_g = \rho_{\text{steam}} + \rho_{\text{air}} = \rho_{\text{sat}}(T_d, x = 1) + \rho_{\text{sat,air}} = \text{constant}$$

From this assumption it can be written:

$$\rho_{\text{sat,air}} = \rho_g - \rho_{\text{sat}}(T_d, x = 1) = \rho_{\text{steam}} + \rho_{\text{air}} - \rho_{\text{sat}}(T_d, x = 1)$$

$$\rho_{\text{sat,air}} = \rho_{\text{steam}}(P_{\text{steam}}, T_g) + \frac{MW_{\text{air}}}{R} \frac{P - P_{\text{steam}}}{T_g} - \rho_{\text{sat}}(T_d, x = 1) \quad (1.10)$$

where P (Pa) is the total pressure of the gaseous mixture (steam + air) and it can be expressed as the sum of the steam partial pressure and the air partial pressure ($P = P_{\text{steam}} + P_{\text{air}}$), T_g (K) is the gaseous mixture temperature, T_d (K) is the droplet temperature, MW_{air} (kg/mol) is the molar mass of air, R (J/mol/K) is the universal gas constant.

-• **Models M1, M3, M5** [8]

These models are based on mass fraction gradients. In the formulations, $B_{M,\text{eq}}$ (-) is the equilibrium Spalding number, $Y_{s,\text{eq}}$ (-) is the equilibrium steam mass fraction at the droplet surface, Y_G (-) is the free stream mass fraction away from the droplet surface. They can be evaluated as follows:

$$Y_{s,\text{eq}} = \frac{X_{s,\text{eq}}}{X_{s,\text{eq}} + (1 - X_{s,\text{eq}})\theta_2} \quad X_{s,\text{eq}} = \frac{P_{\text{sat}}(T_d)}{P} \quad \theta_2 = \frac{MW_{\text{steam}}}{MW_{\text{air}}}$$

$$Y_G = \frac{X_G}{X_G + (1 - X_G)\theta_2} \quad X_G = \frac{P_{\text{steam}}}{P}$$

where $X_{s,\text{eq}}$ (-) is the equilibrium steam mole fraction at the droplet surface, X_G (-) is the free stream mole fraction away from the droplet surface, MW_{steam} and MW_{air} (g/mol) are the molar weights of steam and air, respectively.

-• **Model M9** [9]

This model, similarly to Model M0, is based on density gradients. It is obtained starting from M1, imposing $B_{M,\text{eq}} \rightarrow 0$, $Y_{s,\text{eq}} \rightarrow 0$ (limit cases).

1.3.1.3 Momentum balance equation

Considering the fall, due to gravity, of an individual liquid drop inside a gaseous mixture, the main forces acting on the drop are:

- Weight
- Archimedes' buoyant force
- Drag force

One must mention that some forces are neglected in the following development of the drop momentum balance equation: Lift force, Magnus effect, Basset force.

The drop momentum balance equation can be written as follows:

$$\frac{d\vec{p}}{dt} = \sum \vec{F} \quad \Rightarrow \quad m_d \vec{a} = \overrightarrow{\text{Weight}} + \overrightarrow{\text{Archimedes}} + \overrightarrow{\text{Drag}} \quad (1.11)$$

$$m_d \frac{d\vec{v}}{dt} = m_d \vec{g} - \frac{\pi d^3}{6} \rho_g \vec{g} - \frac{1}{2} C_D \frac{\pi d^2}{4} \rho_g v \cdot \vec{v} \quad (1.12)$$

where \vec{p} (kg · m/s) is the droplet momentum, m_d (kg) is the mass of the droplet, v (m/s) is the velocity of the droplet, g (m/s²) is the gravitational acceleration, d (m) is the diameter of the droplet, ρ_g (kg/m³) is the density of the gaseous mixture, C_D (-) is the drag coefficient.

The drag coefficient C_D varies according to the Reynolds number. The figure 1.3 plots the measured values of the drag coefficient as a function of the Reynolds number for a smooth sphere.

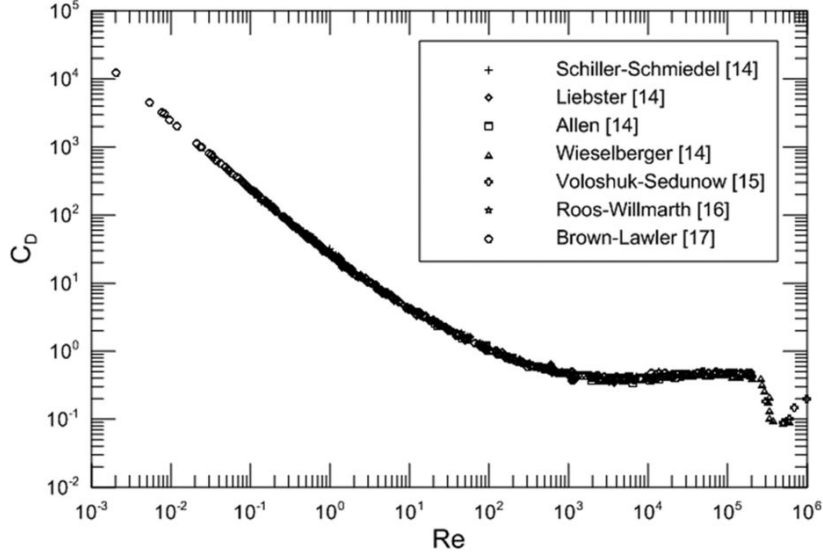


Figure 1.3: Measured values of the drag coefficient as a function of the Reynolds number for a smooth sphere.

Several correlations have been proposed in order to best reproduce the experimental curve. The table 1.5 summarizes the correlations chosen for the model described in this section.

Table 1.5

Reynolds number	Drag coefficient	Chosen correlation
$Re < 1$	$C_D = \frac{24}{Re}$	Stokes' law
$1 \leq Re < 950$	$C_D = \frac{24}{Re} (1 + 0.15 Re^{0.687})$	Schiller & Naumann
$Re \geq 950$	$C_D = 0.45$	Constant value

with $Re = \frac{\rho_g v_d d}{\mu_g}$.

1.3.2 Bestion-Lopez model

In the article [3], the authors, D. Bestion and T. Lopez, present a description for both a conservative and a mechanistic modeling of spray cooling in the containment.

1.3.2.1 Conservative approach

Considering a spray mass flow rate Q_{sp} (kg/s) injected at enthalpy h_{10} (J/kg), it will induce a condensation mass flow rate Q_{cond} (kg/s), resulting in heating up the droplets to the enthalpy h_{11} (J/kg). The following energy balance can be written [3]:

$$(Q_{\text{sp}} + Q_{\text{cond}})h_{\text{l1}} = Q_{\text{sp}}h_{\text{l0}} + Q_{\text{cond}}h_{\text{l1}} + W_{\text{il}} \quad (1.13)$$

where W_{il} (W) is the sensible power received by the droplets during the process, the subscript “il” stands for “interface-liquid”, in fact the main characteristic of this model is the introduction of the concept of “interface” between the gas mixture atmosphere and the liquid droplet, that allows to write an interfacial energy balance.

The interfacial energy balance can be written as follow:

$$W_{\text{il}} + W_{\text{ig}} = Q_{\text{cond}}h_{\text{fg}} = W_{\text{cond}} \quad (1.14)$$

where $W_{\text{gi}} = -W_{\text{ig}}$ (W) is the sensible power provided by the gas to the drops, h_{fg} (J/kg) is the enthalpy of phase change, W_{cond} (W) is the condensation (latent) power.

Introducing W_{gl} (W), the total power provided by the gas to the liquid, we can write:

$$W_{\text{gl}} = W_{\text{gi}} + Q_{\text{cond}}h_{\text{v}} \quad W_{\text{gl}} = Q_{\text{cond}}h_{\text{l}} + W_{\text{il}} \quad (1.15)$$

where h_{v} and h_{l} (J/kg) are respectively the steam enthalpy and the liquid enthalpy evaluated at saturation conditions, such that $h_{\text{fg}} = h_{\text{v}} - h_{\text{l}}$.

One can define the repartition x_{sp} of the total gas-to liquid energy transfer between condensation power and gas cooling power as follows:

$$x_{\text{sp}} = \frac{W_{\text{cond}}}{W_{\text{gl}}} \quad (1.16)$$

It is conservatively assumed that $x_{\text{sp}} = 92\%$. It can be noticed that a subcooled droplet will receive heat thanks to the condensation of steam until the droplet reaches the saturation temperature, but afterwards it may also vaporize by the effect of gas heat transfer. Therefore W_{cond} may also become negative if the vaporization becomes higher than the initial condensation. The vaporization is neglected here due to the fixed value x_{sp} [3].

1.3.2.2 Mechanistic approach

The mechanistic model consists in writing, solving and integrating the mass momentum and energy balance equations for droplets from the injection at the spray nozzle up to the fall to the ground. The objective is to predict the mass and energy transfer with the containment gas mixture.

Assumptions:

- The gas thermodynamic state variables are assumed constant during the fall duration.
- The initial droplet size and initial velocities are given as boundary conditions. The possible drop break up or coalescence between drops are not taken into account.
- Drops are considered spherical.
- Gas is assumed stagnant without velocity and has uniform state variables in the whole containment.

Equations:

-• **Drop mass balance equation**

$$\frac{\pi}{6} \frac{d(\rho_l d^3)}{dt} = \frac{dm}{dt} = \pi d^2 G_{\text{cond}} \quad (1.17)$$

-• **Drop energy balance equation**

$$\frac{\pi}{6} \frac{d(\rho_l h_l d^3)}{dt} = \frac{d(mh_l)}{dt} = \pi d^2 G_{\text{cond}} h_l + \pi d^2 \varphi_{\text{il}}$$

Using the mass balance equation 1.17 and the interface energy balance 1.28 we can obtain the following formulation:

$$\frac{dh_l}{dt} = \frac{6}{\rho_l d} \varphi_{\text{il}} = \frac{6}{\rho_l d} G_{\text{cond}} h_{\text{fg}} - \frac{6}{\rho_l d} \varphi_{\text{ig}} \quad (1.18)$$

-• **Drop momentum balance equation**

$$\begin{aligned} \rho_l \frac{\pi d^3}{6} \frac{dV}{dt} &= -\frac{\pi d^2}{4} \frac{\rho_g}{2} C_d |V - V_g| (V - V_g) + \frac{\pi d^3}{6} (\rho_g - \rho_l) g \quad V_g \approx 0 \\ \Rightarrow \frac{dV}{dt} &= -\frac{3\rho_g}{4\rho_l d} C_D V^2 + \frac{(\rho_l - \rho_g)}{\rho_l} g \end{aligned} \quad (1.19)$$

For the drop momentum balance equation, the drag coefficient C_D is defined in the same way as it is done for the one-drop model (see table 1.5), V (m/s) is the relative drop velocity, V_g (m/s) is the relative gas mixture velocity.

Given Q_{sp} (kg/s) the total spray mass flowrate, d_0 (m) the injected droplet diameter and ρ_l (kg/m³) the liquid density, it is possible to calculate \dot{N} (1/s) the number of drops injected by unit time.

$$\dot{N} = \frac{Q_{\text{sp}}}{m_0} = \frac{Q_{\text{sp}}}{\frac{\pi}{6} \rho_l d_0^3} \quad (1.20)$$

where m_0 (kg) is the injected droplet mass.

The mass diffusion model provides the definition of G_{cond} (kg/m²/s), condensation mass flux.

$$G_{\text{cond}} = D_{v,n} \rho_g Sh \frac{1}{d} \ln \frac{Y_{n,i}}{Y_n} \quad (1.21)$$

where $D_{v,n}$ (m²/s) is the (effective) mass diffusion coefficient of steam in the gas mixture, ρ_g (kg/m³) is the gas mixture density, Sh (-) is the Sherwood number, $Y_{n,i}$ (-) is the non-condensable gases (air) mass fraction at the interface, Y_n (-) is the non-condensables gases (air) mass fraction at the bulk conditions.

$$Y_{n,i} = \frac{1 - X_{\text{steam},i}}{1 - X_{\text{steam},i}(1 - MW_{\text{steam}}/MW_n)} \quad X_{\text{steam},i} = \frac{P_{\text{steam},i}}{P} = \frac{P_{\text{sat}}(T_i)}{P} \quad (1.22)$$

$$Y_n = \frac{1 - X_{\text{steam}}}{1 - X_{\text{steam}}(1 - MW_{\text{steam}}/MW_n)} \quad X_{\text{steam}} = \frac{P_{\text{steam}}}{P} \quad (1.23)$$

where $X_{\text{steam},i}$ (-) is the steam mole fraction at the interface, X_{steam} (-) is the steam mole fraction at the bulk conditions, $P_{\text{steam},i}$ (Pa) is the steam saturation pressure at the interface

temperature T_i (K), P_{steam} (Pa) is the steam partial pressure at the bulk conditions, P (Pa) is the total (absolute) pressure of the atmosphere ($P = P_{\text{steam}} + P_{\text{air}}$), MW_{steam} (g/mol) is the steam (water) molecular weight, MW_n (g/mol) is the non-condensable gases (air) molecular weight.

In order to write an interfacial energy balance, the interfacial heat fluxes φ_{gi} (W/m²) and φ_{li} (W/m²) are defined as the gas-to-interface heat flux and the liquid-to-interface heat flux, respectively. They are calculated as follow:

$$\varphi_{\text{gi}} = h_{\text{gi}}(T_{\text{g}} - T_{\text{i}}) \quad \varphi_{\text{li}} = h_{\text{li}}(T_{\text{d}} - T_{\text{i}}) \quad (1.24)$$

where T_{g} (K) is the gas mixture temperature, T_{i} (K) is the interface temperature, T_{d} (K) is the droplet (liquid) temperature, h_{gi} (W/m²/K) is the gas-to-interface heat transfer coefficient, h_{li} (W/m²/K) is the liquid-to-interface heat transfer coefficient.

$$h_{\text{gi}} = \frac{Nu_{\text{gi}}\lambda_{\text{g}}}{d} \quad h_{\text{li}} = \frac{Nu_{\text{li}}\lambda_{\text{l}}}{d} \quad (1.25)$$

where λ_{g} (W/m/K) is the thermal conductivity of the gas mixture, λ_{l} (W/m/K) is the thermal conductivity of the liquid (droplet). The Nusselt number on the drop side, Nu_{li} (-), is considered constant, while on the gas side, Nu_{gi} (-), it is calculated through the Froessling-Ranz-Marschall model.

$$Nu_{\text{gi}} = 2 + 0.56Re_{\text{d}}^{0.5}Pr_{\text{g}}^{0.3} \quad Nu_{\text{li}} = 10 \quad (1.26)$$

Both the Reynolds and the Prandtl numbers are defined in equation 1.5.

The Sherwood number is calculated through the heat transfer analogy.

$$Sh = 2 + 0.56Re_{\text{d}}^{0.5}Sc_{\text{g}}^{0.3} \quad (1.27)$$

where the Reynolds and the Schmidt numbers are defined in equation 1.8.

-• Energy balance at the interface

$$\varphi_{\text{il}} + \varphi_{\text{ig}} = (h_{\text{v}} - h_{\text{l}})G_{\text{cond}} = h_{\text{fg}}G_{\text{cond}} = \varphi_{\text{cond}} \quad (1.28)$$

From this balance it is possible to calculate the interface temperature T_{i} (K).

At the end of the free fall, it is possible to calculate the total heat and mass transfer for the drop.

$$m_{\text{cond}} = m - m_0 \quad (1.29)$$

The total condensed mass m_{cond} (kg) is calculated as the difference between the final mass of the droplet m (kg) and its initial (injection) mass m_0 (kg).

It is possible to write the following energy balance for the droplet:

$$mh_1 - m_0h_{10} = m_{\text{cond}}h_{\text{v}} + E_{\text{gi}} \quad E_{\text{gi}} = \int_{t_0}^{t_{\text{end}}} \pi d^2 \varphi_{\text{gi}} dt \quad (1.30)$$

where E_{gi} (J) is the total gas-to-interface energy.

For all the drops injected (knowing \dot{N}) it is possible to calculate the total condensation flow rate Q_{cond} (kg/s), the total condensation power W_{cond} (W), the total gas-to-interface power W_{gi} (W).

$$Q_{\text{cond}} = \dot{N}m_{\text{cond}} \quad W_{\text{cond}} = Q_{\text{cond}}h_{\text{fg}} \quad (1.31)$$

$$W_{\text{gi}} = \dot{N}E_{\text{gi}} \quad (1.32)$$

The spray heat transfer repartition x_{sp} (-) can be calculated as defined in equation [1.16](#).

1.4 Implementation

In this section it is provided the description of the Python codes developed to implement the different physical models presented in the previous section.

1.4.1 One-drop model

The Python code for the one-drop model is based on the numerical solution of the three balance equation for the droplet: mass balance, energy balance and momentum balance.

1.4.1.1 Input parameters

The input parameters for the model are five and they can be varied within a certain range in order to perform parametric analysis on the model. The parameters are the following:

Table 1.6

1	P	(bar)	Total (absolute) pressure of the atmosphere
2	ΔT_{sat}	(°C)	Super-heating degree of the atmosphere
3	$v_{d,0}$	(m/s)	Initial (injection) droplet velocity
4	d_0	(mm)	Initial (injection) droplet diameter
5	$T_{d,0}$	(°C)	Initial (injection) droplet temperature

Hypothesis: $P = P_{\text{steam}} + P_{\text{air}}$ $P_{\text{air}} = 1 \text{ bar} = \text{constant}$

1.4.1.2 Definition of constants

The next step of the code consists in the definition of some constants:

Table 1.7

D_{fall}	20 m	Falling height for the drop
MW_{steam}	18 g/mol	Steam (water) molecular weight
MW_{air}	28.965 g/mol	Air molecular weight
g	9.81 m/s ²	Gravitational acceleration
R	8.31 J/mol/K	Gas constant
$D_{v,\text{air,ref}}$	0.282 cm ² /s	Diffusivity of steam in air at ($P_{\text{ref}} = 1 \text{ atm}$, $T_{\text{ref}} = 25 \text{ °C} = 298.15 \text{ K}$)
$C_{p,\text{air}}$	1023 J/kg/K	Air specific heat capacity at constant pressure
λ_g	0.025 W/m/K	Gas mixture conductivity

1.4.1.3 Loops on the input parameters

At this point of the code, five nested *while/for* loops are opened. Each of these loops scans one of the five input parameters in order to create all the possible combinations of test cases. From

now on all calculations are carried out within the innermost loop.

1.4.1.4 Initialization of the variables

1. Water/steam properties calculated through the IAPWS97 Python library (steam tables)

Table 1.8

$T_{\text{sat}}(P_{\text{steam}})$	(K)	Steam saturation temperature at P_{steam}
$T_{\text{g}} = T_{\text{sat}}(P_{\text{steam}}) + \Delta T_{\text{sat}}$	(K)	Gas mixture (atmosphere) temperature
$\rho_{\text{d}}(P, T_{\text{d}})$	(kg/m ³)	Droplet (liquid water) density
$P_{\text{sat}}(T_{\text{d}})$	(Pa)	Steam saturation pressure at T_{d}
$\rho_{\text{sat}}(T_{\text{d}}, x = 1)$	(kg/m ³)	Saturated steam density at T_{d}
$C_{p,\text{steam}}(P_{\text{steam}}, T_{\text{g}})$	(J/kg/K)	Steam specific heat capacity at constant pressure
$C_{p,\text{d}}(P, T_{\text{d}})$	(J/kg/K)	Droplet specific heat capacity at constant pressure
h_{fg}	(J/kg)	Phase change enthalpy

with x (-) the steam quality and $h_{\text{fg}} = h_{\text{steam}}(P_{\text{steam}}, x = 1) - h_{\text{liq}}(P, x = 0)$.

2. Calculation of other variables

- Droplet mass (kg)

$$m_{\text{d}} = \frac{\pi d^3}{6} \rho_{\text{d}} \quad (1.33)$$

- Diffusivity of steam in air calculated as shown in table 1.1
- Steam density (ideal gas law) (kg/m³)

$$\rho_{\text{steam}} = \frac{P_{\text{steam}} MW_{\text{steam}}}{RT_{\text{g}}} \quad (1.34)$$

- Air density (ideal gas law) (kg/m³)

$$\rho_{\text{air}} = \frac{P_{\text{air}} MW_{\text{air}}}{RT_{\text{g}}} \quad (1.35)$$

- Gas mixture density (kg/m³)

$$\rho_{\text{g}} = \rho_{\text{air}} + \rho_{\text{steam}} \quad (1.36)$$

- Gas mixture specif heat capacity (J/kg/K)

$$C_{p,\text{g}} = \frac{P_{\text{steam}}}{P} C_{p,\text{steam}} + \frac{P_{\text{air}}}{P} C_{p,\text{air}} \quad (1.37)$$

- Reynolds, Prandtl and Schmidt numbers as shown in equations 1.5 and 1.8.
- Nusselt and Sherwood numbers as shown in equations 1.4 and 1.7.

- Driving term H_M (-) calculated as shown in table 1.4.
- Droplet mass transfer flow rate \dot{m}_d (kg/s) calculated as shown in equation 1.6.
- Drag coefficient C_D (-) calculated as shown in table 1.5.

3. Latent and sensible heat

- $Q_{\text{lat}} = 0$ (J) \rightarrow Instantaneous latent heat (at the current time step)
- $Q_{\text{sens}} = 0$ (J) \rightarrow Instantaneous sensible heat (at the current time step)
- $Q_{\text{lat,tot}} = 0$ (J) \rightarrow Total latent heat (integral)
- $Q_{\text{sens,tot}} = 0$ (J) \rightarrow Total sensible heat (integral)

4. Falling time and travelled distance

- $t = 0$ (s) \rightarrow Falling time
- $D = 0$ (m) \rightarrow Falling distance
- Δt (s) \rightarrow Time-step for time discretization (i.e. $\Delta t = 0.001$ s)

1.4.1.5 *While* loop for the one-drop H&M transfers during the fall

- Discretization of the drop mass balance equation ($dm_d/dt = \dot{m}_d$)

$$m_d^{i+1} = m_d^i + \dot{m}_d^i \cdot \Delta t \quad (1.38)$$

with $i + 1$ the current time-step and i the previous one.

- Discretization of the drop energy balance equation (eq. 1.2)

$$T_d^{i+1} = T_d^i + \frac{\Delta t}{m_d^i C_{p,d}^i} [h^i S(T_g - T_d^i) + \dot{m}_d^i h_{fg}] \quad (1.39)$$

- Discretization of the drop momentum balance equation (eq. 1.12)

$$v_d^{i+1} = v_d^i - \frac{1}{2} C_D^i \frac{\pi (d^i)^2}{4} \frac{1}{m_d^i} \rho_g (v_d^i)^2 \Delta t + \frac{m_d^i - \frac{\pi (d^i)^3}{6} \rho_g}{m_d^i} g \Delta t \quad (1.40)$$

- Calculation of the sensible heat

- Instantaneous

$$Q_{\text{sens}} = h S (T_g - T_d) \Delta t \quad (1.41)$$

- Integral

$$Q_{\text{sens,tot}}^{i+1} = Q_{\text{sens,tot}}^i + Q_{\text{sens}} \quad (1.42)$$

- Calculation of the latent heat

- Instantaneous

$$Q_{\text{lat}} = \dot{m}_d h_{fg} \Delta t \quad (1.43)$$

if $\dot{m}_d > 0 \Rightarrow$ Condensation $\Rightarrow Q_{\text{lat}} > 0$

if $\dot{m}_d < 0 \Rightarrow$ Vaporization $\Rightarrow Q_{\text{lat}} < 0$

- Integral

$$Q_{\text{lat,tot}}^{i+1} = Q_{\text{lat,tot}}^i + Q_{\text{lat}} \quad (1.44)$$

-• Updating all the variables and calculation of the distance traveled by the drop

$$D^{i+1} = D^i + v_d \cdot \Delta t \quad (1.45)$$

-• Stop the loop if $D \leq 0$ m (the drop reached the ground) or if $d < \text{tolerance}$ (the droplet diameter has become so small, smaller than a certain chosen tolerance, that the drop can be considered totally vaporized).

1.4.2 Bestion-Lopez model

The Python code for the Bestion-Lopez model is based on the numerical solution of the three balance equation for the droplet, similarly to the one-drop model, but in addition it is necessary to solve the energy balance at the interface (eq. 1.13) to calculate the interface temperature T_i .

The structure of the code is basically the same as the one-drop model, what differs is the drop falling height considered ($D_{\text{fall}} = 50$ m instead of 20 m), the way the drop balance equations are written and the introduction of the energy balance at the interface.

1.4.2.1 Initialization of the energy balance at the interface

-• Interface temperature (K) \rightarrow “1/3 rule”

$$T_{i,0} = \frac{1}{3}T_g + \frac{2}{3}T_{d,0} \quad (1.46)$$

-• Interfacial and condensation heat fluxes (W/m²)

$$\varphi_{\text{gi}} = h_{\text{gi}}(T_g - T_i) \quad \varphi_{\text{li}} = h_{\text{li}}(T_d - T_i) \quad \varphi_{\text{cond}} = G_{\text{cond}}h_{\text{fg}} \quad (1.47)$$

1.4.2.2 Drop balance equations time discretization

-• Drop mass balance equation (eq. 1.17)

$$m_d^{i+1} = m_d^i + \pi(d^i)^2 G_{\text{cond}}^i \Delta t \quad (1.48)$$

-• Drop energy balance equation (eq. 1.18)

$$h_1^{i+1} = h_1^i + \frac{6}{\rho_1^i d^i} \varphi_{\text{il}}^i \Delta t \quad \Rightarrow \quad T_d^{i+1} = T(P_{\text{tot}}, h_1^{i+1}) \quad (1.49)$$

-• Drop momentum balance equation (eq. 1.19)

$$V^{i+1} = V^i - \frac{3\rho_g}{4\rho_1^i d} C_D^i (V^i)^2 \Delta t + \frac{(\rho_1^i - \rho_g)}{\rho_1^i} g \Delta t \quad (1.50)$$

Where the apexes $i + 1$ and i indicate the current and the previous time-steps, respectively.

1.4.2.3 Calculation of the interface temperature

In order to calculate the evolution of the interface temperature T_i it is necessary to solve the interface energy balance 1.28. It is a non-linear equation in T_i , so it is necessary to use an iterative method: *Newton's method*.

- Define the function $\Psi(T_i)$

$$\Psi(T_i) = \varphi_{\text{cond}}(T_i) - \varphi_{\text{il}}(T_i) - \varphi_{\text{ig}}(T_i) \quad (1.51)$$

- Apply the *Newton's method* to the function $\Psi(T_i)$ using the *scipy.optimize* Python library.

$$T_i = \text{optimize.newton}(\Psi(T_i), T_{i,0}) \quad (1.52)$$

It gives the value of T_i for which $\Psi(T_i) = 0$, where $T_{i,0}$ (K) is the initial value of the interface temperature given as initial estimate of the zero that should be somewhere near the actual zero.

- Recalculation of: $G_{\text{cond}}(T_i)$ $\varphi_{\text{cond}}(T_i)$ $\varphi_{\text{gi}}(T_i)$ $\varphi_{\text{li}}(T_i)$
- Calculation of: m_{cond} E_{gi} Q_{cond} W_{gi} W_{cond}

1.5 Validation of the models

This section provides a validation of the models described so far. A parametric analysis of the input parameters is performed for the One-drop model. For the validation of the Bestion/Lopez model, an attempt was made to reproduce the results presented in article [3] using both the One-drop model and the Bestion/Lopez model itself; the results obtained are compared with those presented in the article. Finally, it is performed a comparison between the experimental results obtained from the test cases carried out at the ISRN CARAIDAS experimental facility [4] and the results obtained by applying the One-drop model to the same test cases (nine test cases are presented in [4]). For the latter analysis, uncertainty quantification was also carried out using the UQLab MATLAB tool.

1.5.1 One-drop model: parametric analysis

Table 1.9

	Input parameters
Atmosphere	$P = (2, 3, 4, 5)\text{bar}$ $\Delta T_{\text{sat}} = (0, 20, 40, \dots, 140)\text{K}$
Droplet	$d_0 = 1 \text{ mm}$ $T_{\text{d},0} = 20 \text{ }^\circ\text{C}$ $v_{\text{d},0} = 15 \text{ m/s}$
Falling height	$D_{\text{fall}} = 20 \text{ m}$
Time-step	$\Delta t = 0.01 \text{ s}$
Driving term	Parametric analysis among M0 M1 M3 M5 M9
Diffusivity	$D_{\text{v}-0}$

Table 1.9 presents the generic test cases reproduced to assess the sensibility of the model to different input parameters. The results below show the variation in diameter and temperature of the single drop during its fall and they are commented on the last page of this subsection.

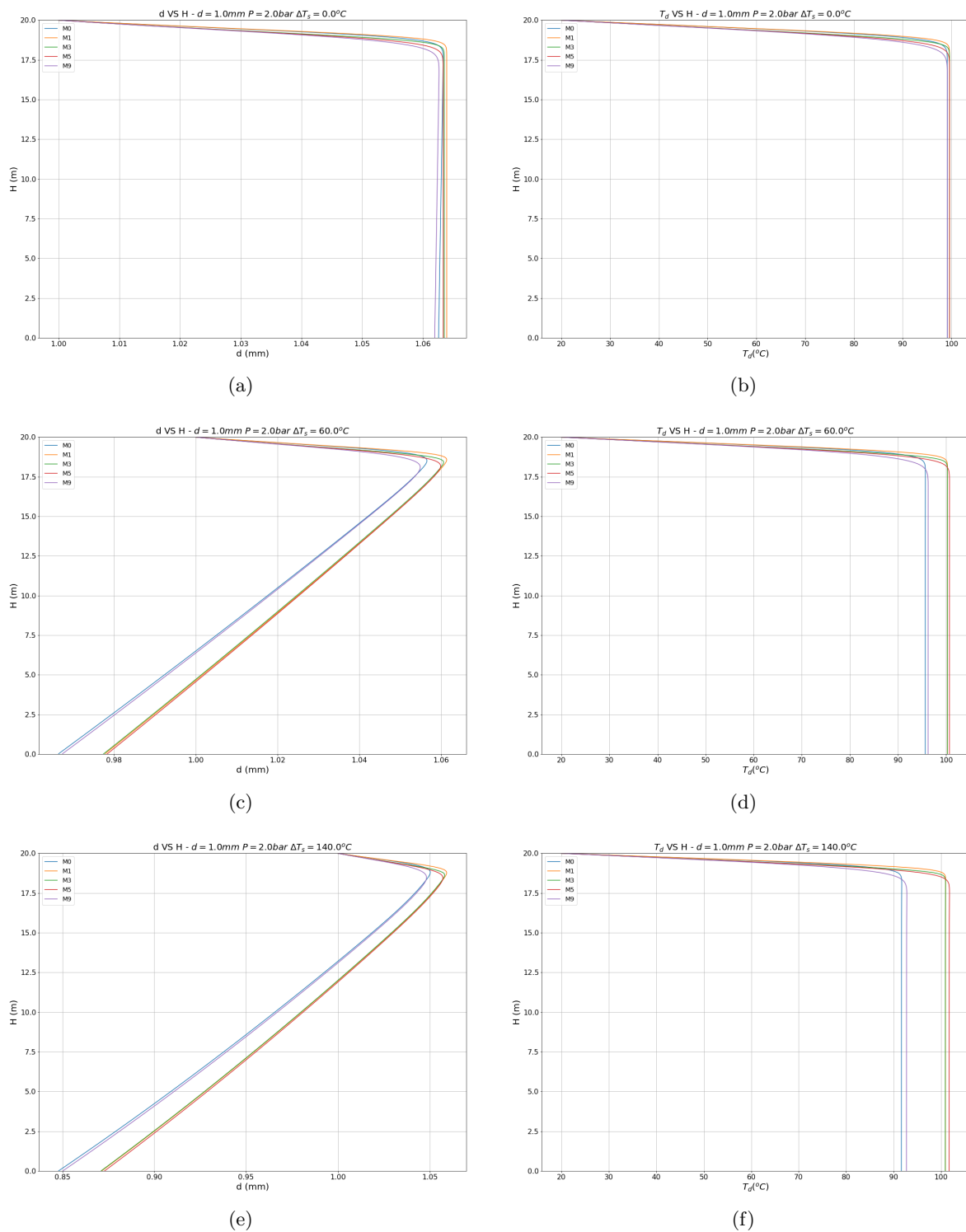


Figure 1.4: Evolution along the falling height of (a)-(c)-(e) the droplet diameter and (b)-(d)-(f) the droplet temperature.

Conditions: $P = 2$ bar, (a)-(b) $\Delta T_{\text{sat}} = 0$ K, (c)-(d) $\Delta T_{\text{sat}} = 60$ K, (e)-(f) $\Delta T_{\text{sat}} = 140$ K

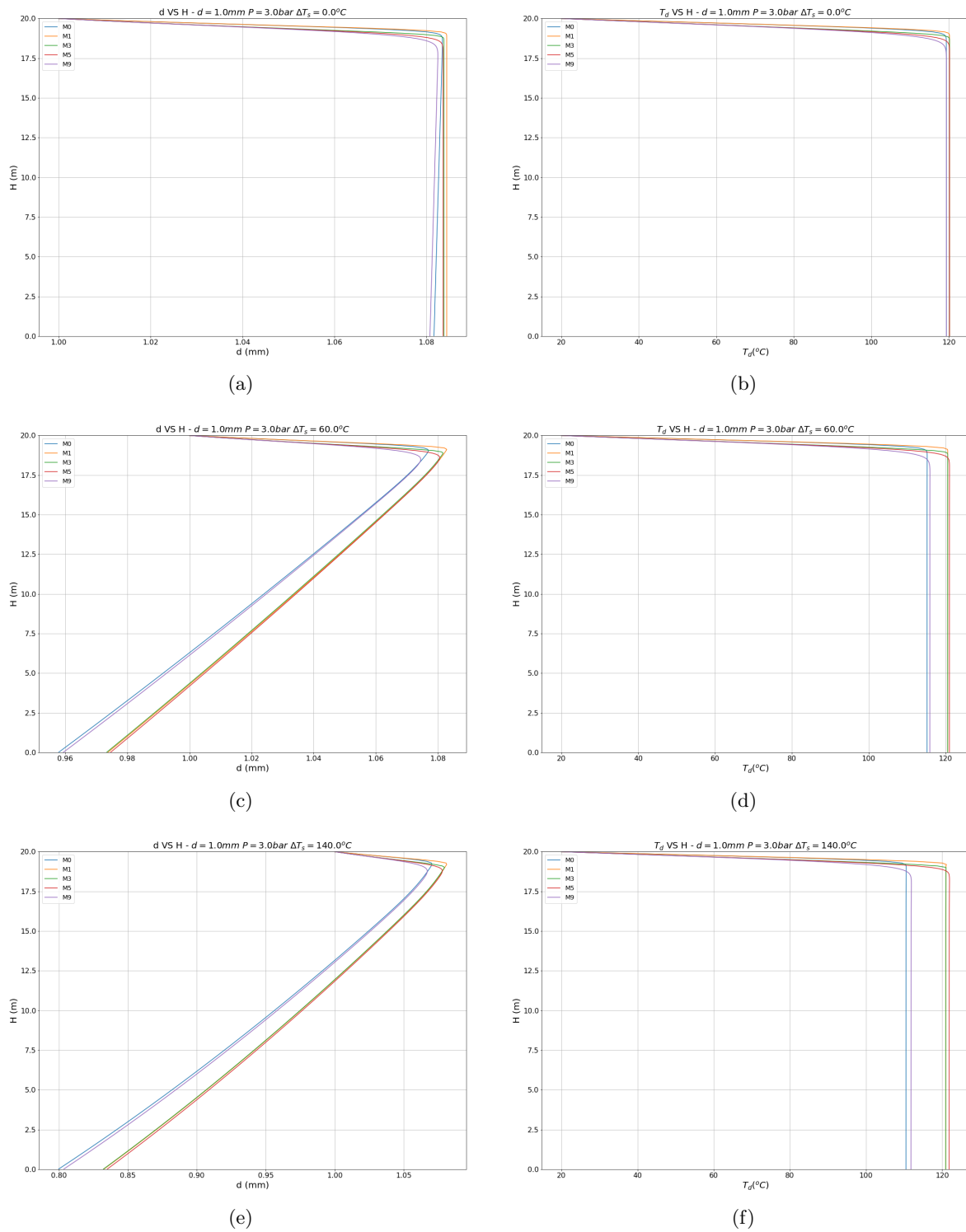


Figure 1.5: Evolution along the falling height of (a)-(c)-(e) the droplet diameter and (b)-(d)-(f) the droplet temperature.

Conditions: $P = 3$ bar, (a)-(b) $\Delta T_{\text{sat}} = 0$ K, (c)-(d) $\Delta T_{\text{sat}} = 60$ K, (e)-(f) $\Delta T_{\text{sat}} = 140$ K

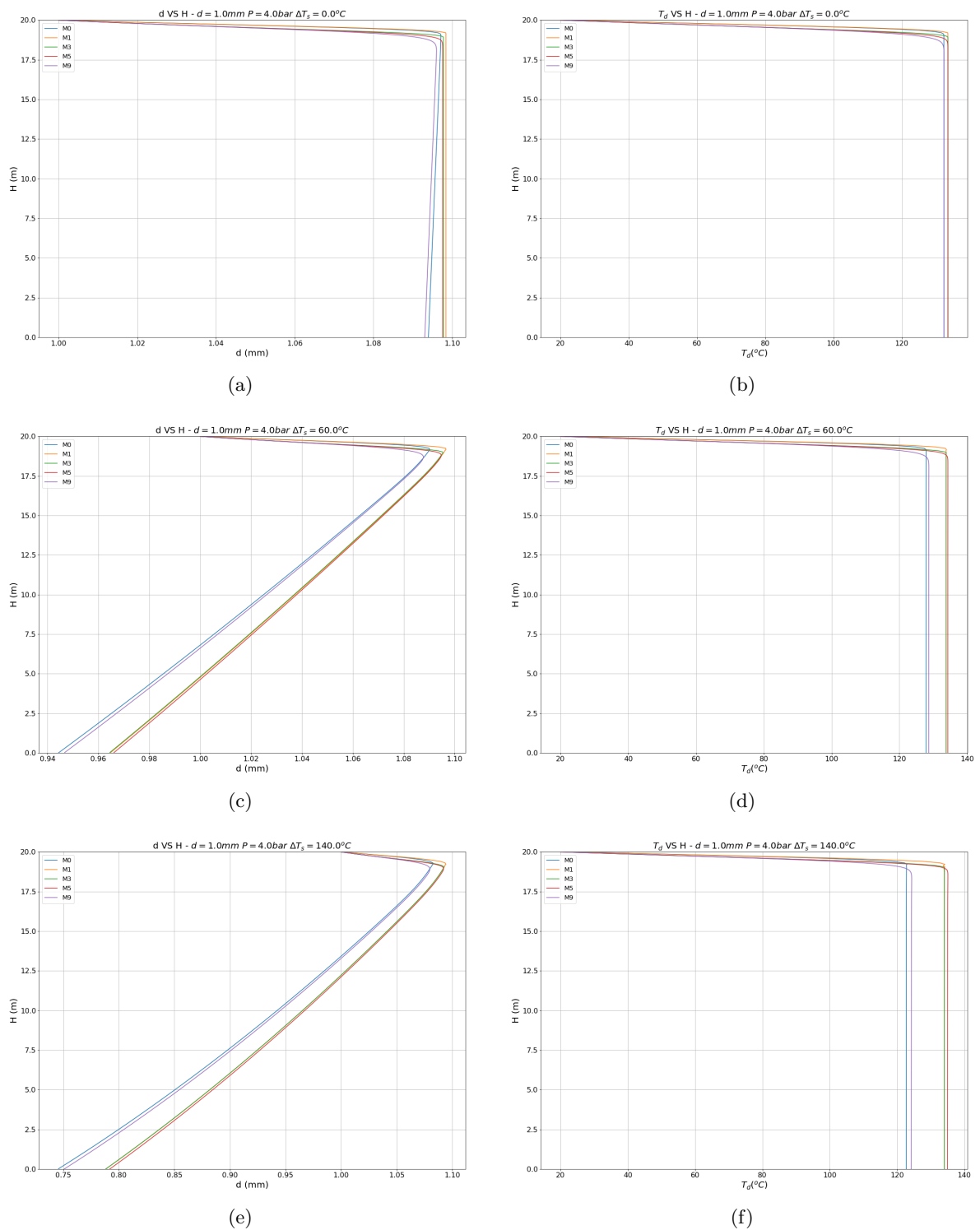


Figure 1.6: Evolution along the falling height of (a)-(c)-(e) the droplet diameter and (b)-(d)-(f) the droplet temperature.

Conditions: $P = 4$ bar, (a)-(b) $\Delta T_{\text{sat}} = 0$ K, (c)-(d) $\Delta T_{\text{sat}} = 60$ K, (e)-(f) $\Delta T_{\text{sat}} = 140$ K

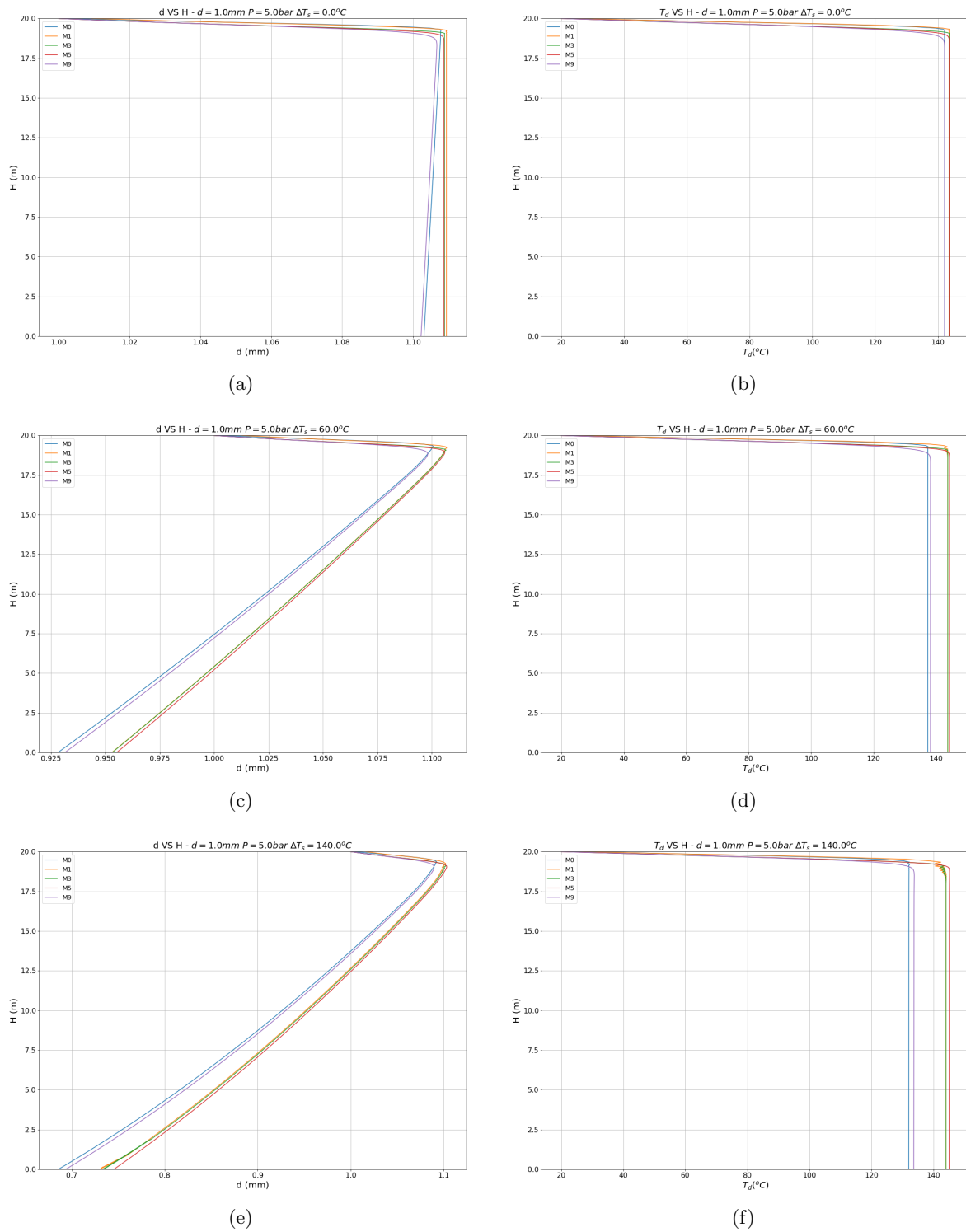


Figure 1.7: Evolution along the falling height of (a)-(c)-(e) the droplet diameter and (b)-(d)-(f) the droplet temperature.

Conditions: $P = 5 \text{ bar}$, (a)-(b) $\Delta T_{\text{sat}} = 0 \text{ K}$, (c)-(d) $\Delta T_{\text{sat}} = 60 \text{ K}$, (e)-(f) $\Delta T_{\text{sat}} = 140 \text{ K}$

The results above are an extrapolation of the parametric analysis carried out on the One-drop model: for each pressure level it is shown the evolution of the diameter and temperature of the droplet for three levels of superheating degree, $\Delta T_{\text{sat}} = (0, 60, 140)\text{K}$.

A common behaviour can be observed for all cases: during the first 1-2 metres of fall ($H \approx 18 \div 20\text{ m}$) the droplet is always subject to a *condensation phase*, i.e. the steam present in the atmosphere condenses on the surface of the droplet, increasing its diameter and also its temperature.

At the end of the *condensation phase*, two different behaviours can be observed depending on the degree of superheating: in the case of a saturated atmosphere ($\Delta T_{\text{sat}} = 0\text{ K}$), the diameter of the drop remains almost unchanged during the rest of the fall and its temperature remains constant and almost equal to the saturation temperature of the atmosphere, while in the case of a superheated atmosphere ($\Delta T_{\text{sat}} > 0\text{ K}$) one always observes the beginning of a *vaporization phase* in which the diameter of the drop decreases during the rest of the fall. The *vaporization phase* mentioned is more prominent both as the degree of superheating increases (with the same total pressure) and as the total pressure increases (with the same degree of superheating).

Focusing on the parametric analysis made on the mass transfer driving term H_M models (M0, M1, M3, M5, M9), it can be clearly seen that the results obtained with the M0 and M9 models (both based on density gradients) differ from the results obtained with the M1, M3 and M5 models (based on mass fraction gradients): under the same conditions, models M0 and M9 show a shorter *condensation phase* (the diameter and temperature of the droplet reach a lower maximum value) than models M1, M3 and M5, consequently for models M0 and M1 a lower diameter and temperature are always obtained during the *vaporization phase*.

1.5.2 Bestion-Lopez model

The test case used for the validation of this model is directly taken from the paper [3], the input parameters are listed in the table 1.10.

Table 1.10

	Input parameters		
Atmosphere	$P = 2 \text{ bar}$	$P_{\text{air}} = 1 \text{ bar}$	$P = P_{\text{steam}} + P_{\text{air}}$
	$\Delta T_{\text{sat}} = (15, 30) \text{ K}$		
Droplet	$d_0 = (0.3, 1) \text{ mm}$	$T_{d,0} = 20 \text{ }^\circ\text{C}$	$v_{d,0} = 15 \text{ m/s}$
Falling height	$D_{\text{fall}} = 50 \text{ m}$		
Driving term	M1		
Diffusivity	$D_v - 0$		

The following plots show the droplet diameter evolution along the falling height, comparing between the results obtained using the Bestion-Lopez model, the results obtained using the one-drop models M0/M1 and the results presented in [3].

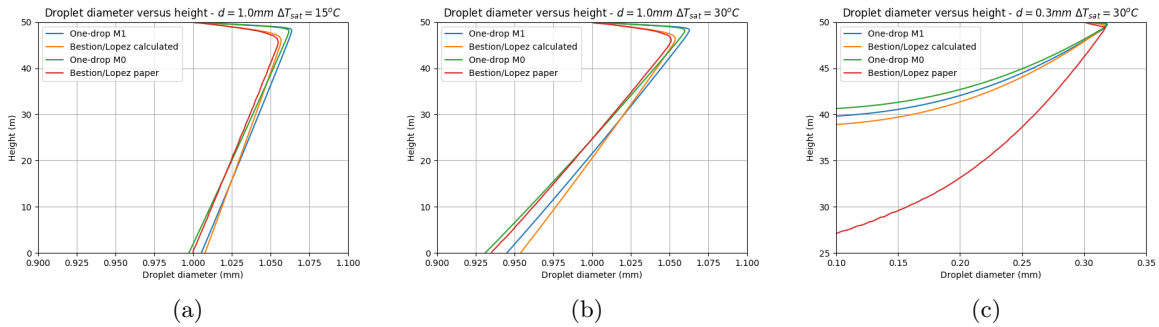


Figure 1.8: Evolution of the droplet diameter along the falling height. Conditions: $P = 2 \text{ bar}$, (a) $[d_0 = 1 \text{ mm}, \Delta T_{\text{sat}} = 15 \text{ K}]$, (b) $[d_0 = 1 \text{ mm}, \Delta T_{\text{sat}} = 30 \text{ K}]$, (c) $[d_0 = 0.3 \text{ mm}, \Delta T_{\text{sat}} = 30 \text{ K}]$

In both the two cases with initial droplet diameter equal to 1 mm, it can be noticed that, in the *Bestion/Lopez calculated* results, the *condensation phase* (first meters of fall in which the droplet diameter increases due to condensation of steam on the droplet) is very close to the results showed in the paper, while the *vaporization phase* (rest of the fall in which the droplet diameter decreases due to its own vaporization) is a bit shifted towards the right, giving a bigger final droplet diameter. In the case with $d_0 = 0.3 \text{ mm}$, the difference between the *Bestion/Lopez calculated* results and the paper results is more significant, in particular regarding the height at which the droplet is completely vaporized: about 27 m from the ground for the paper, while about 39 m from the ground for the calculated results.

Regarding the results obtained with the *One-drop model*, we can clearly see that the expected *condensation phase* lasts for less meters compared to the Bestion/Lopez results (both those calculated and those shown in the paper), but the effect of condensation leads to a larger diameter of the drop reached at the transition point (point where there is the transition from

condensation to vaporization). Regarding the *vaporization phase*, it can be noted that the results that come closest to those shown in the paper are those obtained with the *One-drop M0 model*. Instead the *One-drop M1 model* shows similar results to the *Bestion/Lopez calculated model* because both models use the same type of *driving term* (M1).

1.5.3 Comparison with IRSN CARAIDAS experimental results

The IRSN CARAIDAS experimental set-up was used to study drop evolution under representative conditions of post-accident atmosphere. The cylindrical enclosure is of 5 m high and 0.6 m inner diameter. Homogeneous conditions are obtained with gas temperatures T_g from 20 to 160 °C, absolute pressures P from 1 to 8 bar and relative humidities HR from a 3 up to 95 %. The drop generator is located at the top of the vessel in order to keep it at a constant temperature whatever the vessel temperature is. It produces monosized water droplets from 200 to 700 μm diameter. Drop injection temperature T_d is set between 20 and 80 °C by an electric heater. Drop diameter d optical measurements are performed at 3 elevations: at the top (drop generator, $z = 0$ m), at $z = 2.51$ m and at the bottom ($z = 4.39$ m). The tests conditions are given in table 1.11: *evaporation* and *condensation* tests are called EVAP-i respectively COND-i tests. [4]

Table 1.11: Mean values for the gas characteristics and for the droplet initial conditions [4]

Test	P (bar)	T_g (°C)	HR (%)	T_d (°C)	d_0 (μm)	$v_{d,0}$ (m/s)
EVAP3	1.00	20.1	20.5	20.6	611 ± 4	3.58
EVAP13	5.42	100.1	15.0	31.0	605 ± 4	3.75
EVAP18	1.00	135.2	3.0	30.9	309 ± 5	3.66
EVAP21	4.29	97.4	12.0	29.2	311 ± 7	3.63
EVAP24	4.97	135.0	4.0	30.3	296 ± 4	3.10
COND1	4.00	141.3	55.0	36.0	341 ± 2	4.90
COND2	4.80	141.6	71.0	37.0	344 ± 2	4.70
COND7	5.30	139.3	87.0	35.0	593 ± 11	2.10
COND10	2.40	121.5	79.0	16.0	673 ± 5	2.10

An uncertainty due to the measurement method is associated with the mean value of the initial drop diameter (d_0).

Below it is proposed to simulate the experiments using the *One-drop model* in order to make a comparison between the results of the code and the experimental results presented in [4], in order to obtain a further validation of the model.

Finally, a quantification of the uncertainties on the model is carried out, using as input uncertainty the one measured on the initial drop diameter. [4]

1.5.3.1 Comparison 1

The first comparison consists in reproducing the IRSN CARAIDAS tests using the One-drop Python code with models M0, M1, M9 for the mass transfer driving term and D_v-0 as mass

diffusivity. The results of the simulations are compared with the experimental measurement presented in [4].

In order to perform the simulation we have to set the proper input parameters for the Python code. At first it is necessary to define the relative humidity HR (%):

$$\text{HR} = \frac{P_{\text{steam}}}{P_{\text{sat}}(T_g)} \cdot 100 \quad (1.53)$$

where P_{steam} (Pa) is the steam partial pressure and $P_{\text{sat}}(T_g)$ (Pa) is the saturation pressure at the gas mixture temperature T_g .

Table 1.12: Input parameters comparison 1

Steam partial pressure	(Pa)	$P_{\text{steam}} = \text{HR}/100 \cdot P_{\text{sat}}(T_g)$
Air partial pressure	(Pa)	$P_{\text{air}} = P - P_{\text{steam}}$
Superheating degree	(°C)	$\Delta T_{\text{sat}} = T_g - T_{\text{sat}}(P_{\text{steam}})$
Mass transfer driving term	(-)	M0 M1 M9
Mass diffusion coefficient	(m ² /s)	D_v-0

Below we show the code-experiment comparison for $z = 2.51$ m and $z = 4.39$ m.

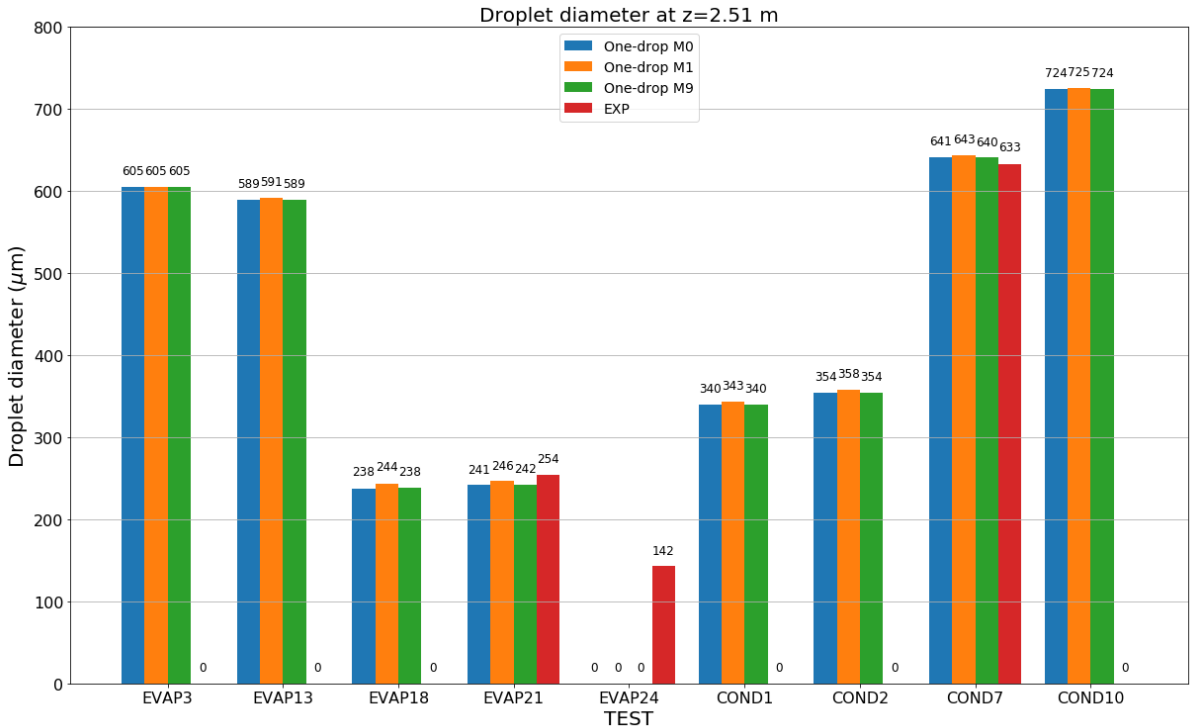


Figure 1.9: Code-experiment comparison: droplet diameter at $z = 2.51$ m.

For the comparison at $z = 2.51$ m (figure 1.9), unfortunately the only experimental measurements available are those for tests EVAP21, EVAP24 and COND7, while for the comparison

at $z = 4.39$ m (figure 1.10) we have the experimental measurements for all the tests with the associated uncertainty (error bars).

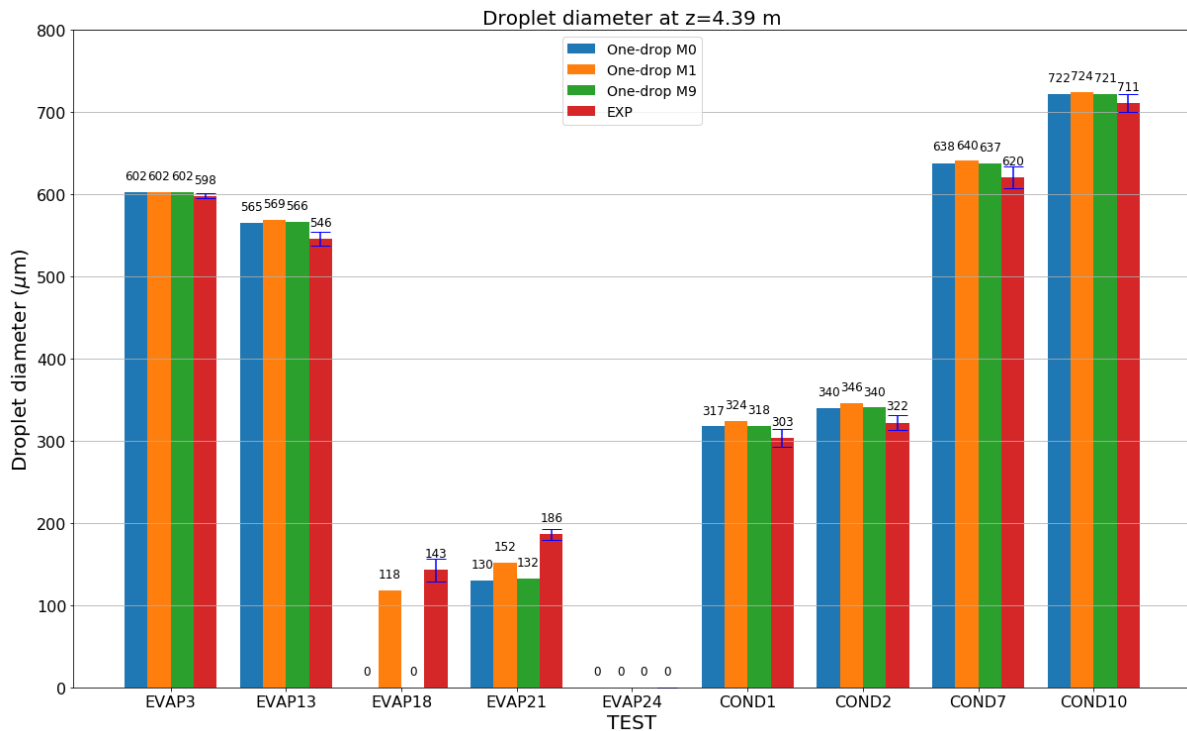


Figure 1.10: Code-experiment comparison: droplet diameter at $z = 4.39$ m.

The major discrepancies between the experimental results and those of the code are obtained for tests EVAP18, EVAP21 and EVAP24.

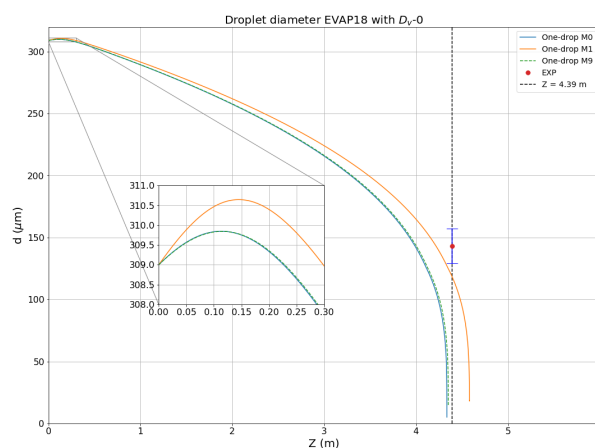


Figure 1.11: EVAP18 droplet diameter evolution.

Figures 1.11, 1.12, 1.13 show the droplet diameter evolution along the falling height for these three test, in order to try to explain the presence of the discrepancies.

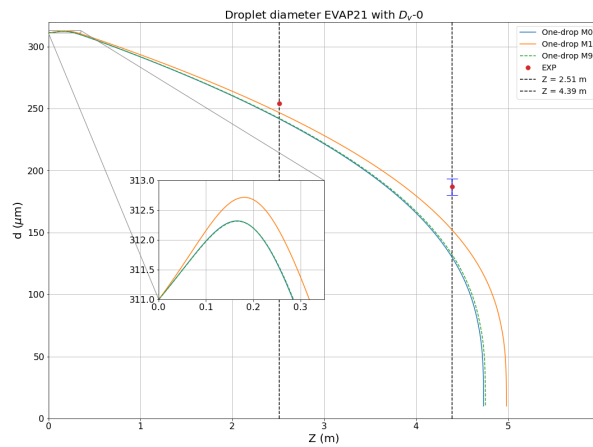


Figure 1.12: EVAP21 droplet diameter evolution.

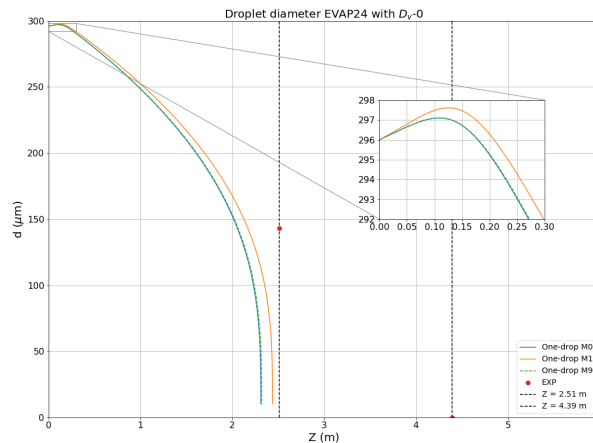


Figure 1.13: EVAP24 droplet diameter evolution.

The presence of large discrepancies between the code and experimental results, for tests EVAP18, EVAP21 and EVAP24, may be justified by the measurement positions chosen: these three tests are those with the smallest initial drop diameter and with atmospheric conditions that lead to fast vaporization of the drop itself and, as the rate of change in the diameter of the drop becomes more and more significant during the fall, the trend obtained with the code differs more and more from the experimental measurements. This effect can clearly be seen from the figure 1.12, test EVAP21: at $z = 2.51$ m the curves are quite close to the experimental measurement, while at $z = 4.39$ m, where the rate of change of the drop diameter is higher, the curves deviate significantly from the experimental measurement. For test EVAP18 (figure 1.11) the effect is equally recognizable, so much so that, for the two curves obtained with M0 and M9 models, the drop is completely vaporized just before reaching the measurement point at $z = 2.51$ m (this explains the big discrepancy between these two models and the experimental measurement showed in figure 1.9, for test EVAP18). With regard to test EVAP 24 (figure 1.13), the effect is so strong that the drop is completely vaporized before the measurement point at $z = 2.51$ m for all 3 curves. For this last test, it should be made clear that the experimental measurement at $z = 4.39$ m simply indicates that the drop is completely vaporized before it

reaches this point: assuming that the experimental curve can follow approximately the trend of the curves obtained with the models and knowing the experimental measurement at $z = 2.51$ m, you can estimate that in the real experiment the drop reaches the complete vaporization between $z = 3$ m and $z = 3.5$ m.

The results for the other tests are very close (taking into consideration the uncertainties associated to the experimental measurements) and what can be noted is that the One-drop M1 model gives always the higher value of drop diameter at the measurement position (remembering that M1 model uses a mass transfer driving term based on mass fractions gradients, while both M0 and M9 use a mass transfer driving term based on density gradients, in fact these last two show almost the same identical results).

It must be mentioned that in this comparison it was decided not to use the M3 and M5 models for the mass transfer driving term, both to avoid producing too crowded graphs and because the M1 model is quite representative also for these two models (all three are based on mass fraction gradients and, from the analysis made in the subsection 1.5.1, it can be seen that they produce very similar results).

1.5.3.2 Comparison 2

The second comparison is basically structured in the same way as the first one, with the difference that this time the parametric analysis is carried out on the type of mass diffusivity used (D_v-0 , D_v-1 , $D_v-2,3$), maintaining instead a single type of mass transfer driving term (M1). It was decided to use the M1 model because, from the results of the first comparison, it is the one that produces the most conservative results (the slowest condensation/vaporisation rates).

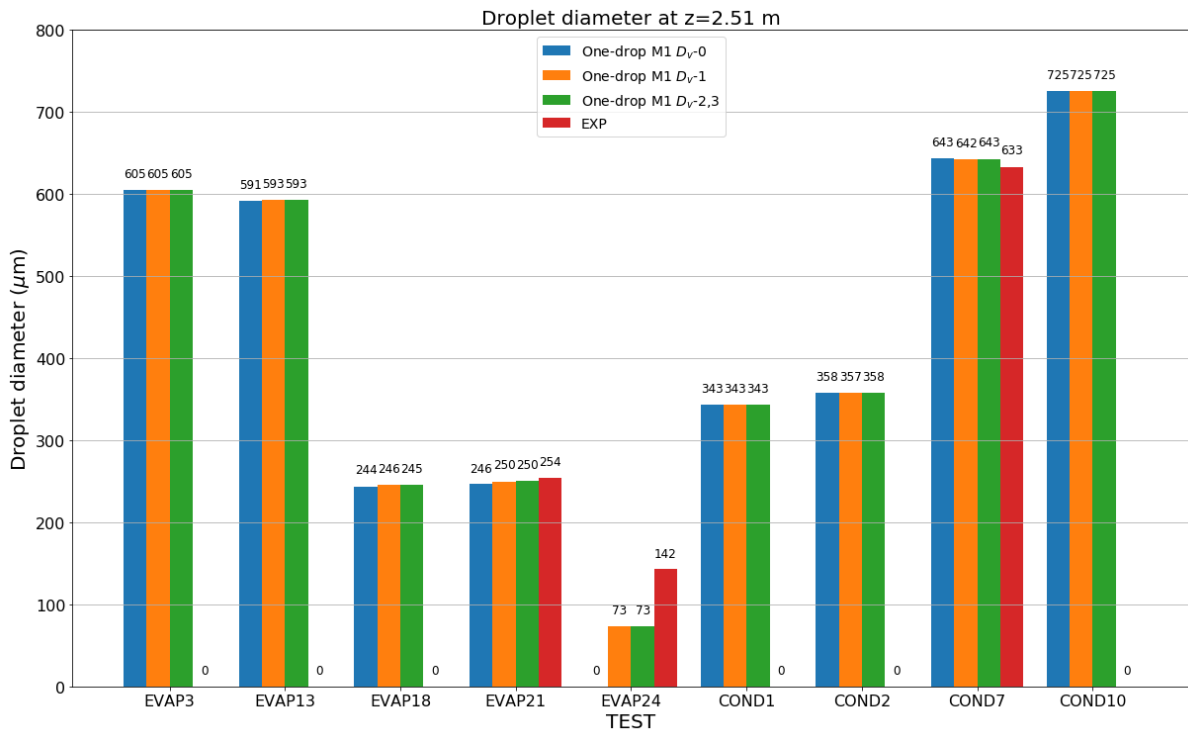


Figure 1.14: Code-experiment comparison: droplet diameter at $z = 2.51$ m.

As done for the first comparison, the code-experiment comparisons for the drop diameter at $z = 2.51$ m (figure 1.14) and $z = 4.39$ m (figure 1.15) are shown.

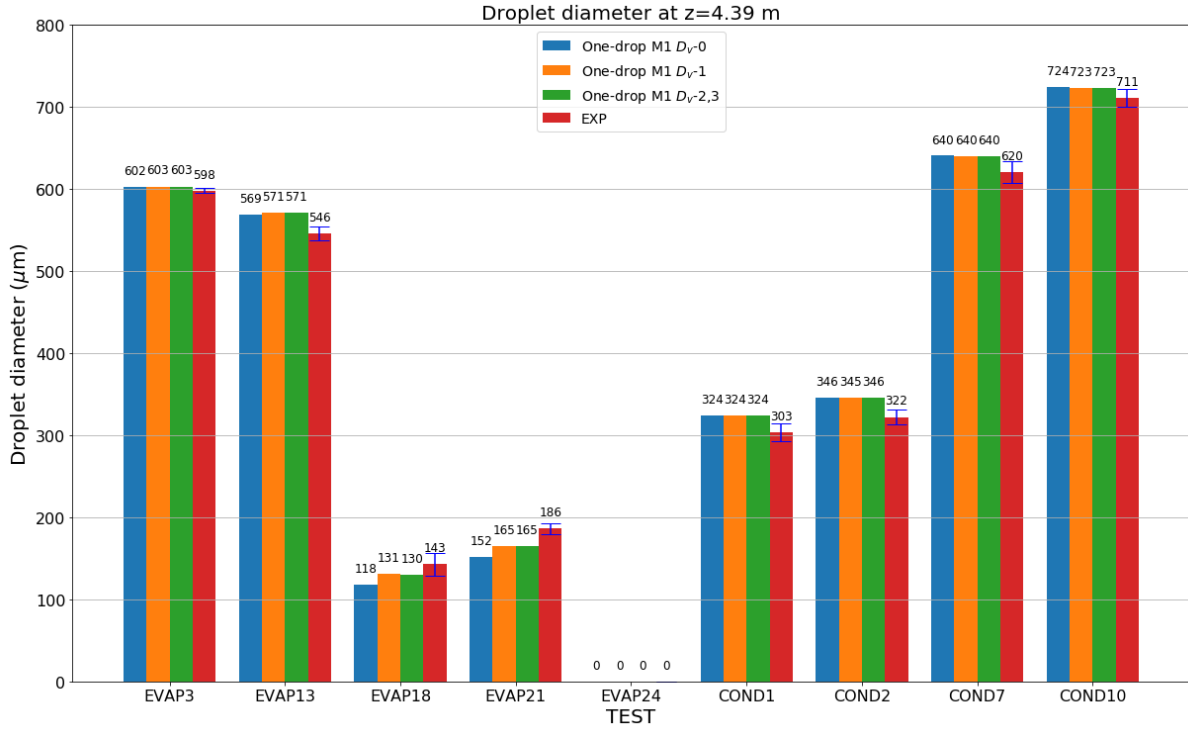


Figure 1.15: Code-experiment comparison: droplet diameter at $z = 4.39$ m.

As also found in the first comparison, the biggest discrepancies occur for tests EVAP18, EVAP21 and EVAP24. It is appreciable, again in these three cases, the difference between the use of the three different mass diffusion coefficients.

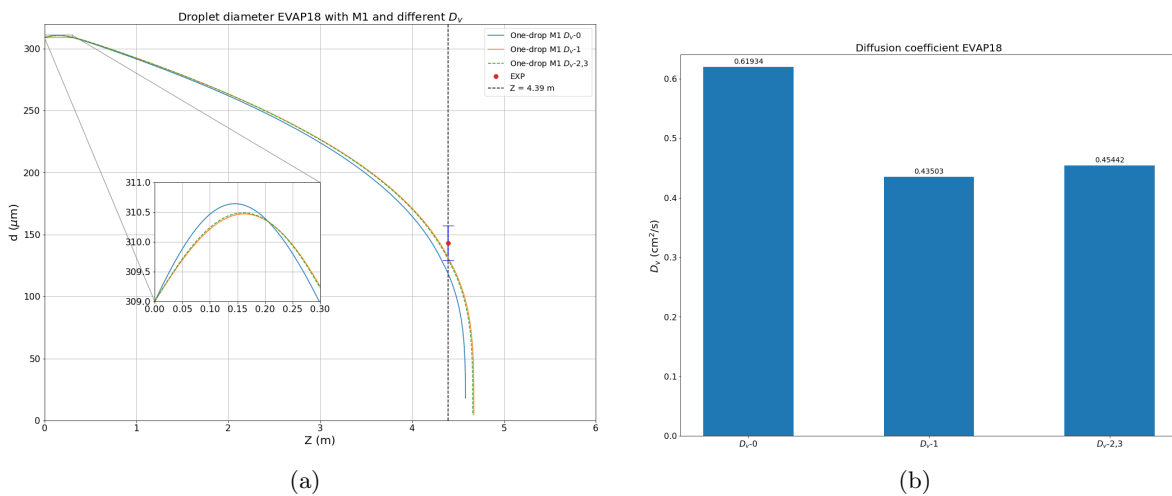


Figure 1.16: EVAP18 (a) droplet diameter evolution and (b) mass diffusivity.

Figures 1.16, 1.17 and 1.18 show the evolution of the drop diameter along the drop height

for tests EVAP18, EVAP21 and EVAP24, respectively. Each of them is flanked by a graph that shows the value of each of the three mass diffusion coefficients (remember that this value remains constant during the entire drop fall as it depends on the total pressure inside the enclosure and on the temperature of the gas mixture, both constant during the drop fall).

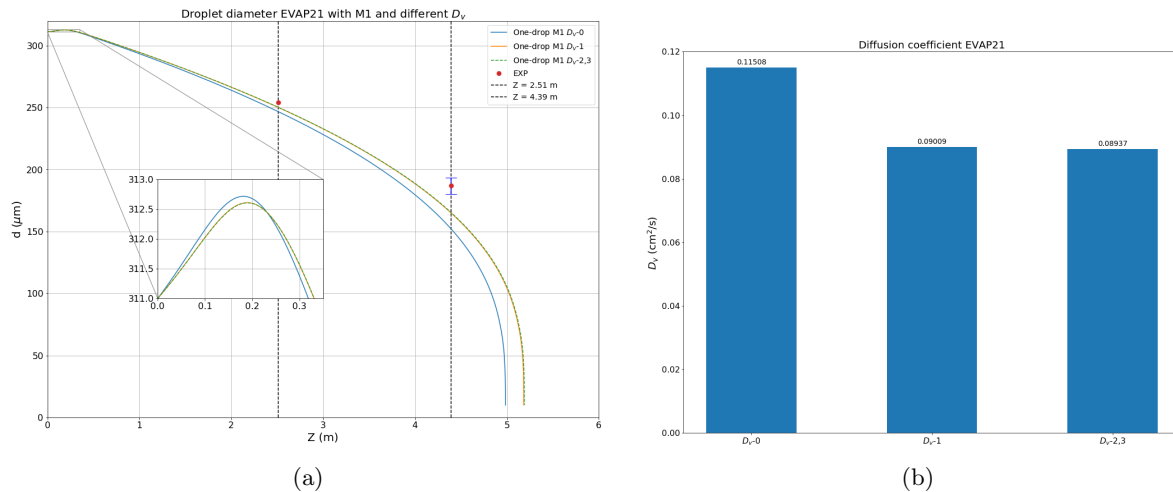


Figure 1.17: EVAP21 (a) droplet diameter evolution and (b) mass diffusivity.

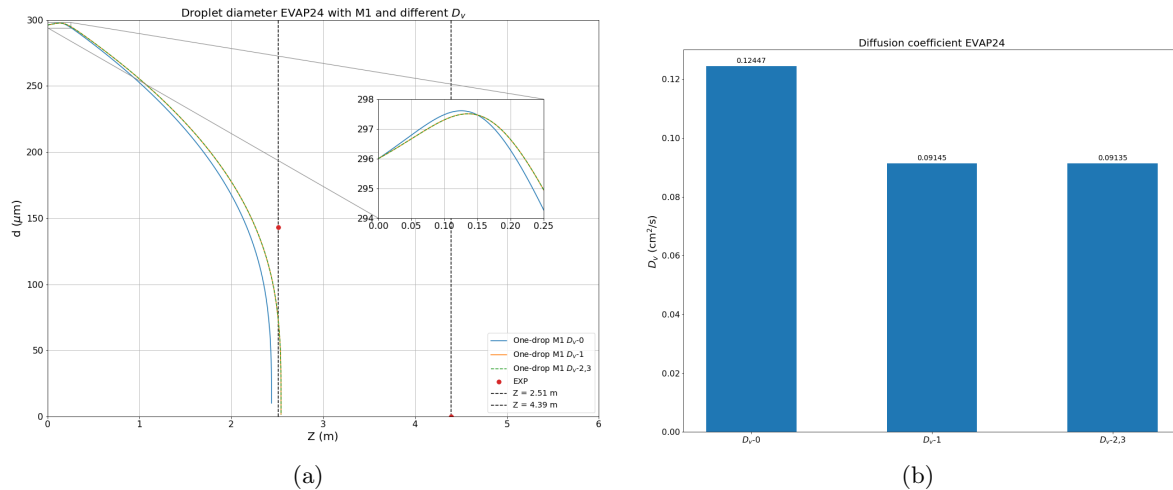


Figure 1.18: EVAP24 (a) droplet diameter evolution and (b) mass diffusivity.

From the previous graphs it can be deduced that the higher the value of the diffusion coefficient the higher the condensation/vaporization rate will be, as you would intuitively expect. For all three cases, in fact, the greatest value of the drop diameter at the end of the condensation phase is reached by the model with $D_v=0$ and, at the same time, this is the model where the transition point from the condensation phase to the vaporization phase is reached more quickly. In addition, the effect of the diffusion coefficient is clearly visible even in the vaporization phase: the model with $D_v=0$ leads to the complete vaporization of the drop slightly earlier than the model with $D_v=1$ and $D_v=2,3$, in all three cases.

1.5.3.3 Uncertainty quantification one-drop model

Taking advantage of the uncertainty data (mean value and standard deviation) on the initial drop diameter provided in table 1.11, this section provides an Uncertainty Quantification (UQ) on the *One-drop model* using the UQLab [10] tool. Given the uncertain parameters and the stochastic variables used to describe the associated uncertainties, the goal is to obtain the statistical description of a certain quantity (e.g. droplet diameter and/or temperature evolution), in order to provide, typically, its mean value and standard deviation. [11]

The UQ strategy used is divided into different phases:

1. Identification of uncertain parameters and their uncertainty (e.g. range of variation or mean value and standard deviation).

In our case: it is considered a single uncertain parameter, the **initial droplet diameter** d_0 , with its mean value and standard deviation (table 1.11).

2. Selection of the Probability Density Function (PDF) according to which each uncertain parameter varies around its reference value (e.g. uniform, Gaussian, etc.).

In our case: it is arbitrarily chosen to use a **uniform PDF**. This choice is arbitrary due to lack of details on measurements error distributions for the experimental uncertainties. On the other hand, modeling uncertainties do not have an intrinsic error definition, therefore the use of an uniform PDF is still object of an arbitrary assumption. [11]

3. Choice of model representation/approximation method.

In our case: it is chosen to use the **Polynomial Chaos Expansion** (PCE) [12]. Through this method the physical quantity to be analyzed is described by a spectral development on a basis of so-called chaos polynomials (see [11] for more details). Once you have determined the number of uncertain parameters M and the order of chaos polynomials p , $(p+1)^M$ are the specific evaluations of the model to be performed for a Design Of Experiments (DOE, see table 1.13) gathering the $(p+1)^M$ combinations of uncertain parameters.

In our case: single uncertain parameter ($M = 1$), third-order PCE with Quadrature Gaussian method ($p = 3$).

$$(p+1)^M = (3+1)^1 = 4 \text{ specific evaluations of the model} \quad (1.54)$$

Table 1.13: Design of Experiments for IRSN CARAIDAS tests

Test	d_0 (μm)			
EVAP3	605.03387	608.64454	613.35546	616.96613
EVAP13	599.03387	602.64454	607.35546	610.96613
EVAP18	301.54234	306.05568	311.94432	316.45766
EVAP21	300.55928	306.87795	315.12205	321.44072
EVAP24	290.03387	293.64454	298.35546	301.96613
COND1	338.01694	339.82227	342.17773	343.98306
COND2	341.01694	342.82227	345.17773	346.98306
COND7	576.59315	586.52249	599.47751	609.40685
COND10	665.54234	670.05568	675.94432	680.45766

In table 1.13 it is shown the DOE for each test of the IRSN CARAIDAS experiment (4 evaluation for each test).

- Once all the combinations of experiments have been carried out, the physical quantity (e.g. the diameter or the temperature of the drop during its fall) of which you want to obtain the statistical description is chosen. Through UQlab, the PCE coefficients are calculated and through these it is possible to easily calculate the **mean value** and the **standard deviation** of the physical quantity considered, due to the uncertainty of the input parameter of the model (initial diameter of the drop in our case). See [11] for more details.

Below (figures 1.19 and 1.20) it is proposed again the comparison between the One-drop model and the experimental results of the IRSN CARAIDAS tests, at the two reference levels, $z = 2.51$ m and $z = 4.39$ m, but this time the values shown for the One-drop model are the **mean values** and each of them is associated with an **uncertainty** (error bar).

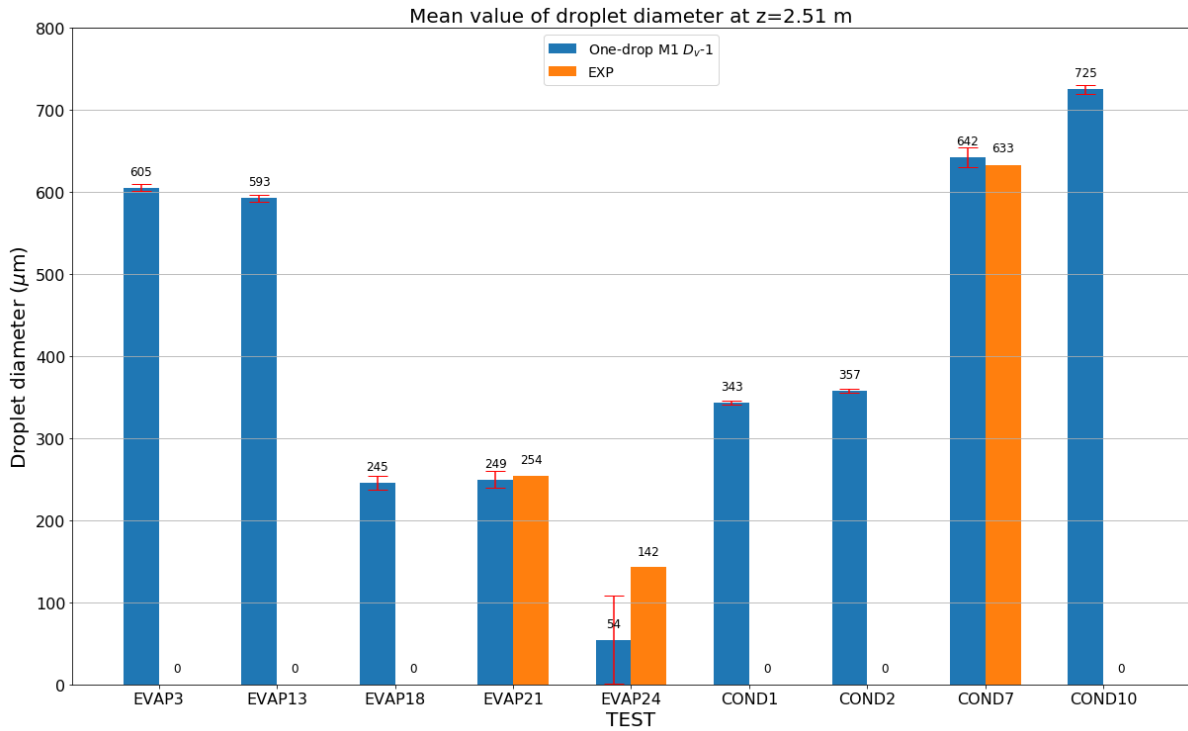


Figure 1.19: Code-experiment comparison: mean value and standard deviation of the droplet diameter at $z = 2.51$ m.

For simplicity, it was decided to use only the M1 model for the mass transfer driving term and the D_v-1 formulation for mass diffusivity.

The graphs show that the tests that produce the biggest statistical error are the same three tests (EVAP18, EVAP21 and EVAP24) for which the biggest discrepancies were found in the two previous subsections.

Also in this case the result is strongly linked to the measurement position considered: the closer we are to the point of complete vaporization of the drop, the higher the rate of vaporization, the greater will be the statistical error produced and the discrepancy compared to the experimental measurement (as seen above).

It can be concluded that the uncertainty about the initial drop diameter produces a larger

statistical error for smaller initial diameters and atmospheric conditions leading to fast vaporization (EVAP18, EVAP21 and EVAP24 tests). With regard to the other tests, the statistical error produced is much smaller, comparable with the error of the experimental measurements and in some cases even smaller.

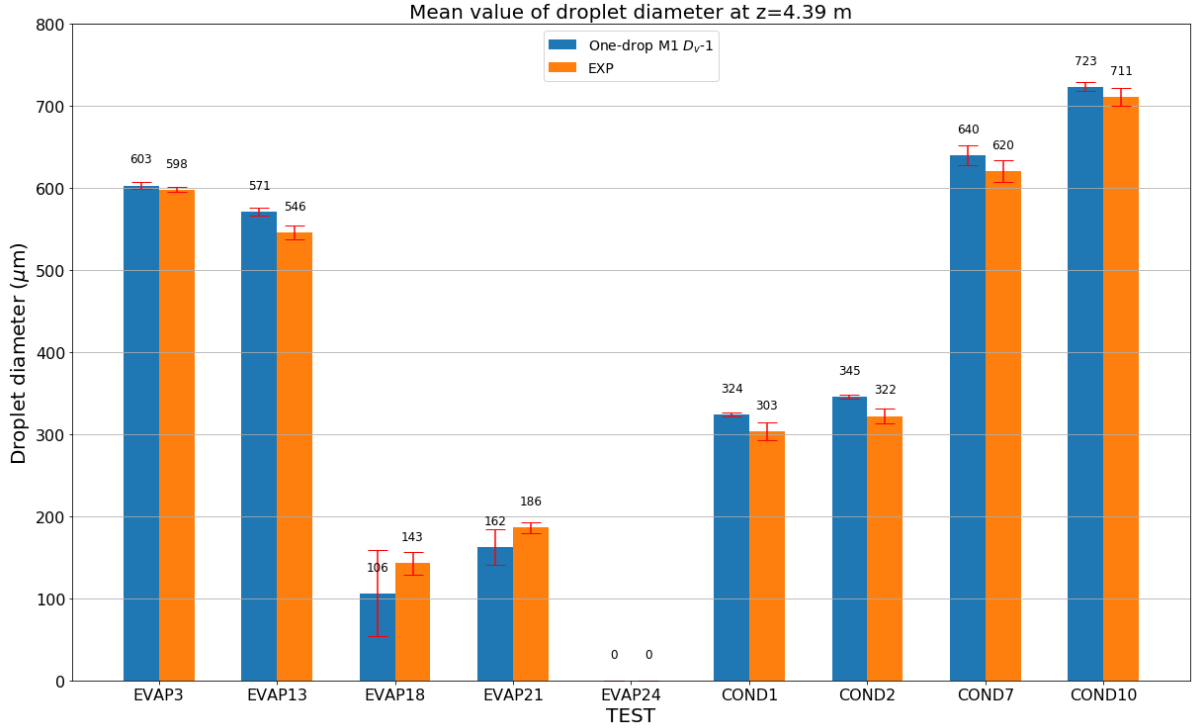


Figure 1.20: Code-experiment comparison: mean value and standard deviation of the droplet diameter at $z = 4.39$ m.

1.6 Spray repartition maps

This section proposes to build parametric maps of the spray repartition for the One-drop model.

1.6.1 Definition of spray repartition

The *spray repartition* x_{spray} can be defined as the ratio between the latent energy (condensation – vaporization) and the total energy (latent + sensible) exchanged between the drop and the atmosphere.

$$x_{\text{spray}} = \frac{Q_{\text{lat,sp}}}{Q_{\text{lat,sp}} + Q_{\text{sens,sp}}} \quad (1.55)$$

The total latent heat exchanged by the spray and the atmosphere, $Q_{\text{lat,sp}}$ (J), is defined as the integral over the entire falling time of the instantaneous latent power ($\dot{m}_d h_{fg}$), see equation 1.56. Since it depends on the mass transfer flow rate \dot{m}_d (if $\dot{m}_d > 0$ we have condensation on the droplet, if $\dot{m}_d < 0$ the droplet is vaporizing), we can have that, overall, condensation has prevailed over vaporization ($Q_{\text{lat,sp}} > 0$) or the opposite ($Q_{\text{lat,sp}} < 0$).

$$Q_{\text{lat,sp}} = \int_0^{t_{\text{end}}} \dot{m}_d h_{\text{fg}} dt = Q_{\text{cond,sp}} - Q_{\text{vap,sp}} \quad (1.56)$$

where t_{end} is the end time of the fall of the single droplet, $Q_{\text{cond,sp}}$ (J) is the fraction of the total latent heat related to condensation (always positive), $Q_{\text{vap,sp}}$ (J) is the fraction of the total latent heat related to vaporization (taken positive, with the minus sign in front because it has to be subtracted due to the definition of \dot{m}_d).

The total sensible heat exchanged by the spray and the atmosphere $Q_{\text{sens,sp}}$ (J) is defined as the integral over the entire falling time of the instantaneous sensible power ($hS(T_g - T_d)$), see equation 1.57. It is always positive as the temperature of the droplet T_d is never higher than that of the gas mixture T_g .

$$Q_{\text{sens,sp}} = \int_0^{t_{\text{end}}} hS(T_g - T_d) dt \quad (1.57)$$

where t_{end} is the end time of the fall of the single droplet.

The table 1.14 summarises how to interpret the x_{spray} values that will be shown in the maps, specifying that $x_{\text{spray}} \leq 1$ (always) and it can also assume negative values, even lower than -1. For completeness in the table we also indicate the case in which $x_{\text{spray}} > 1$ (last row), but this case never occurs in the model calculations.

Table 1.14

x_{spray}	Sensible heat	Latent heat
$x_{\text{spray}} = 1$	$Q_{\text{sens,sp}} = 0$	$Q_{\text{lat,sp}} > 0 \Rightarrow Q_{\text{cond,sp}} > Q_{\text{vap,sp}}$
$0 < x_{\text{spray}} < 1$	$Q_{\text{sens,sp}} > 0$	$Q_{\text{lat,sp}} > 0 \Rightarrow Q_{\text{cond,sp}} > Q_{\text{vap,sp}}$
$x_{\text{spray}} = 0$	$Q_{\text{sens,sp}} > 0$	$Q_{\text{lat,sp}} = 0 \Rightarrow Q_{\text{cond,sp}} = Q_{\text{vap,sp}}$
$-1 < x_{\text{spray}} < 0$	$Q_{\text{sens,sp}} > -2 \cdot Q_{\text{lat,sp}}$	$Q_{\text{lat,sp}} < 0 \Rightarrow Q_{\text{cond,sp}} < Q_{\text{vap,sp}}$
$x_{\text{spray}} = -1$	$Q_{\text{sens,sp}} = -2 \cdot Q_{\text{lat,sp}}$	$Q_{\text{lat,sp}} < 0 \Rightarrow Q_{\text{cond,sp}} < Q_{\text{vap,sp}}$
$x_{\text{spray}} < -1$	$-Q_{\text{lat,sp}} < Q_{\text{sens,sp}} < -2 \cdot Q_{\text{lat,sp}}$	$Q_{\text{lat,sp}} < 0 \Rightarrow Q_{\text{cond,sp}} < Q_{\text{vap,sp}}$
$x_{\text{spray}} > 1$	$0 < Q_{\text{sens,sp}} < -Q_{\text{lat,sp}}$	$Q_{\text{lat,sp}} < 0 \Rightarrow Q_{\text{cond,sp}} < Q_{\text{vap,sp}}$

1.6.2 Input parameters and case study

As already mentioned, the purpose of this section is to construct parametric maps for x_{spray} , a kind of look-up tables that can be used by any user to determine, even by interpolation, the value of x_{spray} for a given combination of parameters.

In our case, the maps are built by creating possible combinations between three parameters on which x_{spray} depends: total pressure of the gas mixture P , air partial pressure P_{air} and superheating degree ΔT_{sat} .

$$x_{\text{spray}} \text{ MAPS} \rightarrow x_{\text{spray}}(P, P_{\text{air}}, \Delta T_{\text{sat}}) \quad (1.58)$$

These parameters are those that determine the atmospheric conditions. The number of parameters can be increased by including a parametrization also on the initial conditions of

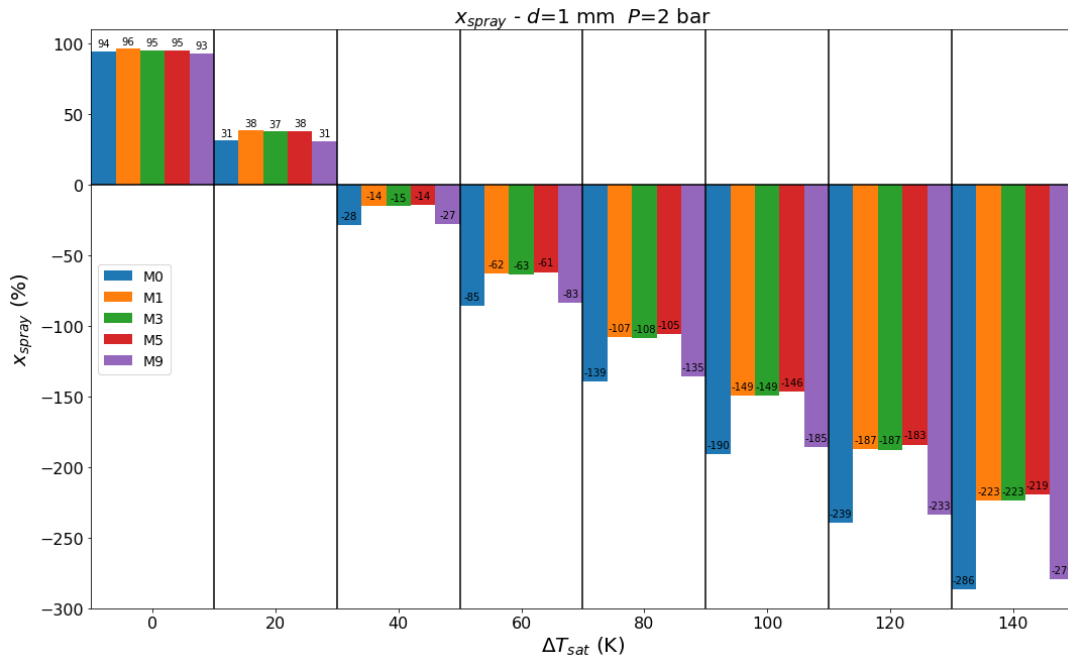
the drop (e.g. $x_{\text{spray}}(P, P_{\text{air}}, \Delta T_{\text{sat}}, d_0, T_{d,0}, v_{d,0})$), but, for simplicity, it has been decided to consider fixed conditions for the initial diameter, temperature and speed of the drop.

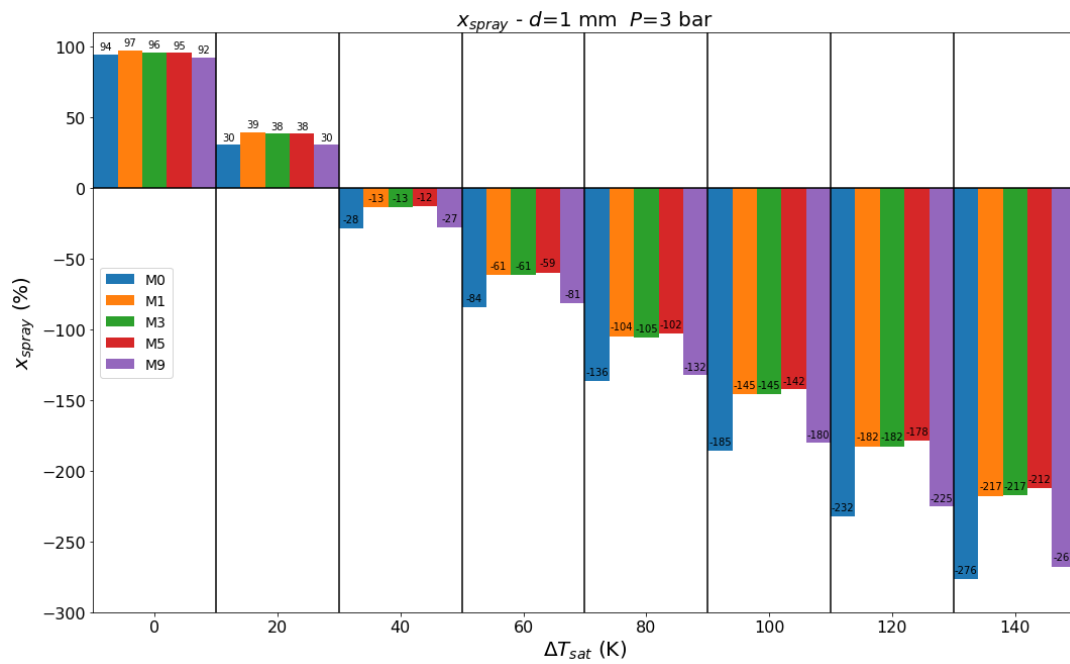
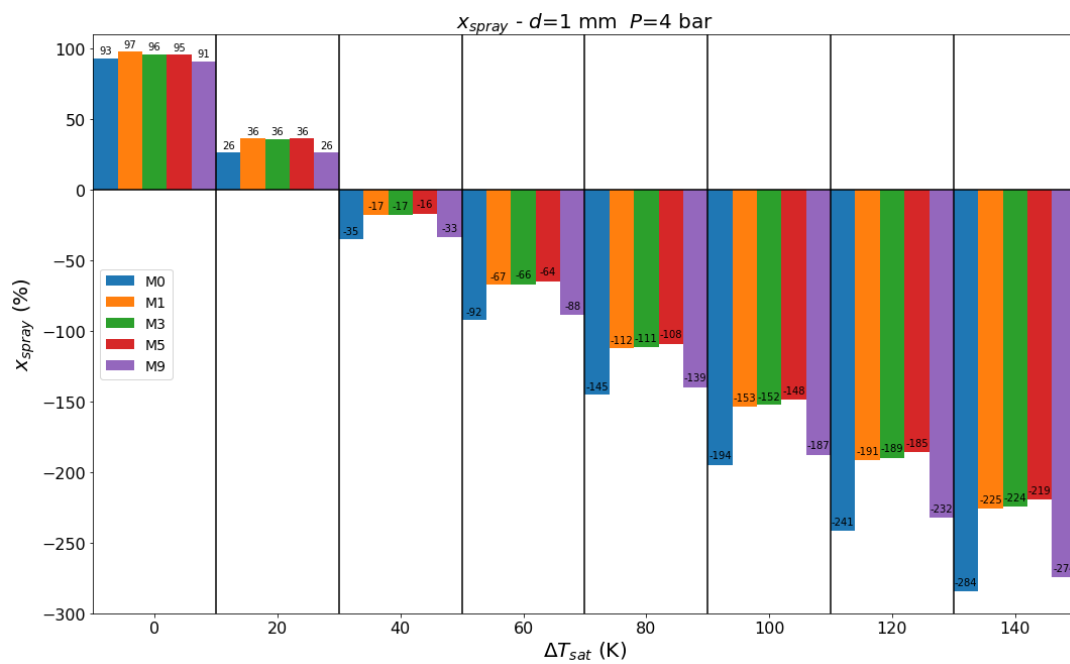
Table 1.15

	Input parameters
Atmosphere	$P = 0.8 \div 6 \text{ bar}$ with $\Delta P = 0.4 \text{ bar}$
	$P_{\text{air}} = 0.8 \div 6 \text{ bar}$ with $\Delta P_{\text{air}} = 0.4 \text{ bar}$
	$\Delta T_{\text{sat}} = 0 \div 200 \text{ }^\circ\text{C}$ with $\Delta(\Delta T_{\text{sat}}) = 20 \text{ }^\circ\text{C}$
Droplet	$d_0 = 1 \text{ mm}$ $T_{d,0} = 20 \text{ }^\circ\text{C}$ $v_{d,0} = 15 \text{ m/s}$
Falling height	$D_{\text{fall}} = 20 \text{ m}$
Time-step	$\Delta t = 0.01 \text{ s}$

Remembering that Dalton's law is always valid, so, for each combination of total pressure P and partial pressure of air P_{air} , the partial pressure of the steam P_{steam} is automatically determined through the relation $P = P_{\text{air}} + P_{\text{steam}}$. Obviously, to be physically consistent, all combinations between P and P_{air} are created respecting the condition $P > P_{\text{air}}$.

- Some extrapolation of the x_{spray} maps are shown below, with the following conditions: $P = (2, 3, 4, 5) \text{ bar}$, $P_{\text{air}} = 1 \text{ bar}$, $\Delta T_{\text{sat}} = (0, 20, 40, \dots, 100, 120, 140) \text{ }^\circ\text{C}$, M0/M1/M3/M5/M9 models for the mass transfer driving term, $D_v=0$ formulation for the mass diffusivity.

Figure 1.21: x_{spray} (%) map for $P = 2 \text{ bar}$ and $P_{\text{air}} = 1 \text{ bar}$.

Figure 1.22: x_{spray} (%) map for $P = 3$ bar and $P_{\text{air}} = 1$ bar.Figure 1.23: x_{spray} (%) map for $P = 4$ bar and $P_{\text{air}} = 1$ bar.

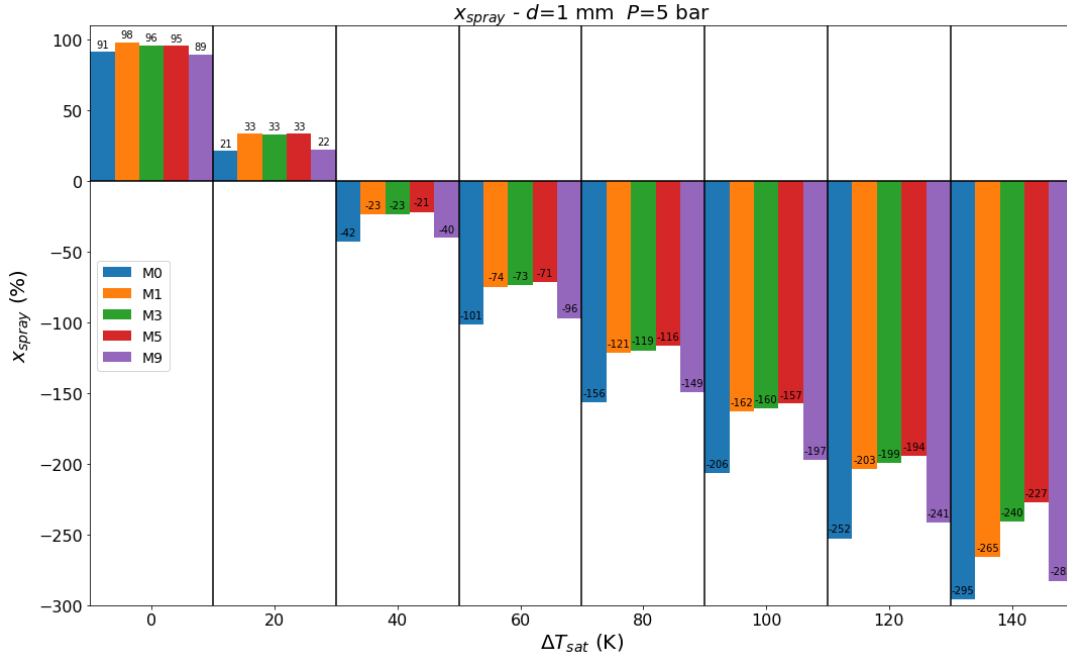


Figure 1.24: x_{spray} (%) map for $P = 5$ bar and $P_{\text{air}} = 1$ bar.

The graphs clearly show that, for each pressure level considered, x_{spray} decreases almost linearly as the superheating degree increases. In particular, it can be noted that the M0 and M9 models (both based on density gradients) show similar results, but lower values than those obtained with the M1, M3 and M5 models (based on mass fraction gradients). The difference becomes increasingly significant as the superheating degree increases. In general, for all cases, it can clearly be observed that the closer you get to the saturation conditions of the atmosphere ($\Delta T_{\text{sat}} = 0$ K), the more you have that the condensation phenomenon prevails over the vaporisation phenomenon ($x_{\text{spray}} > 90\%$), while moving away from the saturation conditions the vaporisation starts to prevail more and more over the condensation.

- Two more maps in the form of 2D maps are shown below, in which x_{spray} is represented simultaneously as a function of the total pressure P (and the steam mole fraction X_{steam}) and the superheating degree ΔT_{sat} . A fixed value is considered for the partial pressure of air ($P_{\text{air}} = 1$ bar) and the results obtained with the M0 model are compared with those of the M1 model, using $D_{\text{v}-1}$ as a formulation for diffusivity.

For this representation it has been chosen to show only the results obtained with the M0 and M1 models, since, from the previous analyses, they are quite representative also for the M9 and M3/M5 models, respectively. As far as the mass diffusivity is concerned, it has been chosen to represent only the case with $D_{\text{v}-1}$, because the difference with the other two formulations ($D_{\text{v}-0}$ and $D_{\text{v}-2,3}$) is not appreciable.

As seen in the previous graphs, here too it is clear that, fixing the amount of steam in the atmosphere (fixed X_{steam}), x_{spray} decreases as the superheating degree increases. The behaviour of x_{spray} as a function of P (and X_{steam}), with fixed ΔT_{sat} , is not linear: x_{spray} increases for $1.2 < P < 2.5$ bar ($0.17 < X_{\text{steam}} < 0.6$), reaches the maximum value at $P \approx 2.5$ bar ($X_{\text{steam}} \approx 0.6$), then decreases for higher values.

The difference between the two models, M0 and M9, becomes more significant as the superheating degree increases, in particular x_{spray} for the M0 model reaches lower values than the M1 model: for example, for M0, $x_{\text{spray}} \approx -308\%$ at $P = 1.2$ bar and $\Delta T_{\text{sat}} = 0$ K, while, in the same conditions, $x_{\text{spray}} \approx -243\%$ for M1.

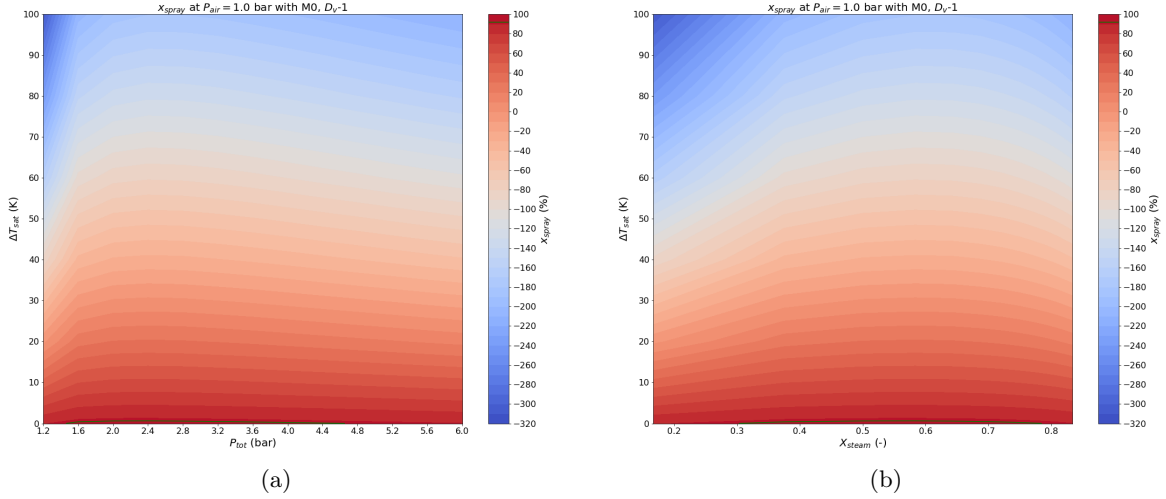


Figure 1.25: Spray repartition (%) 2D map, (a) $x_{\text{spray}}(P, \Delta T_{\text{sat}})$ and (b) $x_{\text{spray}}(X_{\text{steam}}, \Delta T_{\text{sat}})$, with $X_{\text{steam}} = P_{\text{steam}}/P$ and $P = P_{\text{steam}} + P_{\text{air}}$. Conditions: $P = 1.2 \div 6$ bar, $P_{\text{air}} = 1$ bar, $\Delta T_{\text{sat}} = 0 \div 100$ °C, M0 model, D_V-1 formulation. The green line corresponds to $x_{\text{spray}} = 92\%$.

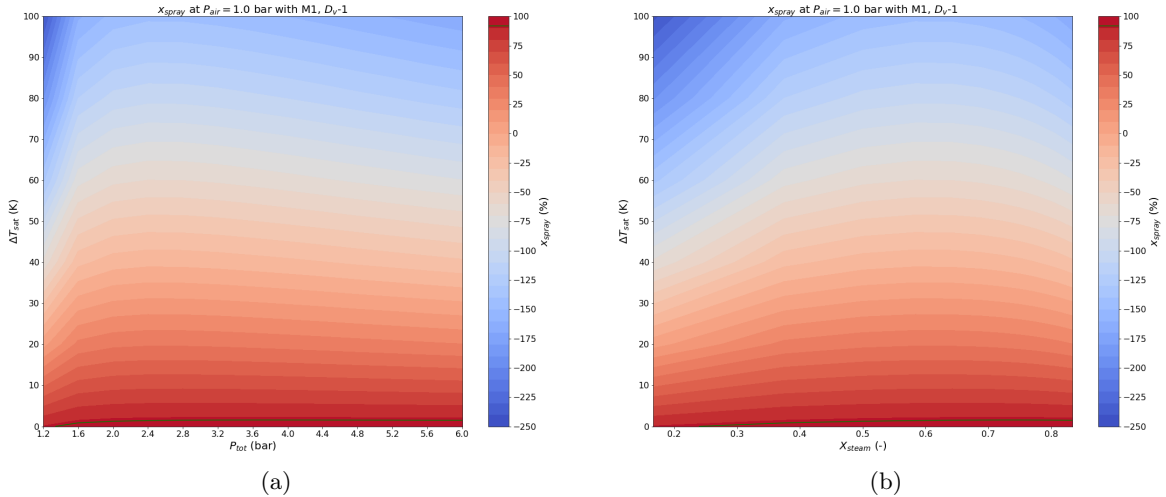


Figure 1.26: Spray repartition (%) 2D map, (a) $x_{\text{spray}}(P, \Delta T_{\text{sat}})$ and (b) $x_{\text{spray}}(X_{\text{steam}}, \Delta T_{\text{sat}})$, with $X_{\text{steam}} = P_{\text{steam}}/P$ and $P = P_{\text{steam}} + P_{\text{air}}$. Conditions: $P = 1.2 \div 6$ bar, $P_{\text{air}} = 1$ bar, $\Delta T_{\text{sat}} = 0 \div 100$ °C, M1 model, D_V-1 formulation. The green line corresponds to $x_{\text{spray}} = 92\%$.

Chapter 2

H&M transfers between the structures and the atmosphere

Contents

2.1	Review of key physical phenomena	59
2.1.1	Liquid film component	61
2.1.2	Diffusive gas boundary layer component	61
2.1.3	Bulk flow	62
2.1.4	Geometric configuration	63
2.2	Working perimeter	63
2.3	H&M transfers models	63
2.3.1	Mechanistic model: Chilton and COPAIN correlations	63
2.3.2	Historical model: Tagami and Uchida correlations	66
2.4	Implementation	68
2.5	Validation of the models	69
2.5.1	Delhaye problem	69
2.5.2	Benteboula-Dabbene: Test-1	73
2.6	Condensation ratio maps	78
2.6.1	Definition of condensation ratio	78
2.6.2	Input parameters and case study	78

2.1 Review of key physical phenomena

Gen III and III+ reactors have safety systems based on natural circulations, so the study of *condensation phenomena* on the containment structure and walls is really essential as it represents one of the thermohydraulic phenomena that characterize the operation of passive emergency systems in the nuclear reactors of new generation. [13]

The *containment structures* represent a way to keep the *containment integrity*: they are made of metal which transports latent heat from the condensing steam to another fluid located out of the containment. Considering that condensation has high sensitivity to *boundary conditions*,

thermal-hydraulic predictions are needed. [13] The *containment walls* are made from reinforced concrete and steel up to 1.5 m thick.

In order to study the phenomena and the relevant parameters that affect the *condensation scenario*, it is introduced a *boundary layer approximation* (see figure 2.1). This approximation is possible because in the case of steam condensation the highest gradients are in normal direction to the surface (containment walls) for the properties and the parameters of the gas mixture (air + steam). It is considered the build up of two different *boundary layer films* near the wall: condensate film and gaseous film. [13]

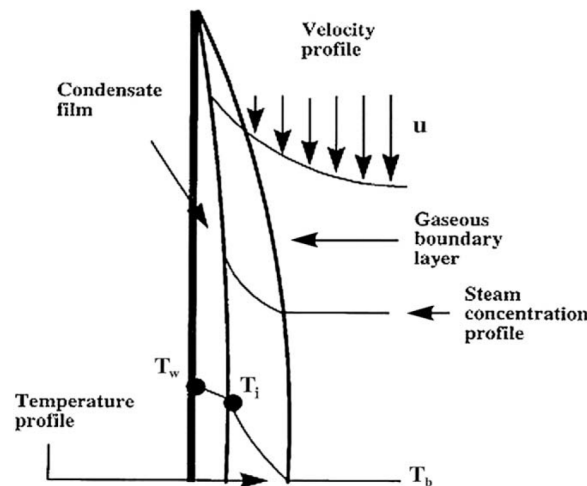


Figure 2.1: Film condensation with noncondensables in a wall. [13]

On the wall there is the build up of a thin film of condensate that is called *condensate layer*, next to this layer there is the *gaseous diffusion layer* (mixture of steam and noncondensables). The two layers interact at the interface. They are characterized by different phenomena and variables, so they can be characterized separately through specific non-dimensional numbers and parameters. [13]

1. *Condensate film*: film closer to the wall, characterized by condensed steam. The condensate flows in direction of gravity. The velocity profile and the interfacial resistance cause small waves development at the interface (if $Re > 30$) that cause the increase of the heat transfer, but, due to the small thickness, we can neglect convective momentum and energy transfers towards the wall. Sometimes also the film thermal resistance is neglected. [13]
2. When condensation starts, the noncondensables accumulates towards the interface, so the steam is forced to diffuse through the barrier of n.c. gases, this causes the build up of *concentration gradient* across the gaseous boundary layer. Natural circulation in the containment causes n.c. gases flows downwards driven by gravity, so that n.c. fraction increases descending along the wall not only because of the condensation of steam, but also due to the buoyancy force. [13]
3. *Phenomena beyond condensation* to be considered: position of the injection of the steam, presence of volatile gases, etc. [13]

The *phenomenological study* consists in the study of the phenomena and variables that affect the *condensation* and the HTC (heat transfer coefficient). [13]

Three boundary layers are taken into consideration [13]:

1. Condensate boundary layer
2. Gaseous diffusion boundary layer
3. Containment atmosphere

2.1.1 Liquid film component

The main phenomena that involve the liquid film component are the following [13]:

- *Liquid film convection and inertia*
- *Interfacial resistance*: evaluation of interface properties, steam partial pressure, saturation conditions. It is necessary to define an interface temperature.
- *Subcooling effect (wall temperature)*: influence of the wall temperature on the HTC and vice versa.

Example 1: increasing the superheating degree, the HTC increases and it is balanced by the subcooling effect that causes a reduction of the HTC.

Example 2: if the wall temperature decreases, the interface temperature decreases (effect on the saturation temperature and on the steam partial pressure at the interface). This leads to the decrease of the mass fraction of steam at the interface.

- *Interfacial share*: interfacial friction factor formulation needed.
- *Structure of the surface*: usually added to the classical Nusselt formulation of the liquid film HTC.
Example: if a wave structure is formed on the film ($Re > 30$), the heat transfer increases because of two main factors: 1. The surface is increased; 2. The inertia creates instabilities that lead to an increase in the homogeneity of the temperature gradients and a reduction of the thermal resistance thickness, leading to an improvement of the HTC.
- *Condensate film*: this is one of the key points where a total disagreement is found. This disagreement is especially caused mainly by the specific boundary conditions in the experimental facility where the relative contribution of the thermal resistance to the HTC is analyzed.
- *Dropwise condensation*: it is one of the most difficult phenomenon to model.

2.1.2 Diffusive gas boundary layer component

The main phenomena that involve the diffusive gas boundary layer component are the following [13]:

- *Thermal diffusion*: diffusive mass transport due to temperature gradients.
- *Diffusion thermo*: energy transport due to a concentration gradient.
- *Variability of the properties in the diffusive boundary layer*

- *Superheating*: influence of the gas temperature on condensation. In general, increasing the superheating has a positive influence on the HTC.
- *Difference of temperatures*: effects of thermal jumps on the HTC and on the heat flux. In general, HTC decreased with the thermal jump with a negative quasi-linear slope, while the flux increased logarithmically.
- *Noncondensables*: there is a categorical agreement that the presence of noncondensable gases is the most influencing condition on steam condensation. When they are dragged to the interface, they start accumulating forming a barrier to the vapour that strongly modifies the nature of the condensation phenomenon.
- *Suction*: it is the modification of the heat and mass transport phenomena due to the existence of an additional convective term in the species equation. This term is obviously caused by wall condensation. The direct consequence is a positive contribution to the heat and mass transfer, causing the concentration boundary layer to be thinner.

2.1.3 Bulk flow

The main phenomena that involve the bulk flow are the following [13]:

- *Circulation pattern and fluid flow*: influence of the gas flow regime (natural/forced, laminar/turbulent) on condensation.
- *Homogeneous condensation (mist)*: considering conservation equations without saturation conditions of steam, a supersaturated steady-state develops along the boundary layer (steam mass fraction is higher than steam mass fraction at saturation). While, considering equilibrium conditions (saturation), we have anticipated condensation effect (important only if the temperature difference ($T_{\text{bulk}} - T_{\text{wall}}$) is high, and Lewis number $Le = \alpha/D > 1$, where α (m^2/s) is the thermal diffusivity and D (m^2/s) is the mass diffusivity). It has a direct influence on HTC. Some authors propose to write conservation equations considering equilibrium and latent heat transfer (increasing T_{bulk}) adding the fraction of the latent heat absorbed by the mist. If ($T_{\text{bulk}} - T_{\text{wall}}$) is too high ($\sim 70^\circ\text{C}$) the equilibrium model cannot be considered suitable, causing the HTC to be underestimated of $\sim 50\%$. Different authors propose different results, but they agree on the fact that the HTC is reduced by the formation of mist: homogeneous condensation causes T_{bulk} increase so that, considering a constant heat flow, HTC decreases as condensed drops start to appear.
- *Presence of light gases*
Example: presence of hydrogen due to the oxidation of the fuel cladding at high temperatures causes modification in flow distribution and condensation heat and mass transfer process.
- *Hydrodynamic condition of the gas (P, T_{sat}, v)*
Example: increasing T_{sat} with a constant steam mass fraction causes P increase, so the driving force increases (in terms of density gradients).
Example: increasing diffusion coefficient causes P decrease.
 The total pressure P affects strongly the properties of the gas components and also the gas velocity v affects a lot condensation, but it is difficult to quantify the effect in case of natural circulation conditions.

2.1.4 Geometric configuration

The main phenomena that involve the geometric configuration of the containment are the following [13]:

- *Leaning of the wall*: it can affect the type of condensation (dropwise versus film), it can lead to the disruption in the continuity of the barrier of noncondensable gases when the drops detach from the wall, causing modification of the interfacial structure and consequent effects on HTC (depending on the leaning angle). In this work the walls are considered vertical.
- *Length of the wall*: it is the only parameter whose relation respect to condensation is positive or negative according to the circulation pattern of the gas. In the forced circulation case, the HTC is inversely proportional to the length of the wall, whereas direct proportionality occurs in the case of natural circulation.
- *Heat transfer in the annulus of the containment*: it can be important to address the effect of the secondary side of the containment atmosphere, which is the system consisted of a water falling on the external side of the steel wall of the containment, and the air that circulates by natural circulation between the concrete and the steel wall (the annulus of the containment). This phenomenon will modify the heat and mass transfer processes in the atmosphere containment by means of modifying the exact value of the wall temperature, as well as its temporal evolution.

2.2 Working perimeter

The working perimeter of the study of this chapter is basically the same, as regard the containment atmosphere conditions, as that defined in section 1.2 for the H&M exchanges between the CSS drops and the atmosphere. These conditions are based on the safety studies carried out, the geometric characteristics of the reactor buildings and the characteristics of the safety systems for the pressurized water reactors of the French nuclear power plants in operation.

Information characterising the containment building must be added: typically the volume of the building is about 50 000 m³ [3]-[6], it is made from reinforced concrete and steel and the walls are 1-1.5 m thick. The initial (before the accident) surface temperature of the walls can be in the order of 40-45 °C.

2.3 H&M transfers models

The heat and mass transfer model used in this work is based on correlations for condensation in the presence of noncondensable gases based on the heat and mass transfer analogy. [5]

2.3.1 Mechanistic model: Chilton and COPAIN correlations

The correlations used in the mechanistic model are established in the turbulent convection regime and are used here considering natural circulation pattern. The hypotheses taken into account are the following. [5]

- At the liquid-steam interface: $P_{v,i} = P_{\text{sat}}(T_i)$, saturated state. $P_{v,i}$ (Pa) is the pressure of steam at the interface, $P_{\text{sat}}(T_i)$ (Pa) is the steam saturation pressure at the interface temperature T_i (K).
- Film thermal resistance is neglected: $T_w = T_i$, where T_w (K) is the wall temperature (on the internal surface of the containment).
- Physical properties of the gas mixture are evaluated at the bulk temperature T_b (K).
- Composition of noncondensable gas mixture equal to the composition at the interface.
- Density of n.c. gases at the interface evaluated through the perfect gas law: $\rho_{\text{nc},i} = (P - P_{v,i})/(r_{\text{nc},i}T_i)$, where $\rho_{\text{nc},i}$ (kg/m³) is the noncondensables density at the interface, P (Pa) is the total pressure of the containment (bulk), $r_{\text{nc},i}$ (J/kg/K) is the specific gas constant for noncondensables at the interface.

These correlations involve further models and assumptions to determine the gas mixture physical properties such as the diffusion coefficient (see subsection 1.3.1.2), viscosity and conductivity. These assumptions will be specified in the next section.

Below the definition of the heat flux on the wall q_w (W/m²) is provided. It can be divided into two contribution: the convection heat flux q_{cv} (W/m²) and the condensation heat flux q_{cd} (W/m²). Each of these contributions is associated with a heat transfer coefficient, h_{cv} and h_{cd} (W/m²/K), respectively. The correlations presented provide a method to obtain these heat transfer coefficients. [5]

$$q_w = q_{cv} + q_{cd} = H_{\text{tot}}(T_b - T_w) \quad (2.1)$$

$$q_{cv} = h_{cv}(T_b - T_w) \quad (2.2)$$

$$q_{cd} = \dot{m}_{v,i}''(h_{v,b} - h_{l,w}) = h_{cd}(T_b - T_w) \quad (2.3)$$

$$h_{v,b} = h_v(P_{v,b}, T_b) \quad h_{l,w} = h_l(P, T_w) \quad (2.4)$$

$$\dot{m}_{v,i}'' = -\frac{\rho D}{1 - Y_{v,i}} \left(\frac{\partial Y_{v,i}}{\partial y} \right) = k_{cd} \frac{\rho(Y_{v,b} - Y_{v,i})}{1 - Y_{v,i}} \quad (2.5)$$

where $H_{\text{tot}} = h_{cv} + h_{cd}$ (W/m²/K) is the total heat transfer coefficient, $\dot{m}_{v,i}''$ (kg/m²/s) is the condensation mass flux (steam mass velocity at the interface), $h_{v,b}$ (J/kg) is the steam specific enthalpy evaluated at the bulk steam pressure $P_{v,b}$ (Pa) and the bulk temperature, $h_{l,w}$ (J/kg) is the liquid (water) specific enthalpy evaluated at the bulk pressure and the wall temperature, ρ (kg/m³) is the gas mixture density at bulk conditions, D (m²/s) is the mass diffusivity, $Y_{v,i}$ (-) is the steam mass fraction at the interface, $Y_{v,b}$ (-) is the steam mass fraction at bulk conditions. In equation 2.5, the condensation mass flux is expressed as a function of the condensation mass transfer coefficient k_{cd} (m/s). [5]

Two correlations, Chilton and COPAIN, usefull to find the convection heat transfer coefficient h_{cv} and the condensation mass transfer coefficient k_{cd} are proposed below.

2.3.1.1 Chilton correlation

The Chilton correlation is based on the Chilton–Colburn analogy which gives the mass transfer coefficient depending on the heat transfer one. [5]

$$k_{cd} = h_{cv}(\rho C_p)^{-1/3} \left(\frac{Pr}{Sc} \right)^{2/3} \quad (2.6)$$

where C_p (J/kg/K) is the gas mixture specific heat at constant pressure, Pr (-) is the Prandtl number, Sc (-) is the Schmidt number.

To obtain a formulation for the h_{cv} one can start from its definition as a function of the Nusselt number Nu (-) and write similarly the definition of k_{cd} as a function of the Sherwood number Sh (-).

$$h_{cv} = \frac{\lambda Nu}{L} \quad k_{cd} = \frac{D Sh}{L} \quad (2.7)$$

where λ (W/m/K) is the gas mixture conductivity, L (m) is the characteristic length, D (m²/s) is the mass diffusivity.

The Nusselt number can be obtained with the Mac-Adams correlation for free convection on vertical plate, while the Sherwood number can be obtained taking advantage of the HMT (Heat and Mass Transfer) analogy. [5]

$$Nu = 0.13(Gr Pr)^{1/3} \quad Sh = 0.13(Gr Sc)^{1/3} \quad (2.8)$$

Pr , Sc and Gr (Grashof number) are evaluated for the gas at bulk conditions.

$$Pr = \frac{\mu}{\rho\alpha} \quad Sc = \frac{\mu}{\rho D} \quad Gr = \rho g \frac{\rho_w - \rho}{\mu^2} L^3 \quad (2.9)$$

where μ (Pa · s) is the gas mixture dynamic viscosity, g (m/s²) is gravitational acceleration, ρ_w (kg/m³) is the gas mixture density near the wall (interface conditions).

Assuming $Pr = 1$, it is possible to write the two following formulations for h_{cv} and k_{cd} . [5]

$$h_{cv} = 0.13\lambda \left(g\rho \frac{\rho_w - \rho}{\mu^2} \right)^{1/3} \quad k_{cd} = \frac{D^{2/3}}{\lambda} \left(\frac{\mu}{\rho} \right)^{1/3} h_{cv} \quad (2.10)$$

2.3.1.2 COPAIN correlation

The COPAIN correlation is based on the HMT analogy, as the Chilton one. The main difference with the Chilton correlation is that it is based on the application of an experimental correction factor θ to the calculation of Nusselt and Sherwood numbers. This correction factor has the aim to overcome the lack of modeling such as the suction and the film effects. Another important difference is that the Prandtl number is not taken equal to one, but it is calculated as in equation 2.9. [5]

$$Nu = 0.13 \cdot \theta \cdot (Gr_h Pr)^{1/3} \quad Sh = 0.13 \cdot \theta \cdot (Gr_h Sc)^{1/3} \quad (2.11)$$

The Schmidt number is calculated as in equation 2.9, while Gr_h (-) is the hybrid Grashof number, calculated as shown in equation 2.12. [5]

$$Gr_h = \frac{\rho^2 g L^3}{\mu^2} \left(1 - \frac{T_w}{T_b} + \frac{Y_{nc,i} - Y_{nc,b}}{\frac{MW_{nc}}{MW_{nc} - MW_v} - Y_{nc,b}} \right) \quad (2.12)$$

where $Y_{nc,i}$ (-) is the noncondensables mass fraction at the interface, $Y_{nc,b}$ (-) is the noncondensables mass fraction at the bulk conditions, MW_{nc} (g/mol) is the noncondensables (air in our case) molecular weight, MW_v (g/mol) is the steam (water) molecular weight.

The correction factor θ is experimental in the sense that this correlation has been in the framework of the experimental program carried out in the CEA on wall condensation in the COPAIN facility [5]. It can be calculated through the following expression.

$$\theta = 0.8254 + 0.616 \frac{X_{nc,i} - X_{nc,b}}{X_{nc,i}} \quad (2.13)$$

where $X_{nc,i}$ (-) is the noncondensables mole fraction at the interface, $X_{nc,b}$ (-) is the noncondensables mole fraction at the bulk conditions.

2.3.2 Historical model: Tagami and Uchida correlations

The historical (conservative) model for wall condensation is based on the 92/8 (%) repartition recommended by the U.S. Nuclear Regulatory Commission (NRC) in the NUREG-0588 report [7]. The assumption is that, when the atmosphere of the containment building is superheated, a maximum of 8 % of the condensate remains in the vapour region, in other words that 92 % of the heat flux exchanged between the atmosphere and the condensate is due to the steam condensation process (on the walls of the building in the case of *wall condensation*, or on the drop of liquid in the case of *heat exchange between the atmosphere and the CSS drops*, as described in the previous chapter), while the rest of the heat flux is of *sensible* nature. While, in the case of an atmosphere in saturation conditions or below, the assumption says that the heat is totally exchanged by condensation (only *latent* contribution), while the sensible contribution is equal to zero, so in this case we are talking about 100/0 (%) repartition. [7]

The heat flux exchanged between the wall and the atmosphere q_w can be redefined, as in equation 2.1, but this time introducing only the total heat transfer coefficient H_{tot} .

$$q_w = H_{tot}(T_b - T_w) \quad (2.14)$$

Considering a superheated atmosphere, one can write the following heat flux repartition, taking advantage of the historical assumption 92/8.

$$q_{cd} = 0.92 \cdot q_w \quad q_{cv} = 0.08 \cdot q_w = q_w - q_{cd} \quad (2.15)$$

remembering that q_{cd} is the condensation heat flux (latent contribution), while q_{cv} is the convection heat flux (sensible contribution).

While in the case of a saturated (or below saturation) atmosphere, the repartition can be written as follows.

$$q_{cd} = q_w \quad q_{cv} = 0 \quad (2.16)$$

In order to calculate the total heat transfer coefficient H_{tot} , it is proposed to use two correlations: Tagami correlation and Uchida correlation. [5]

$$H_{\text{tot}}^{\text{Tagami}} = 11.256 + 283.9 \left(\frac{Y_{\text{v,b}}}{Y_{\text{nc,b}}} \right) \quad (2.17)$$

$$H_{\text{tot}}^{\text{Uchida}} = 379 \left(\frac{Y_{\text{v,b}}}{Y_{\text{nc,b}}} \right)^{0.707} \quad (2.18)$$

Both of them are based on the ratio between the steam mass fraction at bulk conditions $Y_{\text{v,b}}$ and the noncondensables mass fraction at bulk conditions $Y_{\text{nc,b}}$.

2.4 Implementation

To proceed with the validation of the wall condensation model, two different Python codes have been developed: in the first code the wall condensation model is implemented to reproduce two case studies (Delhaye problem 11.2 [6] and Benteboula-Dabbene: Test-1 [5]) taken from the literature, these require the introduction of a model capable of reproducing the temporal evolution of pressure and temperature inside the containment building taking into account the wall condensation phenomenon (the detailed development of this model is presented in the next chapter, subsection 3.1.2); the second code instead carries out a one-way calculation on the model, that is a parametric analysis with which to construct the condensation ratio maps (similarly to what was done with the spray repartition maps).

Once the pressure and temperature conditions of the containment building have been fixed, the two codes have in common the calculation procedure for the heat exchange between the atmosphere and the walls of the building.

-• Mechanistic model

The calculation process for the mechanistic model is the following:

1. Set the input parameters, initialize the variables and define the constants.
2. Identify the containment conditions: total pressure, temperature, relative humidity (mass of steam), superheating degree. For this step, two approaches can be followed: if you are dealing with the reproduction of a containment test case (like Delhaye problem 11.2 or Benteboula-Dabbene: Test-1), you need to calculate iteratively at each time-step the new containment conditions solving the balance equations; whereas if you want to build the condensation ratio maps, it is just necessary to scan the various sets of input parameters to perform the one-way calculations.
3. Calculate the gas mixture density ρ , the noncondensables (air) density at the interface $\rho_{nc,i}$ and the gas mixture density on the wall (at the interface) ρ_w .

$$\rho = \rho_{air} + \rho_{steam} \quad (2.19)$$

where ρ_{air} is the air partial pressure and it is assumed constant.

$$\rho_{nc,i} = \frac{P - P_{v,i}}{r_{nc,i} T_i} \quad (2.20)$$

$$\rho_w = \rho_{nc,i} + \rho_{steam,i} \quad (2.21)$$

where $\rho_{steam,i}$ is the steam density at the interface, it is calculated with the IAPWS tables as the steam saturation density at the interface temperature $T_i = T_w$.

$$\rho_{steam,i} = \rho_{sat}(T_i, x = 1) \quad (2.22)$$

where x (-) is the steam quality.

4. Calculate the steam/air mole/mass fractions, both at bulk conditions and at the interface.

$$X_{v,b} = \frac{P_{v,b}}{P} \quad X_{air,b} = 1 - X_{v,b} \quad (2.23)$$

$$Y_{v,b} = \frac{X_{v,b}}{X_{v,b} + (1 - X_{v,b})(MW_{steam}/MW_{air})} \quad Y_{air,b} = 1 - Y_{v,b} \quad (2.24)$$

$$X_{v,i} = \frac{P_{v,i}}{P} \quad X_{air,i} = 1 - X_{v,i} \quad (2.25)$$

$$Y_{v,i} = \frac{X_{v,i}}{X_{v,i} + (1 - X_{v,i})(MW_{steam}/MW_{air})} \quad Y_{air,i} = 1 - Y_{v,i} \quad (2.26)$$

5. Assumption on air composition for the calculation of the mass diffusivity: air can be considered as composed only of nitrogen and oxygen, with the following mole and mass fractions (at bulk conditions).

$$X_{N_2} = 0.79 \cdot X_{air,b} \quad X_{O_2} = 0.21 \cdot X_{air,b} = 1 - X_{N_2} \quad (2.27)$$

$$Y_{N_2} = 0.77 \cdot Y_{air,b} \quad Y_{O_2} = 0.23 \cdot Y_{air,b} = 1 - Y_{N_2} \quad (2.28)$$

The next step consists in the calculation of the mass diffusivity by choosing between two of the three formulations in table 1.1: D_v -1 or D_v -2,3, that are the two suggested to reproduce the Test-1 in [5].

6. Calculate the convection heat transfer coefficient h_{cv} and the condensation mass transfer coefficient k_{cd} : choose between Chilton and COPAIN correlation. The results will be identified as a function of the chosen correlation (Chilton or COPAIN) and as a function of the formulation used for the calculation of mass diffusivity (-1 or -2,3).

$$\text{Chilton-1} \quad \text{Chilton-2,3} \quad \text{COPAIN-1} \quad \text{COPAIN-2,3}$$

7. Proceed with the evaluation of $h_{v,b}$ and $h_{l,w}$, as shown in equation 2.4, using the IAPWS tables. Calculate $\dot{m}''_{v,i}$, q_{cv} , q_{cd} and q_w , as shown in equations 2.5, 2.2, 2.3 and 2.1, respectively.

-• Historical model

The calculation process for the historical model is basically similar to the one just presented for the mechanistic model, mainly what differs from the latter are the correlations used for the calculation of the total heat transfer coefficient H_{tot} : Tagami and Uchida. The use of this model does not require the calculation of the mass diffusivity nor the calculation of the mass fractions at the interface, since the correlations depend only on the properties of steam and air at the bulk conditions.

2.5 Validation of the models

This section presents the validation of the wall condensation model by trying to reproduce two case studies proposed in the literature: Delhay problem 11.2 [6] and Benteboula-Dabbene: Test-1 [5].

2.5.1 Delhay problem

The Delhay problem 11.2 [6] is entitled as *Pressure increase in the reactor building of a PWR in case of large break LOCA* (original title in french: *Montée en pression d'une enceinte REP en situation d'APRP grosse brèche*).

The containment building taken into consideration has volume $V = 49\,400\text{ m}^3$ and, at nominal conditions, contains air at pressure $P_0 = 1\text{ bar}$ and temperature $T_0 = 20\text{ °C}$. Following a LBLOCA (large break loss of coolant accident) the pressure increase in the building is due to

the injection of steam into the building through the breach. The aim is to determine, under certain assumptions, the evolution of pressure and temperature inside the building in the case of steam injection with constant flow and condensation on the walls of the building.

The simulations carried out consider a time interval of 50 seconds, where during the first 20 seconds we have steam injection at a constant mass flow rate, temperature and pressure ($\dot{M}_{\text{in,steam}} = 3500 \text{ kg/s}$, $T_{\text{in,steam}} = 200 \text{ }^\circ\text{C}$, $P_{\text{in,steam}} = 4 \text{ bar}$). At $t = 20 \text{ s}$ the steam injection is stopped and the evolution of pressure and temperature inside the building for the remaining 30 seconds is observed. The wall condensation phenomenon acts during the whole simulation according to the models previously presented. The pressure and temperature evolution are calculated using the *Configuration 1* model, which is described in detail in the next chapter (subsection 3.1.2).

In order to calculate the condensation mass flow rate $\dot{M}_{\text{cd-w}}$ (kg/s), it is assumed a cubic containment building of volume $V = 49400 \text{ m}^3$, such that one can calculate the area of the internal surface of the building S (m^2) (surface on which steam condensation occurs) as follows:

$$S = 6 \cdot V^{2/3} = 8078.0 \text{ m}^2 \quad (2.29)$$

The condensation mass flow rate $\dot{M}_{\text{cd-w}}$ can be calculated using the condensation mass flux $\dot{m}_{\text{v,i}}''$ ($\text{kg/m}^2/\text{s}$) (equation 2.5):

$$\dot{M}_{\text{cd-w}} = \dot{m}_{\text{v,i}}'' \cdot S \quad (2.30)$$

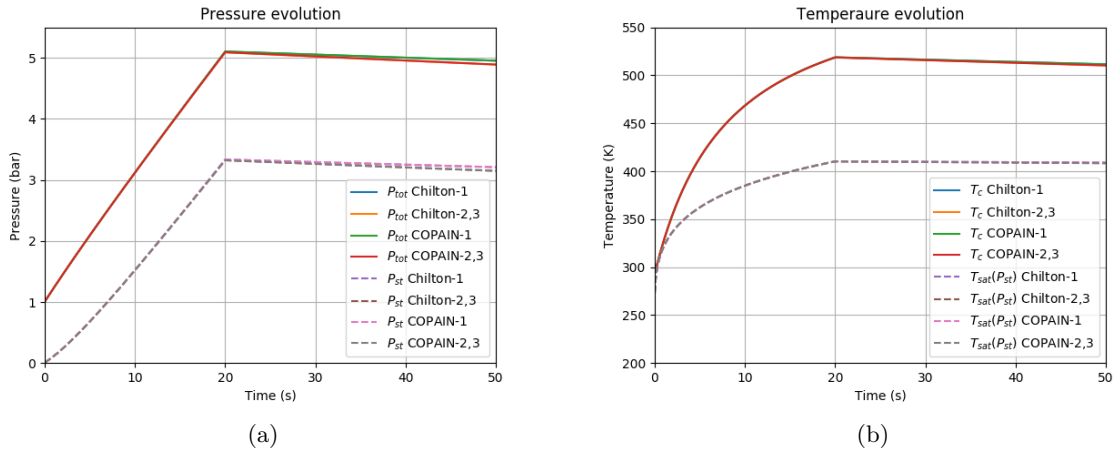


Figure 2.2: (a) Total pressure P_{tot} (bar) evolution and steam partial pressure P_{st} (bar) evolution (dashed lines) in the containment building, where $P_{\text{st}} = P_{\text{tot}} - P_{\text{air}}$ and $P_{\text{air}} = 1 \text{ bar} = \text{const.}$ (b) Gas mixture temperature T_c (K) evolution and saturation temperature at the steam partial pressure $T_{\text{sat}}(P_{\text{st}})$ (K) evolution (dashed lines).

Figure 2.2 shows the time evolution of pressure and temperature inside the containment building. One can clearly see the rapid increase in pressure and temperature in the first 20 seconds during which steam is injected into the building. As anticipated, at $t = 20 \text{ s}$ the steam injection is stopped and it can be seen that both pressure and temperature stop increasing and slowly start decreasing during the remaining 30 seconds due to the wall condensation phenomenon. It should be noted that the wall condensation phenomenon acts during the entire

simulation as it is a passive phenomenon, therefore it also acts during the first 20 seconds. As a consequence, if the wall condensation phenomenon had not been taken into account (*Configuration 0* model, described in detail in the next chapter 3.1.1), during the first 20 seconds we would have observed a slightly faster increase in both pressure and temperature, which would have reached a peak value at $t = 20$ s slightly higher than that shown in figure 2.2, while for the remaining 30 seconds both pressure and temperature would have remained constant and equal to the peak values reached at $t = 20$ s.

Four different wall condensation models are used to obtain the plots in figure 2.2: Chilton-1, Chilton-2,3, COPAIN-1 and COPAIN-2,3. The difference between the models is appreciable when the steam injection is stopped, i.e. for $t > 20$ s: Chilton-1 and COPAIN-1 (blue and green lines are superimposed) provide a slightly slower decrease in pressure and temperature than Chilton-2,3 and COPAIN-2,3 (orange and red lines are superimposed). This last observation suggests that the difference between the models is mainly due to the different formulations used for the mass diffusivity: D_v -1 and D_v -2,3.

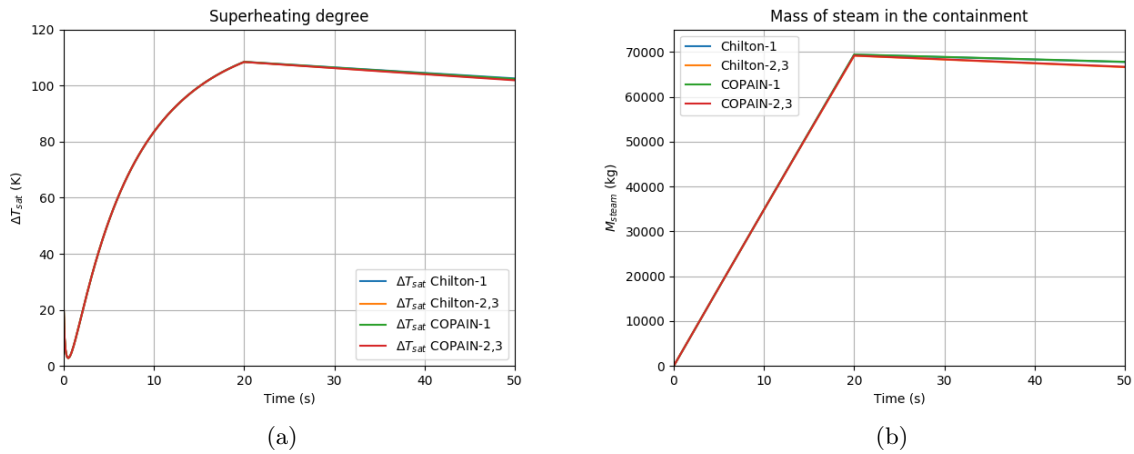


Figure 2.3: (a) Superheating degree $\Delta T_{\text{sat}} = T_c - T_{\text{sat}}(P_{\text{st}})$ (K). (b) Mass of steam in the containment M_{st} (kg).

Figure 2.3 shows the evolution of the superheating degree (directly deducible from plot (b) in figure 2.2) and the evolution of the mass of steam present in the containment building. The same considerations can be made as for the evolution of pressure and temperature: both the superheating degree and the mass of steam in the containment show a rapid increase during the first 20 seconds, reaching a peak at $t = 20$ s and then slightly decreasing for the remaining 30 seconds. It should be noted that the peak value reached by the mass of steam at $t = 20$ s is slightly lower than 70 000 kg, demonstrating that the wall condensation phenomenon also acts during the first 20 seconds: if this phenomenon had not been considered, the mass of steam would have reached exactly 70 000 kg at $t = 20$ s as the flow rate with which it is injected is constant and equal to 3500 kg/s. The amount of steam that condenses as a result of this phenomenon and its mass flow rate are shown in figure 2.4.

The difference between the wall condensation models used is most evident from both figure 2.4 and figure 2.5. Chilton-1 and COPAIN-1 provide a lower condensation mass flow rate than Chilton-2,3 and COPAIN-2,3 and, consequently, there is the same effect on the condensation

heat flux (fig. 2.5). This highlights how influential the use of the two different mass diffusivity formulations actually is and explains why Chilton-2,3 and COPAIN-2,3 are more effective at decreasing the pressure and temperature in the containment building. Concerning the convection heat flux (plot (b) in figure 2.5), not depending on the mass diffusivity, it can be seen that Chilton-1 and Chilton-2,3 give slightly lower values than COPAIN-1 and COPAIN-2,3, but this difference is not appreciable on the evolution of pressure and temperature in the containment building as the convection heat flux is about one order of magnitude lower than the condensation heat flux.

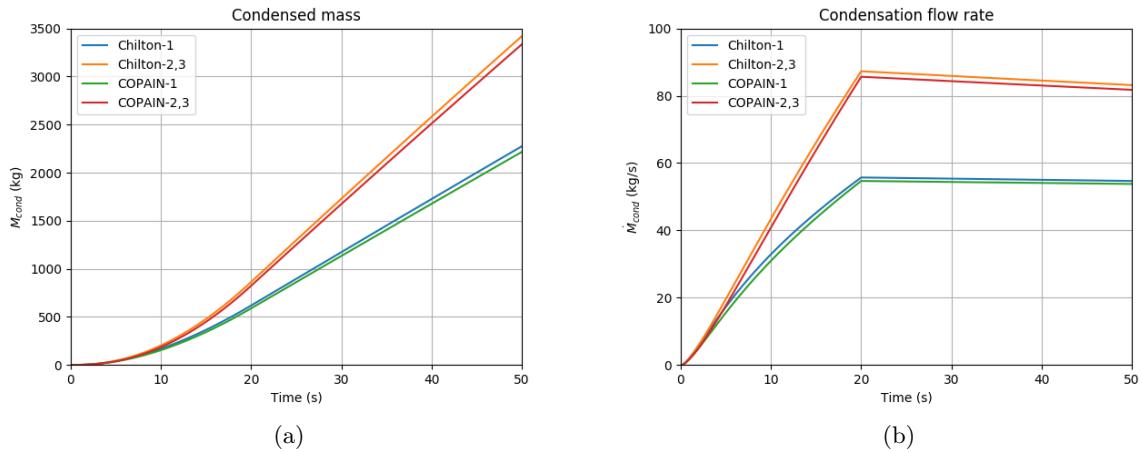


Figure 2.4: (a) Condensed mass M_{cd} (kg). (b) Condensation mass flow rate \dot{M}_{cd-w} (kg/s).

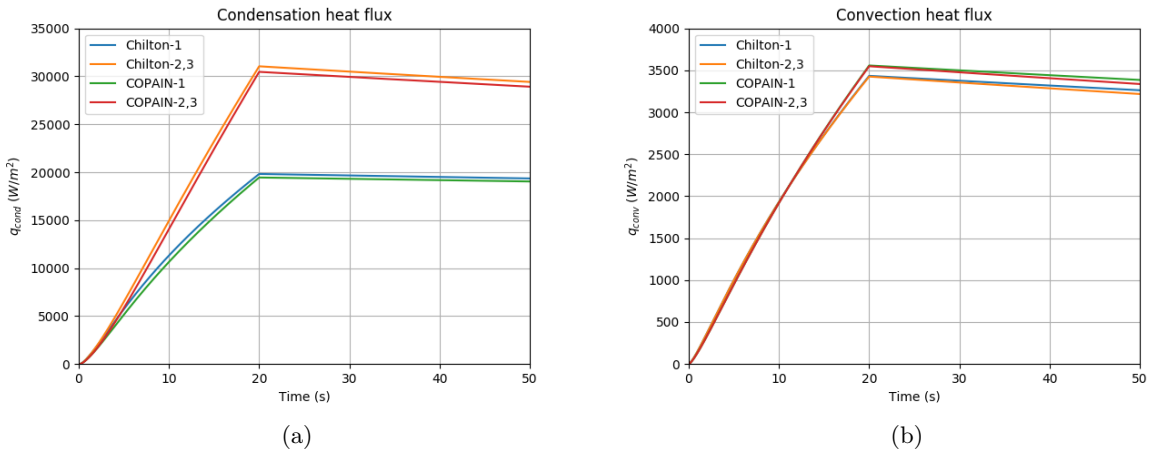


Figure 2.5: (a) Condensation heat flux q_{cd} (W/m^2). (b) Convection heat flux q_{cv} (W/m^2).

Figure 2.6 shows, for the four models, a comparison between the total (integral) amount of latent heat (condensation) exchanged and that of sensible heat (convection). It is clear how much more influential the latent contribution is than the sensible one in all cases. The values shown in the figure are obtained by multiplying the respective heat fluxes (conduction and convection)

by the area of the internal surface of the containment building and then integrating this value over the entire duration of the simulation.

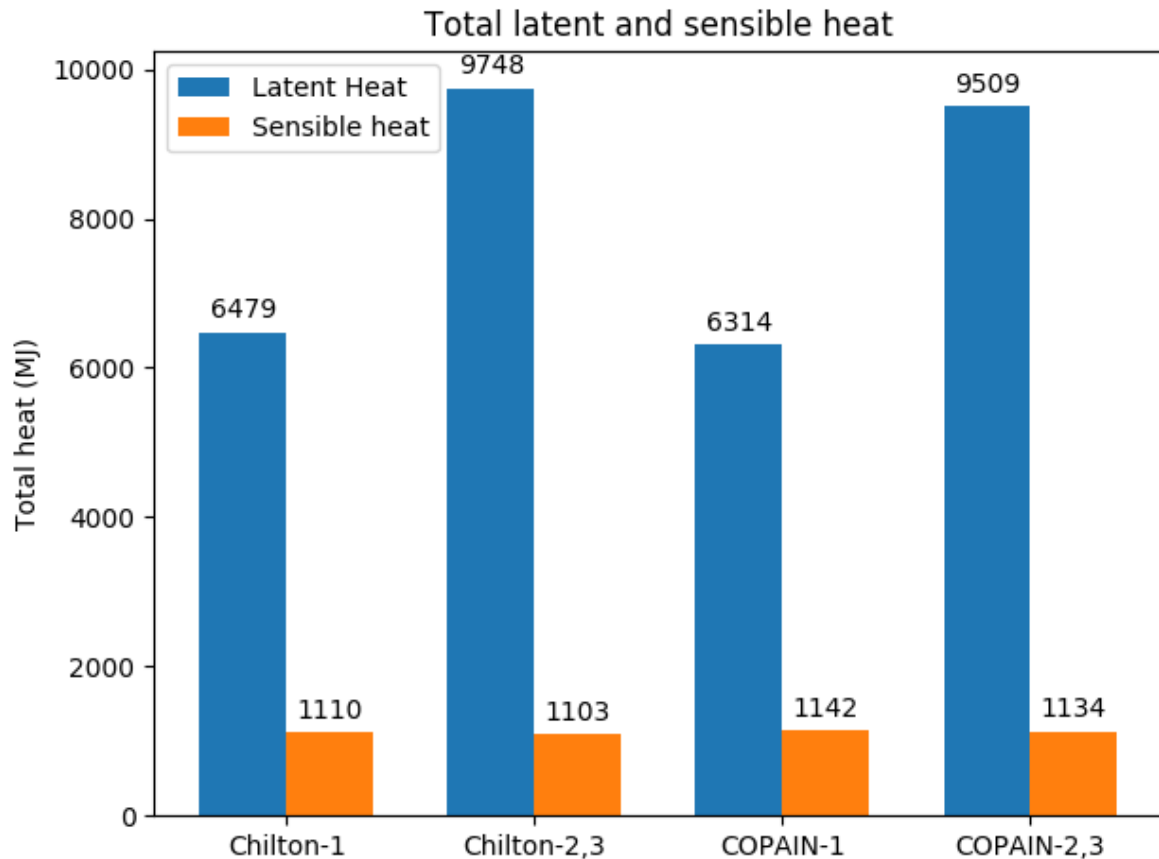


Figure 2.6: Total latent (condensation) and sensible (convection) heat exchanged.

2.5.2 Benteboula-Dabbene: Test-1

Here the case study proposed by the authors in [5], *Test-1: Steam injection in air*, is reproduced. The results obtained are compared with those proposed in the article in order to provide a validation of the wall condensation model (remember that this model was mainly extrapolated from the same article).

The case study considers a cylindrical enclosure inside which there is initially air under homogeneous conditions and the following thermodynamic conditions: $p_0 = 1.2$ bar and $T_0 = 45$ °C. The volume of the enclosure is $V = 20$ m³ and it is filled with a mass of air $M_{\text{air}} = 28.41$ kg. The condensation phenomenon occurs on the inside wall of the enclosure which has a surface area $S = 42.026$ m² and is at a constant temperature $T_w = 45$ °C. It is assumed that superheated steam is injected into the enclosure with a constant mass flow rate $\dot{M}_{\text{st}} = 200$ g/s and temperature $T_{\text{st}} = 200$ °C for a time interval of 1000 seconds. The calculations are carried out for a duration of 2000 seconds. These time intervals are chosen in order to observe the steady states during and after the steam injection. The first steady state is reached when the injected mass and energy are balanced by the heat and mass transfer to the wall and by bulk condensation.

After the end of injection, the gas temperature decreases to reach the wall temperature with a final pressure corresponding to saturation conditions. [5]

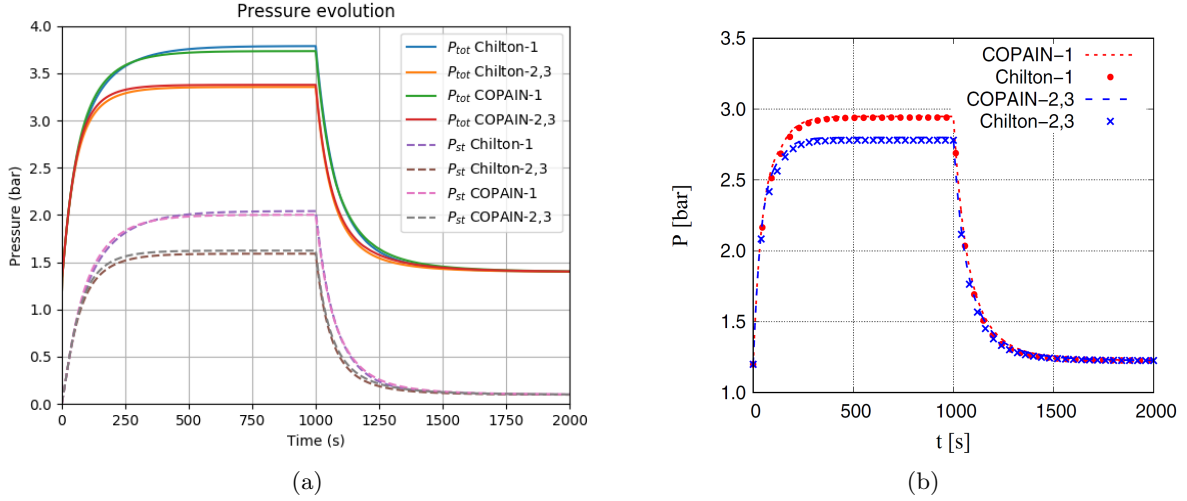


Figure 2.7: (a) Total pressure P_{tot} (bar) evolution and steam partial pressure P_{st} (bar) evolution (dashed lines) in the containment building, where $P_{st} = P_{tot} - P_{air}$ and $P_{air} = p_0 = 1.2 \text{ bar} = \text{const.}$ (b) Total pressure P (bar) evolution provided in [5].

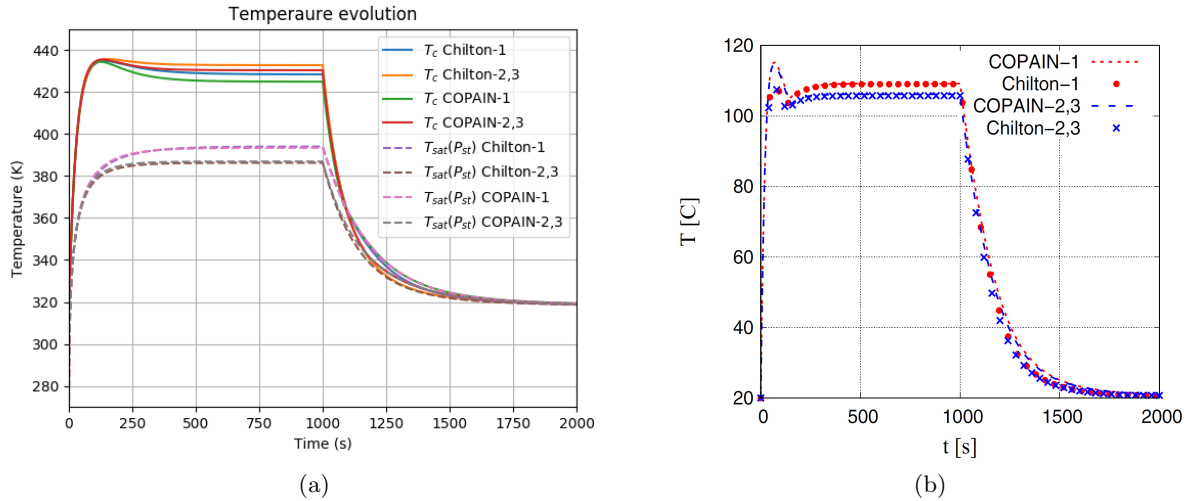


Figure 2.8: (a) Gas mixture temperature T_c (K) evolution and saturation temperature at the steam partial pressure $T_{sat}(P_{st})$ (K) evolution (dashed lines). (b) Gas mixture temperature T (°C) evolution provided in [5].

Figures 2.7 and 2.8 show respectively the pressure and temperature temporal evolution along the whole simulation, comparing the results obtained through the Python codes (subplots (a)) with those proposed in [5] (subplots (b)). The comparison shows that the Python codes give very similar results to those proposed in the article, the differences being due to the different type of containment model used: the *Configuration 1* model presented in the next chapter

(subsection 3.1.2) is implemented in the Python codes, that is a 0D containment model based on the numerical solution of the mass and energy conservation equations, while in [5] they used a lumped parameter approach implemented in the CAST3M-LP containment code. Regarding the temporal evolution of the pressure, it can be noted that both results show the same behaviour with respect to the different formulations used for the wall condensation model: Chilton-1 and COPAIN-1 lead to higher pressures at the first steady-state ($500 < t < 1000$ s) than Chilton-2,3 and COPAIN-2,3, while at the second steady-state ($1500 < t < 2000$ s) the pressure reaches almost the same value for all the correlations. This underlines the importance of the influence of the two formulation used to calculate the effective diffusion coefficient: D_v -1 and D_v -2,3 (their temporal evolution is shown in figure 2.9).

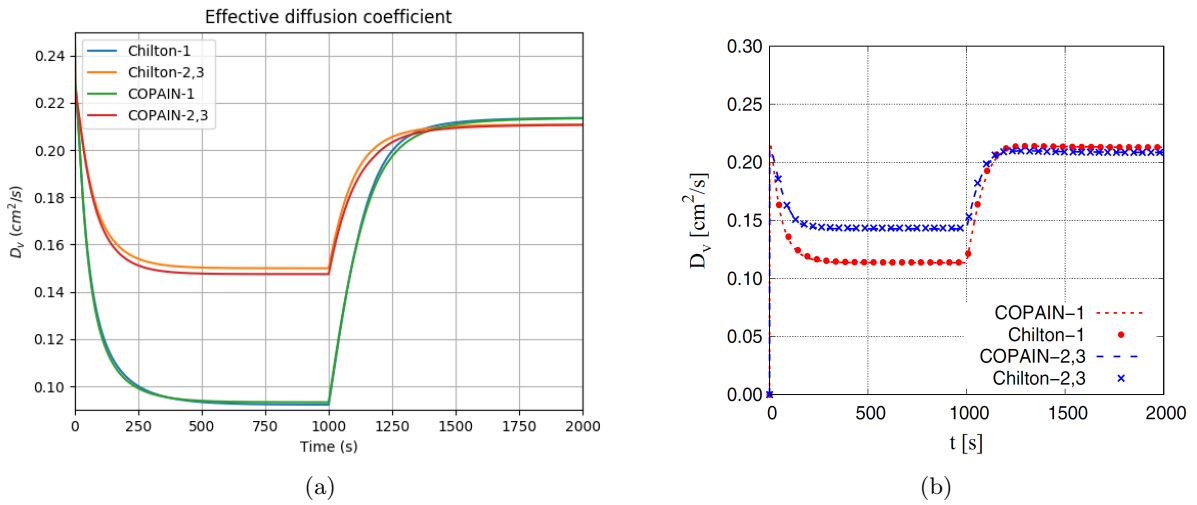


Figure 2.9: Comparison between the effective diffusion coefficient D_v (cm^2/s) evolution calculated with the *Configuration 1* model (a) and the one provided in [5] (b).

Figure 2.10 shows the time evolution of the mass of steam in the building: similarly to the Delhaye problem 11.2 (see subsection 2.5.1), the amount of steam in the building is controlled by the steam mass flow rate that is injected in it, which during the first 1000 seconds causes it to increase, and by the condensation phenomenon, which acts throughout the simulation, causing the amount of steam to decrease. Comparing the results obtained through the *Configuration 1* model with those provided in [5], it can be seen that in the latter the amount of steam reached inside the building is lower than that calculated using the Python codes, suggesting a greater effectiveness of the condensation phenomenon for the model in [5] compared to the *Configuration 1* model: a lower mass of steam means a greater amount of steam that is condensed and consequently this effect spills over onto the temporal evolution of pressure and temperature in the building (comparisons in figures 2.7 and 2.8 show that in the *Configuration 1* model both pressure and temperature reach higher values than in [5]). The difference between the two models, as already mentioned, can mainly be explained by the use of two different Containment codes.

As already mentioned, the condensation phenomenon can be divided into two contributions: latent (condensation) and sensible (convection). Figures 2.11 and 2.12 show the temporal evolution of the condensation and convection fluxes, respectively, comparing the results obtained with our model with those in [5]: regarding the latent contribution it can be noticed that the

two results are very similar, with slightly higher values obtained by our model, while regarding the sensible contribution the opposite situation occurs, with the results of [5] showing slightly higher values than those of the *Configuration 1* model.

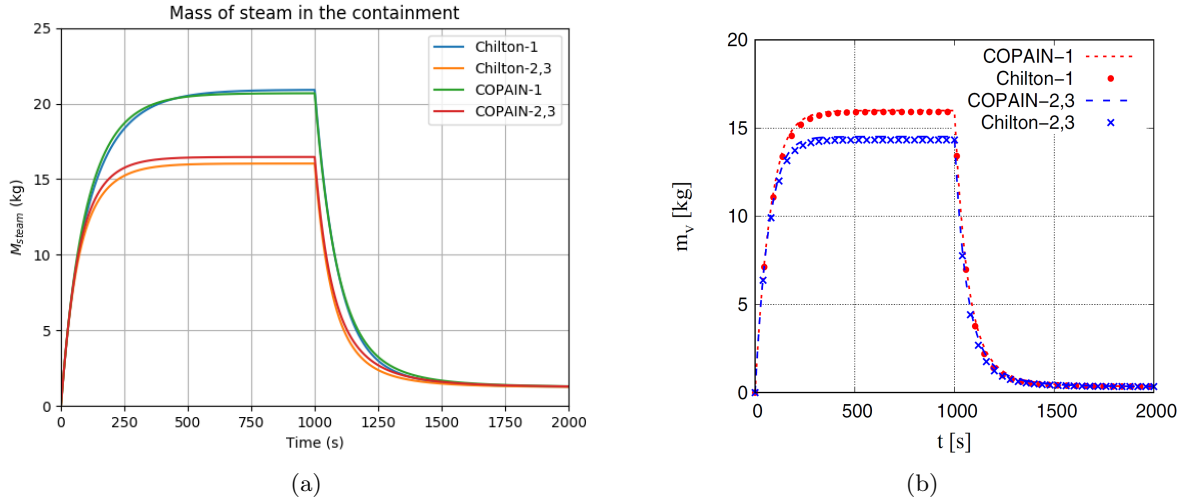


Figure 2.10: Comparison between the mass of steam M_{st} (kg) evolution calculated with the *Configuration 1* model (a) and the one provided in [5] (b).

Figure 2.13 shows, for the four wall condensation formulations, a comparison between the total (integral) amount of latent heat (condensation) exchanged and that of sensible heat (convection). It is clear how much more influential the latent contribution is than the sensible one in all cases. The values shown in the figure are obtained by multiplying the respective heat fluxes (conduction and convection) by the area of the internal surface of the containment building and then integrating this value over the entire duration of the simulation.

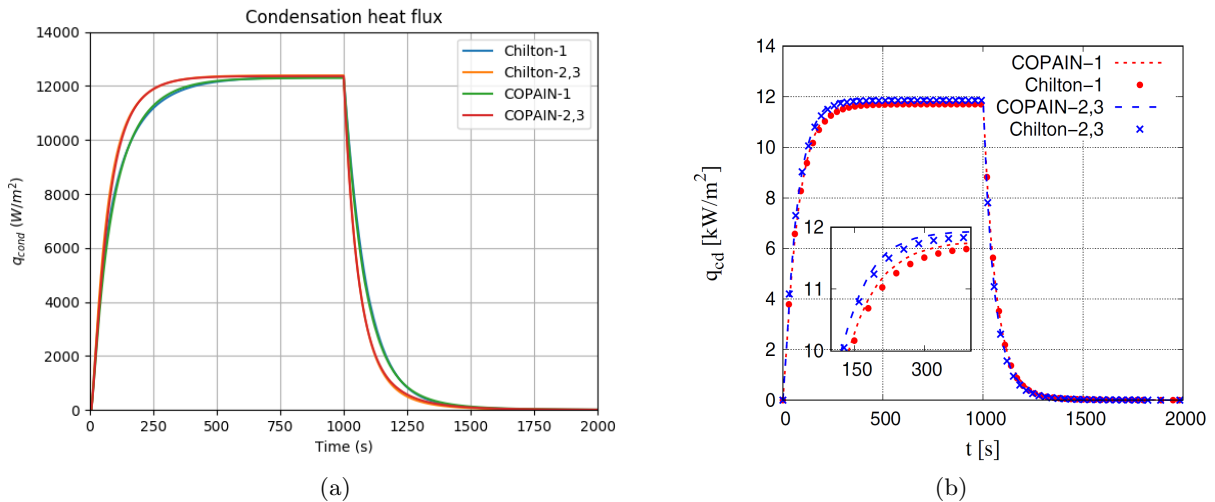


Figure 2.11: Comparison between the condensation heat flux q_{cd} (W/m²) evolution calculated with the *Configuration 1* model (a) and the one provided in [5] (b).

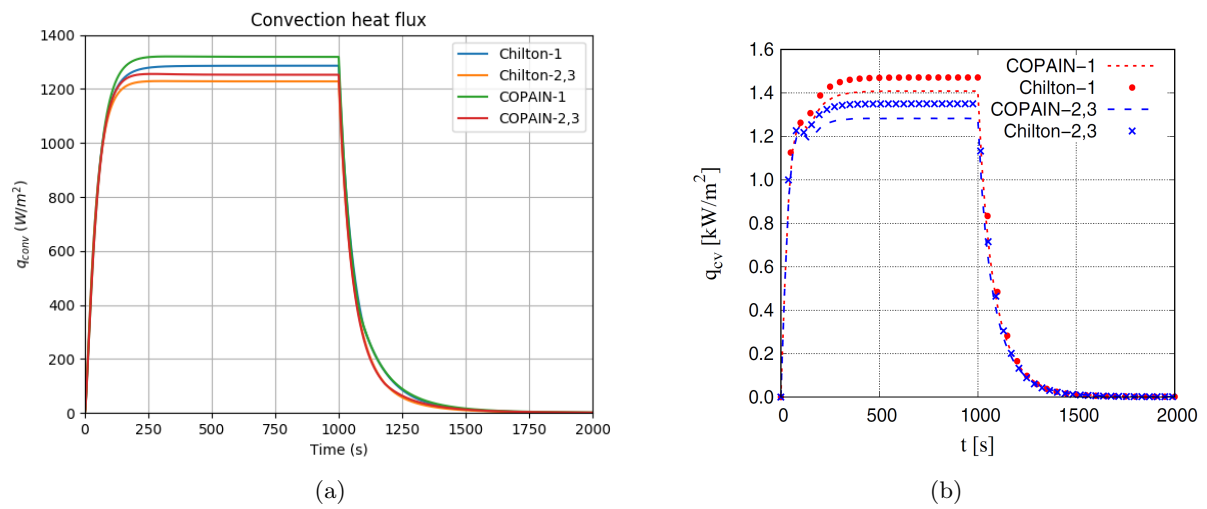


Figure 2.12: Comparison between the convection heat flux q_{cv} (W/m²) evolution calculated with the *Configuration 1* model (a) and the one provided in [5] (b).

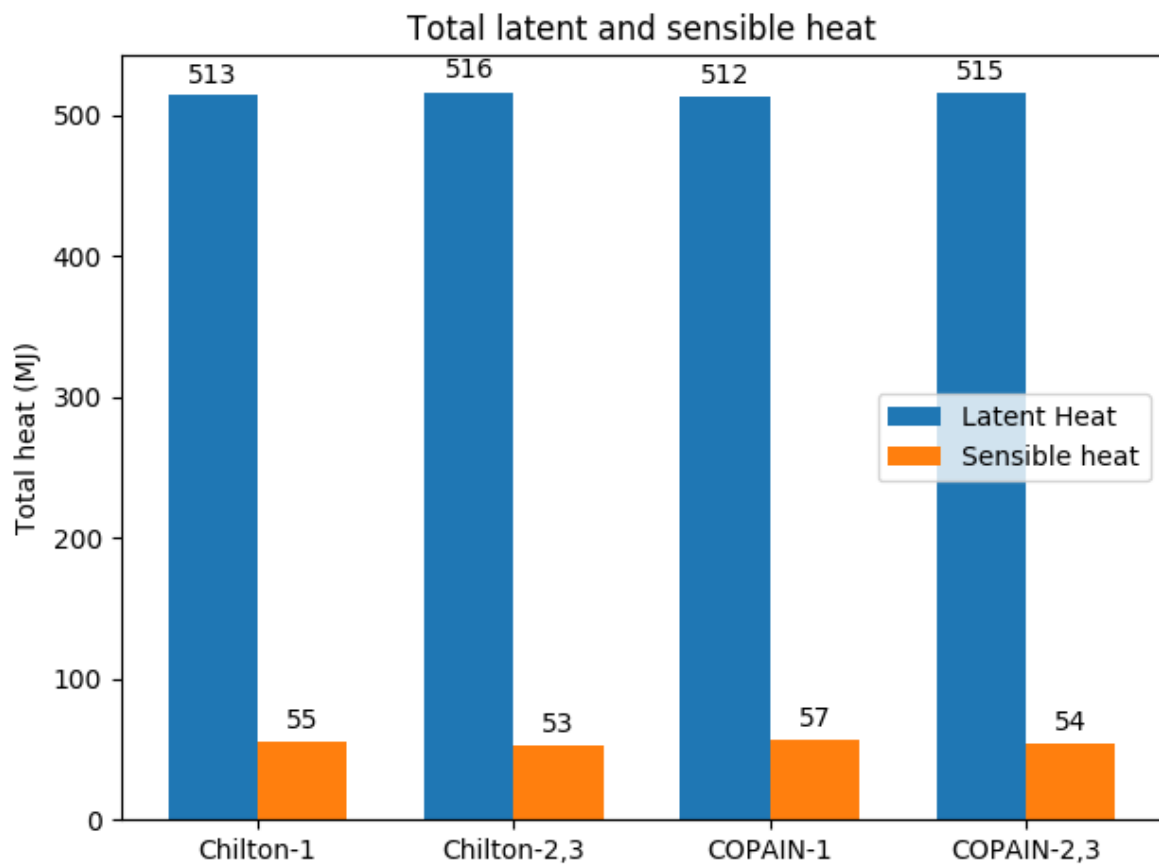


Figure 2.13: Total latent (condensation) and sensible (convection) heat exchanged.

2.6 Condensation ratio maps

In this section it is proposed to build parametric maps of the condensation ratio for the Wall condensation model, similarly to the spray repartition maps (see section 1.6).

2.6.1 Definition of condensation ratio

The *condensation ratio* x_{cond} can be defined as the ratio between the condensation heat flux q_{cd} (latent contribution) and the total heat flux $q_{\text{w}} = q_{\text{cd}} + q_{\text{cv}}$ (condensation + convection, or latent + sensible contributions) exchanged between the wall and the gas mixture.

$$x_{\text{cond}} = \frac{q_{\text{cd}}}{q_{\text{cd}} + q_{\text{cv}}} \quad (2.31)$$

Since both q_{cd} and q_{cv} are always greater than 0, you will always have that $0 < x_{\text{cond}} < 1$. In the extreme cases $x_{\text{cond}} = 0$ or $x_{\text{cond}} = 1$, you will have respectively that $q_{\text{cd}} = 0$ or $q_{\text{cv}} = 0$.

2.6.2 Input parameters and case study

As already mentioned, the purpose of this section is to construct parametric maps for x_{cond} , a kind of look-up tables that can be used by any user to determine, even by interpolation, the value of x_{cond} for a given combination of parameters.

In this case, the maps are constructed by creating possible combinations between three parameters on which x_{cond} depends: total pressure of the gas mixture P , air partial pressure P_{air} and superheating degree ΔT_{sat} .

$$x_{\text{cond}} \text{ MAPS} \rightarrow x_{\text{cond}}(P, P_{\text{air}}, \Delta T_{\text{sat}}) \quad (2.32)$$

These parameters are those that determine the atmospheric conditions, one could increase the number of parameters by including a parametrization also on the wall temperature (e.g. $x_{\text{cond}}(P, P_{\text{air}}, \Delta T_{\text{sat}}, T_{\text{w}})$), but, for simplicity, it has been chosen to consider fixed conditions for the wall temperature: $T_{\text{w}} = 45^\circ\text{C} = \text{const}$.

Table 2.1

	Input parameters
Atmosphere	$P = 0.8 \div 6 \text{ bar}$ with $\Delta P = 0.4 \text{ bar}$ $P_{\text{air}} = (0.8 - P_{\text{st,min}}) \div (6 - P_{\text{st,min}}) \text{ bar}$ with $\Delta P_{\text{air}} = 0.4 \text{ bar}$ $\Delta T_{\text{sat}} = 0 \div 200^\circ\text{C}$ with $\Delta(\Delta T_{\text{sat}}) = 20^\circ\text{C}$
Wall	$T_{\text{w}} = 45^\circ\text{C} = \text{const}$

Remind that Dalton's law is always valid, so, for each combination of total pressure P and partial pressure of air P_{air} , the partial pressure of the steam P_{steam} is automatically determined through the relation $P = P_{\text{air}} + P_{\text{steam}}$. Obviously, to be physically consistent, all combinations between P and P_{air} are created respecting the condition $P > P_{\text{air}}$. Furthermore, in order to carry out the one-way calculations correctly, it is necessary that, whatever the combination of parameters, the temperature of the gas mixture in the atmosphere of the building is at a higher temperature than that of the wall T_{w} . In order to meet this latter condition, a minimum

allowable value for the steam partial pressure is introduced, $P_{st,min} = P_{sat}(T_i = T_w)$, acting on the range of variation of the air partial pressure P_{air} .

The figures below (2.14, 2.15, 2.16, 2.17) show an extrapolation (conditions: $P = 1.2 \div 6$ bar, $P_{air} = 1$ bar, $\Delta T_{sat} = 0 \div 100$ °C) of the x_{cond} maps (subfigures (a)), in the form of 2D maps, in which x_{cond} is represented simultaneously as a function of the steam mass fraction ($X_{steam} = P_{steam}/P$, with $P = P_{steam} + P_{air}$) and the superheating degree (ΔT_{sat}). The four figures correspond to the use of the four correlations respectively: Chilton-1, Chilton-2,3, COPAIN-1, COPAIN-2,3. A green line corresponding to $x_{cond} = 92\%$ is represented in each x_{cond} map for a quick comparison with the 92/8 historical assumption (see subsection 2.3.2).

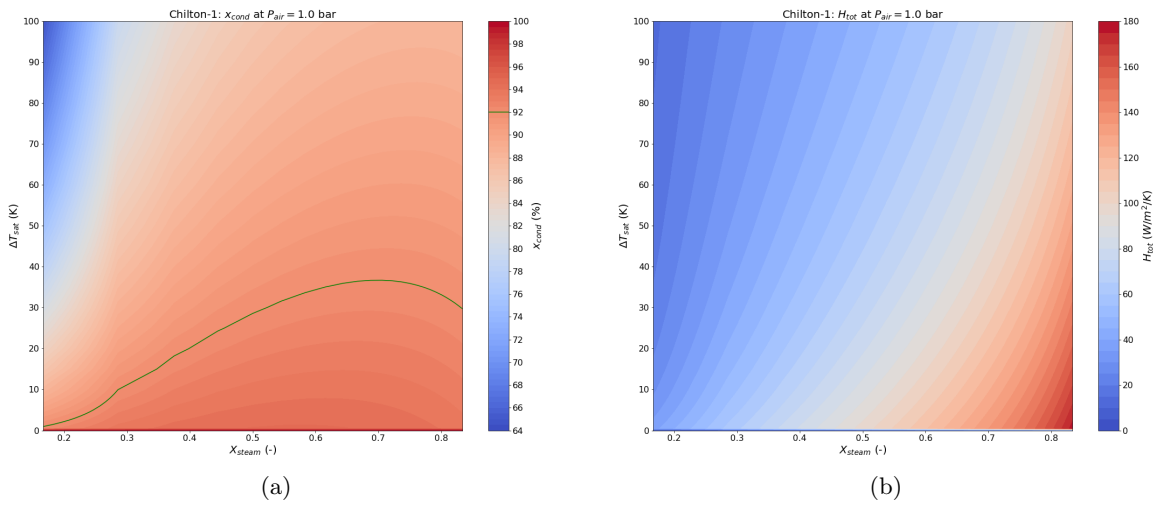


Figure 2.14: (a) Condensation ratio $x_{cond}(X_{steam}, \Delta T_{sat})$ (%) and (b) Total heat transfer coefficient $H_{tot}(X_{steam}, \Delta T_{sat})$ ($W/m^2/K$) 2D maps. Chilton correlation, D_v -1 formulation.

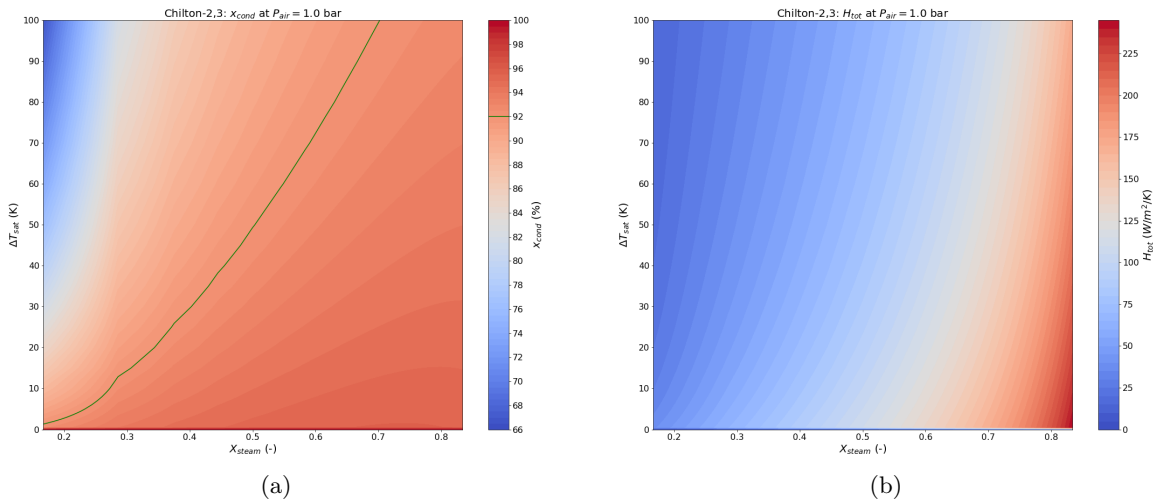


Figure 2.15: (a) Condensation ratio $x_{cond}(X_{steam}, \Delta T_{sat})$ (%) and (b) Total heat transfer coefficient $H_{tot}(X_{steam}, \Delta T_{sat})$ ($W/m^2/K$) 2D maps. Chilton correlation, D_v -2,3 formulation.

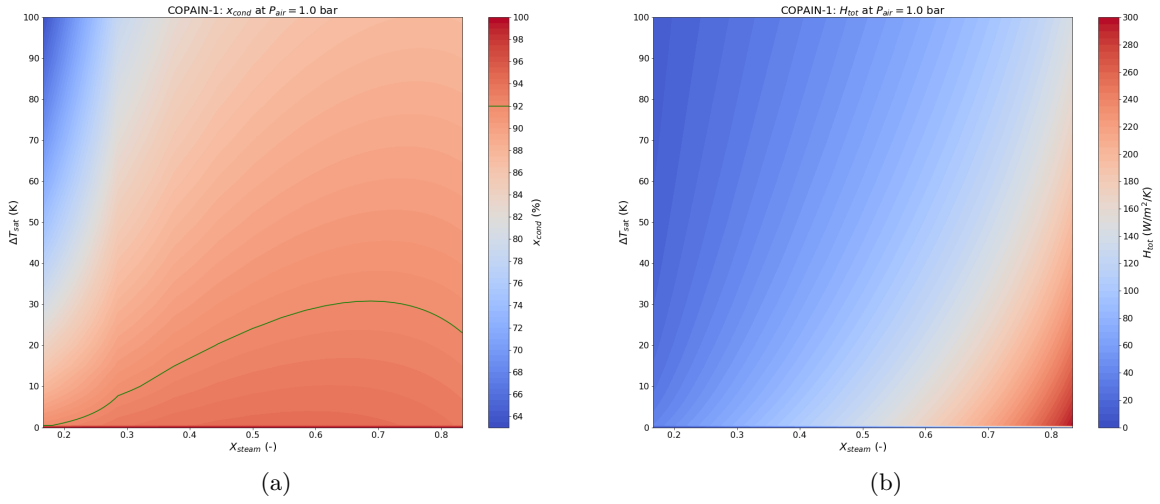


Figure 2.16: (a) Condensation ratio $x_{\text{cond}}(X_{\text{steam}}, \Delta T_{\text{sat}})$ (%) and (b) Total heat transfer coefficient $H_{\text{tot}}(X_{\text{steam}}, \Delta T_{\text{sat}})$ ($\text{W/m}^2/\text{K}$) 2D maps. COPAIN correlation, D_v-1 formulation.

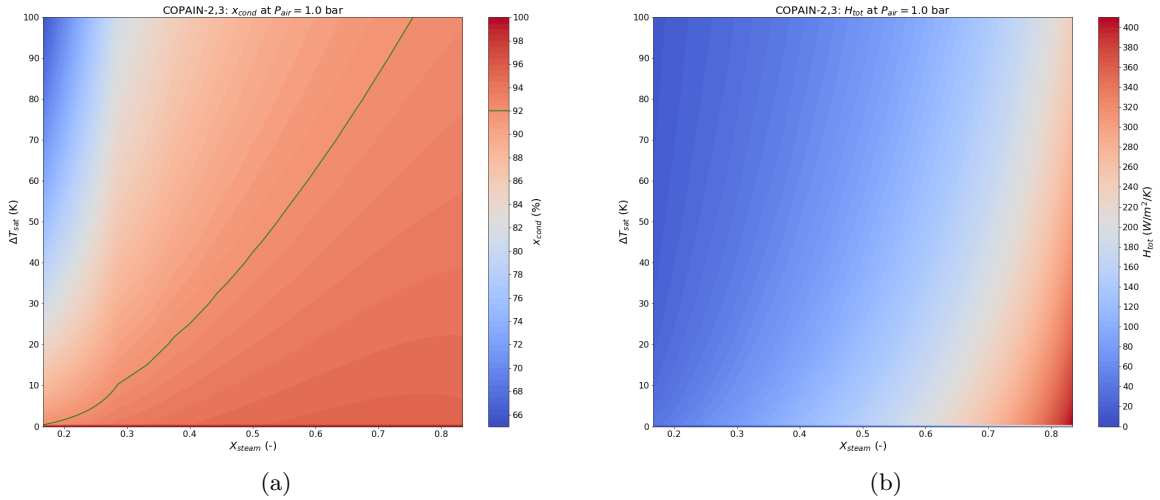


Figure 2.17: (a) Condensation ratio $x_{\text{cond}}(X_{\text{steam}}, \Delta T_{\text{sat}})$ (%) and (b) Total heat transfer coefficient $H_{\text{tot}}(X_{\text{steam}}, \Delta T_{\text{sat}})$ ($\text{W/m}^2/\text{K}$) 2D maps. COPAIN correlation, $D_v-2,3$ formulation.

From the above graphs it can be deduced that, fixing the amount of steam in the building (fixing X_{steam}), the condensation ratio decreases as the superheating degree increases, in all four cases. If, on the other hand, you fix the superheating degree, you can observe a different behaviour according to the different formulation of the effective diffusion coefficient (D_v-1 in figures 2.14 and 2.16, $D_v-2,3$ in figures 2.15 and 2.17): using D_v-1 the condensation ratio increases with X_{steam} until it reaches a maximum for $X_{\text{steam}} = 0.6 \div 0.8$ and then decreases for higher values of X_{steam} , while using $D_v-2,3$ the condensation ratio increases with X_{steam} without decreasing again, except for low values of the superheating degree ($\Delta T_{\text{sat}} < 20 \div 30$ K) for $X_{\text{steam}} > 0.8$. A similar 2D map for the total heat transfer coefficient H_{tot} (subfigures (b)) is shown next to each

x_{cond} map: in all four cases, it can be observed that H_{tot} decreases as ΔT_{sat} increases, while it increases as X_{steam} increases. The highest values of H_{tot} are achieved using the COPAIN-2,3 correlation (fig. 2.17, with $H_{\text{tot,max}} \approx 400 \text{ W/m}^2/\text{K}$), while the lowest values are achieved using the Chilton-1 correlation (fig. 2.14, with $H_{\text{tot,max}} \approx 180 \text{ W/m}^2/\text{K}$).

Concerning the historical models (Tagami and Uchida), two 2D maps (fig. 2.18) for only the total heat transfer coefficient H_{tot} calculated by Tagami and Uchida correlations (see equations 2.17 and 2.18) are shown, since there would be no reason to represent condensation ratio maps for this kind of models (see subsection 2.3.2) which consider a fixed value $x_{\text{cond}} = 92\%$ if you are considering a superheated atmosphere ($\Delta T_{\text{sat}} > 0 \text{ K}$) or $x_{\text{cond}} = 100\%$ if the atmosphere is in saturation conditions ($\Delta T_{\text{sat}} = 0 \text{ K}$). It can be observed that, for both correlations, H_{tot} does not depend on ΔT_{sat} (H_{tot} is constant fixing X_{steam}), while it increases as X_{steam} increases.

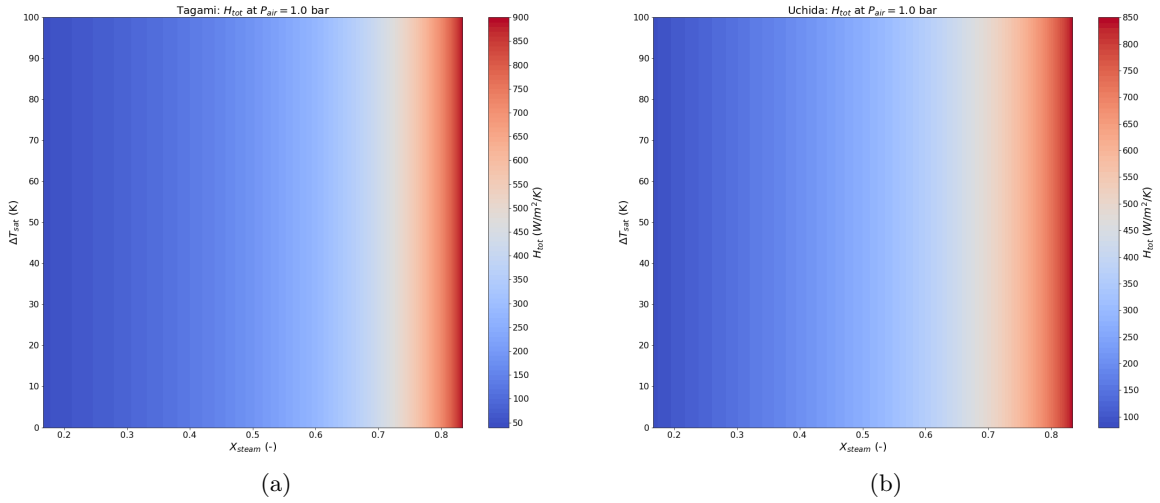


Figure 2.18: Total heat transfer coefficient $H_{\text{tot}}(X_{\text{steam}}, \Delta T_{\text{sat}})$ (W/m²/K) 2D maps, with $X_{\text{steam}} = P_{\text{steam}}/P$ and $P = P_{\text{steam}} + P_{\text{air}}$. Conditions: $P = 1.2 \div 6 \text{ bar}$, $P_{\text{air}} = 1 \text{ bar}$, $\Delta T_{\text{sat}} = 0 \div 100 \text{ }^\circ\text{C}$, (a) Tagami correlation, (b) Uchida correlation.

Chapter 3

Containment H&M transfers model

Contents

3.1 OD containment model for a LOCA with spray system and wall condensation	83
3.1.1 Configuration 0: no spray, no wall condensation	84
3.1.2 Configuration 1: no spray, with wall condensation	88
3.1.3 Configuration 2: with spray, with wall condensation	90
3.2 Comparison with literature	93
3.2.1 Delhay problem	93
3.2.2 Benteboula-Dabbene: Test-1	94
3.3 Main case study: MSLB simulation with spray activation and wall condensation	96
3.3.1 Mechanistic models for spray and wall condensation	98
3.3.2 Historical (conservative) models for spray and wall condensation using the 92/8 repartition	102
3.3.3 Historical models for spray and wall condensation using the MAPS	106

3.1 OD containment model for a LOCA with spray system and wall condensation

A containment with fixed volume V is considered. Initially the containment is filled with air, at pressure P_{air}^0 and temperature T^0 . In the context of an accidental scenario, it is assumed a large breach appears on the main pipe in which water vapor (steam) circulates. Hence steam is injected into the containment with a known mass flowrate \dot{M}_{br} . In the scenario under study, it is also assumed a spray system (CSS) is turned on after the breach appears (when a certain threshold pressure is reached in the containment). Water is sprayed inside the containment and interacts with the air/steam mixture. Note also the air/steam mixture interacts with the containment walls.

The objective is to develop a simple 0D model to describe the time evolution of the containment pressure P and temperature T , taking into account:

- steam injection through the breach
- water droplet injection through the spray system
- interaction with the containment walls.

Air is described as a perfect gas, such that $P_{\text{air}} = \rho_{\text{air}} r_{\text{air}} T$ with T the temperature assumed uniform in the containment and the same for air and steam. The unknown fields are the pressure field for air, P_{air} , the pressure field for steam P_{steam} and the temperature field T . The containment pressure is $P = P_{\text{air}} + P_{\text{steam}}$ and the containment temperature is T . Note that air and steam density are also variables used in the analysis, for instance when expressing next mass conservation. Denote ρ_{air} and ρ_{steam} respectively the air and steam density. Note ρ_{air} is easily computed from P_{air} and T using the Perfect Gas (PG) Equation of State (EoS). For steam the IAPWS formulation is used, which allows in particular to compute the specific enthalpy h_{steam} from P_{steam} and T .

3.1.1 Configuration 0: no spray, no wall condensation

In order to describe the evolution of $P(t)$ and $T(t)$, one must express mass and energy conservation for the fluid enclosed in the containment. The control volume is the containment itself, with a single inflow condition for this baseline configuration: steam inflow through the breach.

3.1.1.1 Mass conservation

Expressing mass conservation on the control volume V yields:

$$\frac{d}{dt} \int_V \rho dV = - \int_S \rho \vec{U} \cdot \vec{n} dS \quad (3.1)$$

There are actually two species present in V : air and steam. Denote \dot{M}_{br} the steam mass flow rate through the breach (steam injection inside the containment). It will be also convenient to introduce the total mass of air and steam in the containment, respectively: $M_{\text{air}}(t)$, $M_{\text{steam}}(t)$. The total mass of fluid, $M = M_{\text{air}} + M_{\text{steam}}$ increases because of steam injection through the breach. Using the various notations introduced, the mass conservation principle (eq. 3.1) can also be expressed as:

$$\frac{d(M_{\text{air}} + M_{\text{steam}})}{dt} = \dot{M}_{\text{br}} \quad (3.2)$$

The mass conservation principle can be obviously decomposed for air and steam:

$$\begin{cases} \frac{dM_{\text{air}}}{dt} = 0 \\ \frac{dM_{\text{steam}}}{dt} = \dot{M}_{\text{br}} \end{cases} \quad (3.3)$$

In order to express the air and steam mass inside the control volume, the density of air and steam are introduced. The constant volume V of the containment is filled with a gaseous mixture of steam and air. Starting with mass conservation for air, one can write:

$$\frac{d\rho_{\text{air}}(t)V}{dt} = 0 \quad (3.4)$$

so that ρ_{air} is constant equal to its initial value:

$$\rho_{\text{air}} = \rho_{\text{air}}^0 = \frac{P_{\text{air}}^0}{r_{\text{air}}T^0} \quad (3.5)$$

For steam:

$$\frac{dM_{\text{steam}}}{dt} = \dot{M}_{\text{br}} \quad (3.6)$$

The detailed form of \dot{M}_{br} depends on the steam injection scenario. For instance, steam can be injected from $t = 0$ to $t = t_1$ and the evolution can be followed until a final time t_2 with no steam injected in the containment from t_1 to t_2 . In that case, the form of \dot{M}_{br} is:

$$\dot{M}_{\text{br}}(t) = \begin{cases} \dot{M}_{\text{br},1} & \text{if } t \leq t_1 \\ 0 & \text{if } t \in]t_1, t_2] \end{cases} \quad (3.7)$$

Assuming the containment is initially filled with air only, an immediate integration of eq. 3.6 with this initial condition yields:

$$M_{\text{steam}}(t) = \begin{cases} \dot{M}_{\text{br},1}t & \text{if } t \leq t_1 \\ \dot{M}_{\text{br},1}t_1 & \text{if } t \in]t_1, t_2] \end{cases} \quad (3.8)$$

The evolution of the steam density $\rho_{\text{steam}}(t)$ is obtained from:

$$M_{\text{steam}}(t) = \rho_{\text{steam}}(t)V \quad (3.9)$$

so that:

$$\rho_{\text{steam}}(t) = \begin{cases} \frac{\dot{M}_{\text{br},1}t}{V} & \text{if } t \leq t_1 \\ \frac{\dot{M}_{\text{br},1}t_1}{V} & \text{if } t \in]t_1, t_2] \end{cases} \quad (3.10)$$

3.1.1.2 Mass and molar fractions

From the constant value M_{air} and $M_{\text{steam}}(t) = \dot{M}_{\text{br}}t$, the mass fractions $Y_{\text{air}}(t)$ and $Y_{\text{steam}}(t)$ can be computed:

$$Y_{\text{air}} = \frac{M_{\text{air}}}{M(t)} = \frac{M_{\text{air}}}{M_{\text{air}} + \dot{M}_{\text{br}}t} \quad (3.11)$$

or else, introducing the densities:

$$Y_{\text{air}}(t) = \frac{\rho_{\text{air}}}{\rho_{\text{air}} + \rho_{\text{steam}}(t)} \quad (3.12)$$

$$Y_{\text{steam}}(t) = \frac{\rho_{\text{steam}}(t)}{\rho_{\text{air}} + \rho_{\text{steam}}(t)} \quad (3.13)$$

Alternatively, using the molar fractions (and denoting respectively MW_{air} , MW_{steam} the molar mass of air and steam) yields:

$$X_{\text{air}} = \frac{Y_{\text{air}}MW_{\text{steam}}}{Y_{\text{air}}MW_{\text{steam}} + Y_{\text{steam}}MW_{\text{air}}} \quad (3.14)$$

or else, using densities:

$$X_{\text{air}}(t) = \frac{\rho_{\text{air}} MW_{\text{steam}}}{\rho_{\text{air}} MW_{\text{steam}} + \rho_{\text{steam}}(t) MW_{\text{air}}} \quad (3.15)$$

and $X_{\text{steam}}(t) = 1 - X_{\text{air}}(t)$.

3.1.1.3 Pressure in the containment

The total pressure $P(t)$ in the containment is such that:

$$P(t) = P_{\text{air}}(t) + P_{\text{steam}}(t) \quad (3.16)$$

Air is described as a perfect gas so that it is directly connected with the containment temperature:

$$P_{\text{air}}(t) = \rho_{\text{air}} r_{\text{air}} T(t) \quad (3.17)$$

with $r_{\text{air}} = R/MW_{\text{air}}$. R is the perfect gas constant ($R = 8.314 \text{ J/mol/K}$) and MW_{air} denotes the molar mass of air.

The steam partial pressure $P_{\text{steam}}(t)$ is such that:

$$P_{\text{steam}}(t) = X_{\text{steam}}(t)P(t) \quad (3.18)$$

It remains to compute the temperature $T(t)$ and this is of course achieved by using an energy balance.

3.1.1.4 Energy conservation

The global form of energy conservation applied to the containment as a control volume reads:

$$\frac{d}{dt} \int_V \rho E dV = \dot{W} + \dot{Q} - \int_S \rho E \vec{U} \cdot \vec{n} dS \quad (3.19)$$

and can be readily simplified by assuming no thermal losses through the boundary S (hence $\dot{Q} = 0$) and considering \dot{W} is the power of pressure force only (body forces and viscous forces are neglected):

$$\dot{W} = - \int_S P \vec{U} \cdot \vec{n} dS \quad (3.20)$$

It follows that eq. 3.19 can be simplified as:

$$\frac{d}{dt} \int_V \rho E dV = - \int_S \rho H \vec{U} \cdot \vec{n} dS \quad (3.21)$$

where the specific total enthalpy $H = E + P/\rho$ has been introduced. In the present 0D analysis it is assumed the kinetic energy contribution to the total energy or to the total enthalpy is negligible with respect to the internal energy or enthalpy. In other words $E \approx e$ and $H \approx h$ with of course $h = e + P/\rho$. Therefore, eq. 3.21 can also be recast in the form:

$$\frac{d}{dt} \int_V \rho h dV - \frac{d}{dt} \int_V P dV = - \int_S \rho h \vec{U} \cdot \vec{n} dS \quad (3.22)$$

The net contribution to the variation of the total energy in the containment is provided by the breach (steam) injection. Assuming known thermodynamic conditions at the breach, it is then possible to compute the specific enthalpy h_{br} at the breach and the corresponding enthalpy flux $\dot{M}_{\text{br}} \times h_{\text{br}}$. Note that in the present analysis \dot{M}_{br} and h_{br} will be prescribed quantities. It follows eq. 3.22 can be expressed as:

$$\frac{d}{dt} \int_V \rho h dV - \frac{dP(t)}{dt} V = \dot{M}_{\text{br}} h_{\text{br}} \quad (3.23)$$

or else:

$$\frac{d(\rho_{\text{steam}} h_{\text{steam}})}{dt} + \frac{d(\rho_{\text{air}} h_{\text{air}})}{dt} - \frac{dP}{dt} = \frac{\dot{M}_{\text{br}} h_{\text{br}}}{V} \quad (3.24)$$

In this expression, the specific enthalpy h_{br} of the steam injected through the breach between $t = t_1$ and $t = t_2$ takes a prescribed value. Since $h_{\text{air}} = C_{p,\text{air}} T + \text{constant}$ and $P = P_{\text{steam}} + P_{\text{air}}$ with $P_{\text{air}} = \rho_{\text{air}} r_{\text{air}} T$ it comes (using Mayer's relationship $C_{p,\text{air}} - C_{v,\text{air}} = r_{\text{air}}$):

$$\frac{d(\rho_{\text{steam}} h_{\text{steam}})}{dt} - \frac{dP_{\text{steam}}}{dt} + \rho_{\text{air}} C_{v,\text{air}} \frac{dT}{dt} = \frac{\dot{M}_{\text{br}} h_{\text{br}}}{V} \quad (3.25)$$

with $h_{\text{steam}} = h(P_{\text{steam}}(t), T(t))$.

3.1.1.5 Steam described by the IAPWS tables

The IAPWS tables provide tabulated values for the reference EoS allowing an accurate description of the steam thermodynamic behaviour. In particular, it is possible to compute $h_{\text{steam}} = h(P_{\text{steam}}, T)$. Going back to eq. 3.25 and introducing the expressions of $\rho_{\text{steam}}(t)$, $P_{\text{steam}}(t)$ one can obtain:

$$\frac{d\rho_{\text{steam}}(t)}{dt} h_{\text{steam}}(t) + \rho_{\text{steam}}(t) \frac{dh_{\text{steam}}(t)}{dt} - \frac{dP_{\text{steam}}}{dt} + \rho_{\text{air}} C_{v,\text{air}} \frac{dT}{dt} = \frac{\dot{M}_{\text{br}}(t) h_{\text{br}}}{V} \quad (3.26)$$

In the general case $\dot{M}_{\text{br}}(t)$ is not necessarily constant and non zero until $t = t_1$ then equal to zero until $t = t_2$ so that the general expression $\dot{M}_{\text{br}}(t)$ is kept here. Assuming no spray and no wall condensation, ρ_{steam} is such that:

$$\frac{d\rho_{\text{steam}}}{dt} = \frac{\dot{M}_{\text{br}}(t)}{V} \quad (3.27)$$

Proceed coupling the mass conservation and the energy conservation in the following system of equations:

$$\begin{cases} \frac{d\rho_{\text{steam}}}{dt} = \frac{\dot{M}_{\text{br}}(t)}{V} \\ \frac{d\rho_{\text{steam}}(t)}{dt} h_{\text{steam}}(t) + \rho_{\text{steam}}(t) \frac{dh_{\text{steam}}(t)}{dt} - \frac{dP_{\text{steam}}}{dt} + \rho_{\text{air}} C_{v,\text{air}} \frac{dT}{dt} = \frac{\dot{M}_{\text{br}}(t) h_{\text{br}}}{V} \end{cases} \quad (3.28)$$

Since h_{steam} can be computed as $h_{\text{steam}} = h(P_{\text{steam}}, T)$ through the IAPWS tables, it is clear that the system of equations is non-linear and has three unknowns: ρ_{steam} , P_{steam} and T . In order to solve the problem, first discretize in time the two equations using a first-order Euler explicit formula:

$$\begin{cases} \frac{\rho_{\text{steam}}^{n+1} - \rho_{\text{steam}}^n}{\Delta t} = \frac{\dot{M}_{\text{br}}^n}{V} \\ \frac{\rho_{\text{steam}}^{n+1} - \rho_{\text{steam}}^n}{\Delta t} h_{\text{steam}}^n + \frac{h_{\text{steam}}^{n+1} - h_{\text{steam}}^n}{\Delta t} \rho_{\text{steam}}^n - \frac{P_{\text{steam}}^{n+1} - P_{\text{steam}}^n}{\Delta t} + \rho_{\text{air}} C_{v,\text{air}} \frac{T^{n+1} - T^n}{\Delta t} = \frac{\dot{M}_{\text{br}}^n h_{\text{br}}}{V} \end{cases} \quad (3.29)$$

where $h_{\text{steam}}^{n+1} = h(P_{\text{steam}}^{n+1}, T^{n+1})$. Since the IAPWS tables also provide $\rho_{\text{steam}} = \rho(P_{\text{steam}}, T)$, one can add a third equation to our system:

$$\begin{cases} \frac{\rho_{\text{steam}}^{n+1} - \rho_{\text{steam}}^n}{\Delta t} = \frac{\dot{M}_{\text{br}}^n}{V} \\ \frac{\rho_{\text{steam}}^{n+1} - \rho_{\text{steam}}^n}{\Delta t} h_{\text{steam}}^n + \frac{h(P_{\text{steam}}^{n+1}, T^{n+1}) - h_{\text{steam}}^n}{\Delta t} \rho_{\text{steam}}^n - \frac{P_{\text{steam}}^{n+1} - P_{\text{steam}}^n}{\Delta t} + \rho_{\text{air}} C_{v,\text{air}} \frac{T^{n+1} - T^n}{\Delta t} = \frac{\dot{M}_{\text{br}}^n h_{\text{br}}}{V} \\ \rho(P_{\text{steam}}^{n+1}, T^{n+1}) = \rho_{\text{steam}}^{n+1} \end{cases} \quad (3.30)$$

The system can be solved numerically using an available non-linear equation solver (i.e. *fsolve* for Python or MATLAB), finding the new states $\rho_{\text{steam}}^{n+1}$, P_{steam}^{n+1} and T^{n+1} . Notice that, in this last system of equations, the quantities $h(P_{\text{steam}}^{n+1}, T^{n+1})$ and $\rho(P_{\text{steam}}^{n+1}, T^{n+1})$ are computed as a call to the IAPWS tables. Once the system is solved, one can compute the new partial pressure of air $P_{\text{air}}^{n+1} = \rho_{\text{air}} r_{\text{air}} T^{n+1}$ and therefore the new total pressure in the containment $P^{n+1} = P_{\text{steam}}^{n+1} + P_{\text{air}}^{n+1}$.

3.1.2 Configuration 1: no spray, with wall condensation

Here the 0D containment model just developed in the previous subsection (*Configuration 0*) is extended by adding the contribution of wall condensation to the mass and energy conservation equations.

3.1.2.1 Preliminary remarks

Introducing the wall condensation phenomenon, a certain volume of liquid water V_L will develop inside the containment in addition to the gaseous mixture volume V_G (air + steam). Consequently, the containment volume V (control volume) can be written as the sum of V_G and V_L :

$$V = V_G(t) + V_L(t) = \text{constant} \quad (3.31)$$

3.1.2.2 Mass conservation

The wall condensation phenomenon generates a certain mass flow rate $\dot{M}_{\text{cd-w}}$ that can be evaluated with the wall condensation model presented in the previous chapter (see eq. 2.30). This mass flow rate is such that the mass conservation for the mass of liquid water M_{water} can be written as follows (assuming $\rho_{\text{water}} = \text{constant}$ at this time, but if needed we can also consider $\rho_{\text{water}}(T)$):

$$\frac{dM_{\text{water}}}{dt} = \dot{M}_{\text{cd-w}} \quad (3.32)$$

The wall condensation mass flow rate $\dot{M}_{\text{cd-w}}$ is computed using the thermodynamic state of air and steam in the containment, so that $\dot{M}_{\text{cd-w}}(P_{\text{air}}(t), P_{\text{steam}}(t), T(t))$. Remembering that $M_{\text{water}} = \rho_{\text{water}} V_{\text{L}}(t)$, one can write:

$$\rho_{\text{water}} \frac{dV_{\text{L}}}{dt} = \dot{M}_{\text{cd-w}}(P_{\text{air}}(t), P_{\text{steam}}(t), T(t)) \quad (3.33)$$

For air it can be simply written:

$$\begin{aligned} \frac{dM_{\text{air}}}{dt} = 0 & \quad \Leftrightarrow \quad \frac{d}{dt}(\rho_{\text{air}}(t)V_{\text{G}}(t)) = 0 \\ \Rightarrow \quad \frac{d\rho_{\text{air}}(t)}{dt} &= \frac{\rho_{\text{air}}(t)}{V - V_{\text{L}}(t)} \frac{dV_{\text{L}}(t)}{dt} \end{aligned} \quad (3.34)$$

The effect of the wall condensation phenomenon is to reduce the amount of steam present in the containment with a flow rate equal to $\dot{M}_{\text{cd-w}}$, while the amount of air is not affected as air is considered non-condensable. Since the amount of steam in the containment increases due to the steam injected through the breach with a mass flow rate \dot{M}_{br} , the mass conservation for steam can be written as follows:

$$V_{\text{G}}(t) \frac{d\rho_{\text{steam}}}{dt} = \dot{M}_{\text{br}} - \dot{M}_{\text{cd-w}} + \rho_{\text{steam}} \frac{dV_{\text{L}}}{dt} \quad (3.35)$$

Note that the volume of liquid water generated by wall condensation V_{L} can be considered negligible with respect to the volume of the gaseous mixture V_{G} present in the containment ($V_{\text{L}} \ll V_{\text{G}}$), so that one can assume $\frac{dV_{\text{L}}}{dt} \approx 0$ and therefore $V \approx V_{\text{G}}$.

3.1.2.3 Energy conservation

The energy conservation equation for the gaseous mixture can be written as follows:

$$\frac{d}{dt} \int_{V_{\text{G}}} (\rho h)_{\text{G}} dV - \frac{dP(t)}{dt} V_{\text{G}} + P(t) \frac{dV_{\text{L}}}{dt} = \dot{M}_{\text{br}} h_{\text{br}} - \dot{M}_{\text{cd-w}} (h_{\text{st,b}} - h_{\text{liq,w}}) - h_{\text{cv}} S (T - T_{\text{w}}) \quad (3.36)$$

where $h_{\text{st,b}} = h_{\text{steam}}(P_{\text{steam}}, T)$ is the steam enthalpy at the bulk conditions and $h_{\text{liq,w}} = h_{\text{liq}}(P, T_{\text{w}})$ the liquid enthalpy at the total pressure and the wall temperature T_{w} . The terms $\dot{M}_{\text{cd-w}}(h_{\text{st,b}} - h_{\text{liq,w}})$ and $h_{\text{cv}} S (T - T_{\text{w}})$ represent respectively the latent (condensation) power and the sensible (convection) power exchanged between the wall and the gaseous mixture, where h_{cv} is the convective heat transfer coefficient (see subsection 2.3.1) and S is the heat exchange surface (area of the internal surface of the containment wall).

In what follows, for the sake of simplicity, it is assumed $\rho_{\text{air}} \approx \text{constant}$ and $V \approx V_{\text{G}}$. The energy balance for the gas mixture can be slightly simplified:

$$\frac{d(\rho_{\text{steam}} h_{\text{steam}})}{dt} V - \frac{dP_{\text{steam}}}{dt} V + \rho_{\text{air}} C_{\text{v,air}} V \frac{dT}{dt} = \dot{M}_{\text{br}} h_{\text{br}} - \dot{M}_{\text{cd-w}} (h_{\text{st,b}} - h_{\text{liq,w}}) - h_{\text{cv}} S (T - T_{\text{w}}) \quad (3.37)$$

3.1.2.4 System to solve

Similarly to what was done for *Configuration 0*, the system of equations that allows us to evaluate $\rho_{\text{steam}}(t)$, $P_{\text{steam}}(t)$ and $T(t)$ is shown below:

$$\begin{cases} \frac{d\rho_{\text{st}}}{dt} = \frac{\dot{M}_{\text{br}}(t)}{V} - \frac{\dot{M}_{\text{cd-w}}(\rho_{\text{st}}(t), P_{\text{st}}(t), T(t))}{V} \\ \frac{d\rho_{\text{st}}}{dt} h_{\text{st}} + \rho_{\text{st}} \frac{dh_{\text{st}}}{dt} - \frac{dP_{\text{st}}}{dt} + \rho_{\text{air}} C_{v,\text{air}} \frac{dT}{dt} = \\ = \frac{\dot{M}_{\text{br}} h_{\text{br}}}{V} - \frac{1}{V} \dot{M}_{\text{cd-w}}(\rho_{\text{st}}(t), P_{\text{st}}(t), T(t)) [h_{\text{st}}(P_{\text{st}}(t), T(t)) - h_{\text{liq}}(P(t), T_w)] + \\ - h_{\text{cv}}(\rho_{\text{st}}(t), P_{\text{st}}(t), T(t)) \frac{S}{V} (T(t) - T_w) \\ \rho(P_{\text{st}}(t), T(t)) - \rho_{\text{st}}(t) = 0 \end{cases} \quad (3.38)$$

Since it is again a non-linear system of equations, it can be discretized in time using a first-order Euler explicit formula:

$$\begin{cases} \frac{\rho_{\text{st}}^{n+1} - \rho_{\text{st}}^n}{\Delta t} = \frac{\dot{M}_{\text{br}}^n}{V} - \frac{\dot{M}_{\text{cd-w}}(\rho_{\text{st}}^n, P_{\text{st}}^n, T^n)}{V} \\ \frac{\rho_{\text{st}}^{n+1} - \rho_{\text{st}}^n}{\Delta t} h_{\text{st}}^n + \frac{h_{\text{st}}^{n+1} - h_{\text{st}}^n}{\Delta t} \rho_{\text{st}}^n - \frac{P_{\text{st}}^{n+1} - P_{\text{st}}^n}{\Delta t} + \rho_{\text{air}} C_{v,\text{air}} \frac{T^{n+1} - T^n}{\Delta t} = \\ = \frac{\dot{M}_{\text{br}}^n h_{\text{br}}}{V} - \frac{1}{V} \dot{M}_{\text{cd-w}}(\rho_{\text{st}}^n, P_{\text{st}}^n, T^n) [h_{\text{st}}(P_{\text{st}}^n, T^n) - h_{\text{liq}}(P^n, T_w)] + \\ - h_{\text{cv}}(\rho_{\text{st}}^n, P_{\text{st}}^n, T^n) \frac{S}{V} (T^n - T_w) \\ \rho(P_{\text{st}}^{n+1}, T^{n+1}) = \rho_{\text{st}}^{n+1} \end{cases} \quad (3.39)$$

As already explained for *Configuration 0*, the system can be solved numerically using an available non-linear equation solver (i.e. *fsolve* for Python or MATLAB), finding the new states ρ_{st}^{n+1} , P_{st}^{n+1} and T^{n+1} . Once the system is solved, one can compute the new partial pressure of air $P_{\text{air}}^{n+1} = \rho_{\text{air}} r_{\text{air}} T^{n+1}$ and therefore the new total pressure in the containment $P^{n+1} = P_{\text{st}}^{n+1} + P_{\text{air}}^{n+1}$.

3.1.3 Configuration 2: with spray, with wall condensation

At this point the development of the complete 0D containment model is presented, taking into account all three contributions mentioned at the beginning of this chapter: steam injection through the breach, water droplet injection through the spray system, interaction with the containment walls.

3.1.3.1 Mass conservation

The activation of the containment spray system (CSS) induces a certain condensation mass flow rate $\dot{M}_{\text{cd-sp}}$ inside the containment and consequently causes an increase or decrease in the amount of steam. The mass conservation for steam can be written as follows:

$$\frac{d\rho_{\text{st}}}{dt} = \frac{\dot{M}_{\text{br}}(t)}{V} - \frac{\dot{M}_{\text{cd-w}}(\rho_{\text{st}}(t), P_{\text{st}}(t), T(t))}{V} - \frac{\dot{M}_{\text{cd-sp}}(\rho_{\text{st}}(t), P_{\text{st}}(t), T(t))}{V} \quad (3.40)$$

In the following it is explained how to evaluate $\dot{M}_{\text{cd-sp}}$ starting from the One-drop model (presented in the first chapter of this work) and knowing the mass flow rate \dot{M}_{sp} at which the spray is injected in the containment.

Suppose one wants to follow the evolution of $P(t)$ and $T(t)$ in the containment from $t = 0$ to $t = t_{\text{end}}$, it is necessary to discretize this time interval with a certain time-step Δt to solve numerically the conservation equations. It is also assumed that the spray is injected from a certain time t (usually when P reaches a certain threshold value) from a certain height D_{fall} . Using the One-drop model you can follow the fall of a single drop and calculate the condensation flow rate $\dot{M}_{\text{cd-1drop}}(x, t)$ (corresponding to m_d calculated using eq. 1.6) generated by it at each vertical position x at time t (the injection position corresponds to $x = 0$, while the end of the fall corresponds to the x position at which the droplet is completely vaporized or to $x = D_{\text{fall}}$ if the droplet reaches the ground of the containment). Suppose that one drop is injected after each time-step Δt . Each drop is injected with the same initial conditions (diameter, temperature, velocity), but at the moment of injection it will be subjected to new containment conditions related to the evolution of $P(t)$ and $T(t)$. In this way you can simultaneously follow the fall of each injected drop and calculate its $\dot{M}_{\text{cd-1drop}}(x, t)$. At this point, to simulate the injection of a spray you need a set of drops to be injected at each time-step and not a single drop. You have as a known quantity the spray mass flow rate \dot{M}_{sp} , from which you can derive the number of drops $N_{\text{drops}}(x, t)$ present at each position x at time t using the following equation:

$$N_{\text{drops}}(x, t) = \frac{\dot{M}_{\text{sp}} \Delta t}{m_d(x, t)} \quad (3.41)$$

where $m_d(x, t)$ is the mass of the single drop at each position x at time t , calculated through the One-drop model (see eq. 1.33). Calculating the product $\dot{M}_{\text{cd-1drop}}(x, t) \cdot N_{\text{drops}}(x, t)$ we obtain the condensation flow rate related to each set of droplet and, finally, summing it over all positions x you get the spray condensation flow rate $\dot{M}_{\text{cd-sp}}(t)$:

$$\dot{M}_{\text{cd-sp}}(t) = \sum_x \dot{M}_{\text{cd-1drop}}(x, t) \cdot N_{\text{drops}}(x, t) \quad (3.42)$$

This just presented is a very simplified model for the simulation of a spray injection, in order to develop it the interaction phenomena between the drops have been neglected and, as already known, the distribution of pressure and temperature inside the containment is considered spatially homogeneous and uniform (0D containment model).

As a remark, it is necessary to point out that $\dot{M}_{\text{cd-1drop}}(x, t)$ can take both positive and negative values: $\dot{M}_{\text{cd-1drop}}(x, t) > 0$ means that the steam in the containment is condensing on the droplet (decreasing the amount of steam in the containment), vice versa $\dot{M}_{\text{cd-1drop}}(x, t) < 0$ means that the droplet is vaporizing causing an increase in the amount of steam in the containment.

3.1.3.2 Energy conservation

The energy conservation equation for the gaseous mixture can be written as follows:

$$\begin{aligned} & \frac{d\rho_{\text{st}}}{dt} h_{\text{st}} + \frac{dh_{\text{st}}}{dt} \rho_{\text{st}} - \frac{dP_{\text{st}}}{dt} + \rho_{\text{air}} C_{v,\text{air}} \frac{dT}{dt} = \\ & = \frac{\dot{M}_{\text{br}} h_{\text{br}}}{V} - \frac{1}{V} \dot{M}_{\text{cd-w}}(\rho_{\text{st}}(t), P_{\text{st}}(t), T(t)) [h_{\text{st}}(P_{\text{st}}(t), T(t)) - h_{\text{liq}}(P(t), T_w)] + \\ & - h_{\text{cv}}(\rho_{\text{st}}(t), P_{\text{st}}(t), T(t)) \frac{S}{V} (T(t) - T_w) - \frac{1}{V} W_{\text{lat-sp}}(\rho_{\text{st}}(t), P_{\text{st}}(t), T(t)) - \frac{1}{V} W_{\text{sens-sp}}(\rho_{\text{st}}(t), P_{\text{st}}(t), T(t)) \end{aligned} \quad (3.43)$$

where $W_{\text{lat-sp}}(t)$ and $W_{\text{sens-sp}}(t)$ are respectively the latent power and the sensible power exchanged between the spray droplets and the gas mixture.

$$W_{\text{lat-sp}}(t) = \dot{M}_{\text{cd-sp}}(t) \cdot [h_{\text{st}}(P_{\text{st}}(t), x_{\text{st}} = 1) - h_{\text{liq}}(P(t), x_{\text{st}} = 0)] \quad (3.44)$$

$$W_{\text{sens-sp}}(t) = \pi \lambda_{\text{g}} \cdot \sum_x [N_{\text{drops}}(x, t) \cdot Nu(x, t) \cdot d(x, t) \cdot (T(t) - T_{\text{d}}(x, t))] \quad (3.45)$$

where x_{st} is the steam quality, λ_{g} is the thermal conductivity of the gas mixture. $Nu(x, t)$, $d(x, t)$ and $T_{\text{d}}(x, t)$ are respectively the Nusselt number, the diameter and the temperature of the single droplet at each position x at time t , calculated respectively from equations 1.4, 1.33 and 1.39.

3.1.3.3 System to solve

Similarly to what was done for *Configuration 0* and *Configuration 1*, the system of equations that allows us to evaluate $\rho_{\text{steam}}(t)$, $P_{\text{steam}}(t)$ and $T(t)$ is shown below:

$$\left\{ \begin{array}{l} \frac{d\rho_{\text{st}}}{dt} = \frac{\dot{M}_{\text{br}}(t)}{V} - \frac{\dot{M}_{\text{cd-w}}(\rho_{\text{st}}(t), P_{\text{st}}(t), T(t))}{V} - \frac{\dot{M}_{\text{cd-sp}}(\rho_{\text{st}}(t), P_{\text{st}}(t), T(t))}{V} \\ \frac{d\rho_{\text{st}}}{dt} h_{\text{st}} + \rho_{\text{st}} \frac{dh_{\text{st}}}{dt} - \frac{dP_{\text{st}}}{dt} + \rho_{\text{air}} C_{\text{v,air}} \frac{dT}{dt} = \\ = \frac{\dot{M}_{\text{br}} h_{\text{br}}}{V} - \frac{1}{V} \dot{M}_{\text{cd-w}}(\rho_{\text{st}}(t), P_{\text{st}}(t), T(t)) [h_{\text{st}}(P_{\text{st}}(t), T(t)) - h_{\text{liq}}(P(t), T_{\text{w}})] + \\ - h_{\text{cv}}(\rho_{\text{st}}(t), P_{\text{st}}(t), T(t)) \frac{S}{V} (T(t) - T_{\text{w}}) + \\ - \frac{1}{V} W_{\text{lat-sp}}(\rho_{\text{st}}(t), P_{\text{st}}(t), T(t)) - \frac{1}{V} W_{\text{sens-sp}}(\rho_{\text{st}}(t), P_{\text{st}}(t), T(t)) \\ \rho(P_{\text{st}}(t), T(t)) - \rho_{\text{st}}(t) = 0 \end{array} \right. \quad (3.46)$$

Since it is again a non-linear system of equations, it can be discretized in time using a first-order Euler explicit formula:

$$\left\{ \begin{array}{l} \frac{\rho_{\text{st}}^{n+1} - \rho_{\text{st}}^n}{\Delta t} = \frac{\dot{M}_{\text{br}}^n}{V} - \frac{\dot{M}_{\text{cd-w}}(\rho_{\text{st}}^n, P_{\text{st}}^n, T^n)}{V} - \frac{\dot{M}_{\text{cd-sp}}(\rho_{\text{st}}^n, P_{\text{st}}^n, T^n)}{V} \\ \frac{\rho_{\text{st}}^{n+1} - \rho_{\text{st}}^n}{\Delta t} h_{\text{st}}^n + \frac{h_{\text{st}}^{n+1} - h_{\text{st}}^n}{\Delta t} \rho_{\text{st}}^n - \frac{P_{\text{st}}^{n+1} - P_{\text{st}}^n}{\Delta t} + \rho_{\text{air}} C_{\text{v,air}} \frac{T^{n+1} - T^n}{\Delta t} = \\ = \frac{\dot{M}_{\text{br}}^n h_{\text{br}}}{V} - \frac{1}{V} \dot{M}_{\text{cd-w}}(\rho_{\text{st}}^n, P_{\text{st}}^n, T^n) [h_{\text{st}}(P_{\text{st}}^n, T^n) - h_{\text{liq}}(P^n, T_{\text{w}})] + \\ - h_{\text{cv}}(\rho_{\text{st}}^n, P_{\text{st}}^n, T^n) \frac{S}{V} (T^n - T_{\text{w}}) + \\ - \frac{1}{V} W_{\text{lat-sp}}(\rho_{\text{st}}^n, P_{\text{st}}^n, T^n) - \frac{1}{V} W_{\text{sens-sp}}(\rho_{\text{st}}^n, P_{\text{st}}^n, T^n) \\ \rho(P_{\text{st}}^{n+1}, T^{n+1}) = \rho_{\text{st}}^{n+1} \end{array} \right. \quad (3.47)$$

As already explained for *Configuration 0* and *Configuration 1*, the system can be solved numerically using an available non-linear equation solver (i.e. *fsolve* for Python or MATLAB), finding the new states ρ_{st}^{n+1} , P_{st}^{n+1} and T^{n+1} . Once the system is solved, one can compute the new partial pressure of air $P_{\text{air}}^{n+1} = \rho_{\text{air}} r_{\text{air}} T^{n+1}$ and therefore the new total pressure in the containment $P^{n+1} = P_{\text{st}}^{n+1} + P_{\text{air}}^{n+1}$.

3.2 Comparison with literature

This section presents a comparison of the results obtained with the Containment model with similar results presented in the literature for some specific case studies. In particular, the *Delhaye Problem 11.2* [6] for *Configuration 0* and the *Benteboula-Dabbene: Test-1* [5] for *Configuration 1* are considered.

3.2.1 Delhaye problem

Here a comparison between the *Configuration 0* Containment model is presented, in which steam is described using IAPWS tables separately from air, which is instead described as a perfect gas, and the *Mixture model* presented in [6], in which the mixture of air and steam is described as a perfect gas of superheated steam.

In [6], the *Mixture model* describes the time evolution of $P(t)$ and $T(t)$ in the containment by means of two simple analytical equations (detailed derivation procedure can be found in appendix A):

$$P(t) = \frac{\gamma - 1}{V} (h_{\text{br}} - h_0) \dot{M}_{\text{br}} t + P_0 \quad T(t) = \frac{P(t)}{\frac{P_0}{T_0} + \dot{M}_{\text{br}} \frac{C_p}{V} \frac{\gamma - 1}{\gamma} t} \quad (3.48)$$

where $\gamma = C_p/C_v = 1.3$ is the ratio between the gas mixture specific thermal capacities, $V = 49\,400 \text{ m}^3$ is the containment volume, $\dot{M}_{\text{br}} = 3500 \text{ kg/s}$ and $h_{\text{br}} = 2900 \text{ kJ/kg}$ are the steam injection mass flow rate and specific enthalpy respectively, assumed constant during the entire injection time interval, $h_0 = 1900 \text{ kJ/kg}$ is a reference specific enthalpy, $P_0 = 1 \text{ bar}$ and $T_0 = 20^\circ\text{C} = 293.15 \text{ K}$ are respectively the nominal (before the steam injection) pressure and temperature in the containment.

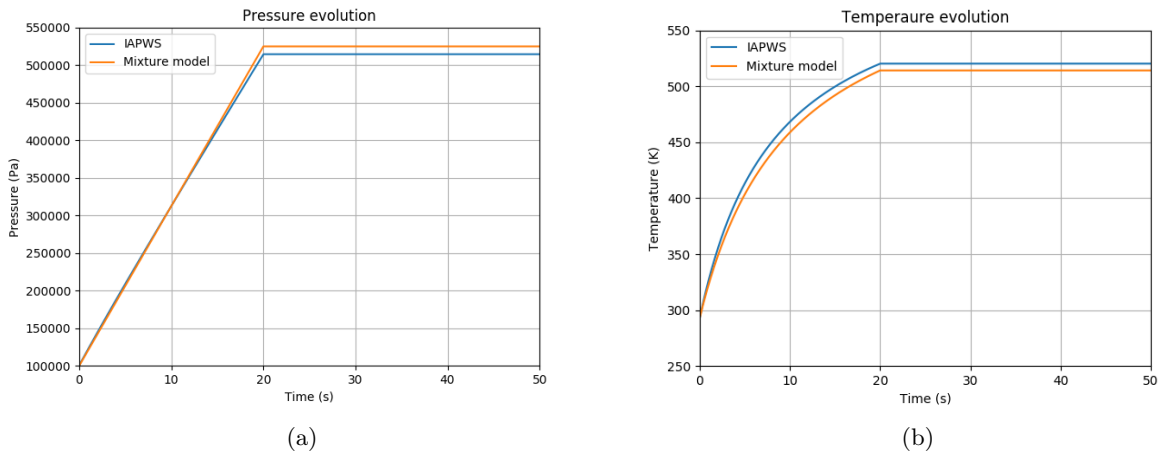


Figure 3.1: Comparison between the *Configuration 0* and the *Mixture* containment models: (a) Pressure evolution, (b) Temperature evolution.

It is assumed that the steam is injected with \dot{M}_{br} and h_{br} from time $t = 0$ to time $t = 20 \text{ s}$, so you have that both $P(t)$ and $T(t)$ remain constant for $t > 20 \text{ s}$ and equal to the values reached at $t = 20 \text{ s}$, as neither wall condensation nor spray injection is considered in this case study (*Configuration 0*). Figure 3.1 shows the comparison between the two models: they show very

similar results and one can simply see that with the *Mixture model* a slightly higher pressure value is reached than with the *Configuration 0 model*, while the opposite is true for the temperature evolution.

3.2.2 Benteboula-Dabbene: Test-1

3.2.2.1 Chilton and COPAIN correlations

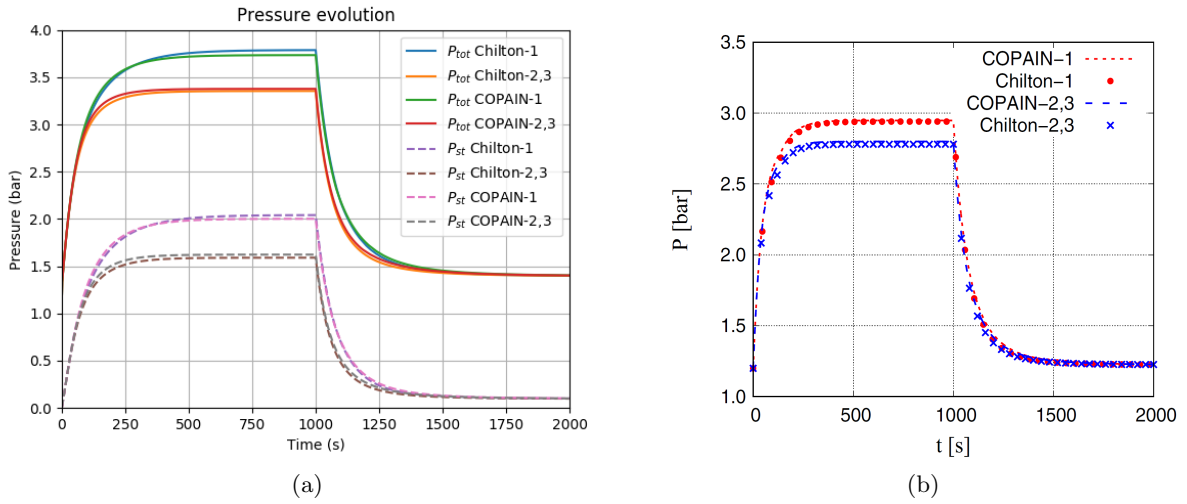


Figure 3.2: (a) Total pressure P_{tot} (bar) evolution and steam partial pressure P_{st} (bar) evolution (dashed lines) in the containment building, where $P_{st} = P_{tot} - P_{air}$ and $P_{air} = p_0 = 1.2 \text{ bar} = \text{const.}$ (b) Total pressure P (bar) evolution provided in [5].

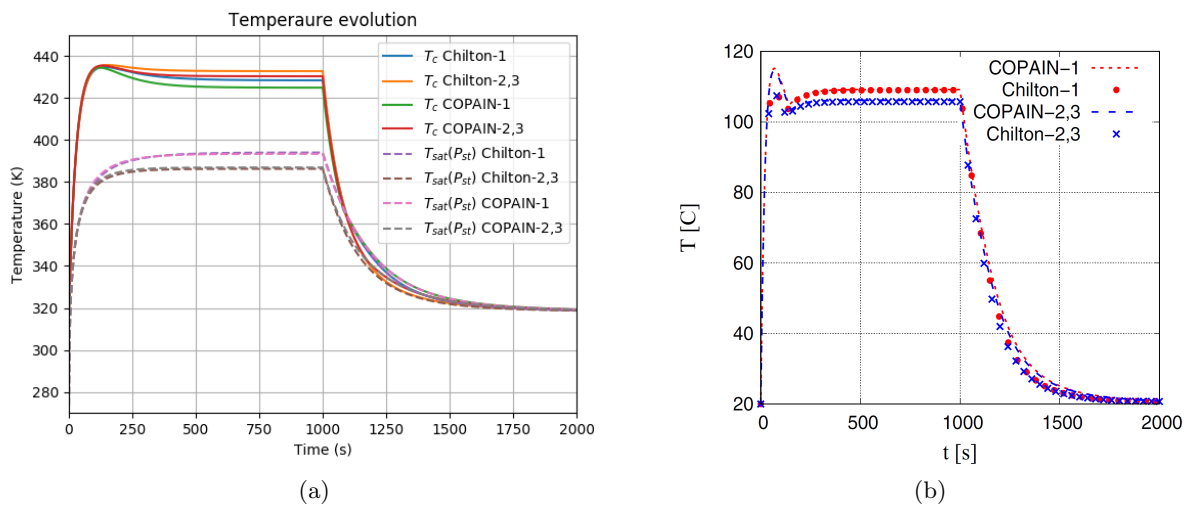


Figure 3.3: (a) Gas mixture temperature T_c (K) evolution and saturation temperature at the steam partial pressure $T_{sat}(P_{st})$ (K) evolution (dashed lines). (b) Gas mixture temperature T ($^{\circ}\text{C}$) evolution provided in [5].

The figures shown above represent a comparison between the results of *Configuration 1* Containment model (steam injection + wall condensation) and the results presented in [5] for the *Benteboula-Dabbene: Test-1*. These figures are the same as those already shown in the previous chapter, so for the related comments reference can be made to the subsection 2.5.2.

3.2.2.2 Tagami and Uchida correlations and condensation ratio maps

Further results in which the *Benteboula-Dabbene: Test-1* was again reproduced with the *Configuration 1* Containment model are shown below, but using the formulations of Uchida and Tagami to calculate the contribution of wall condensation.

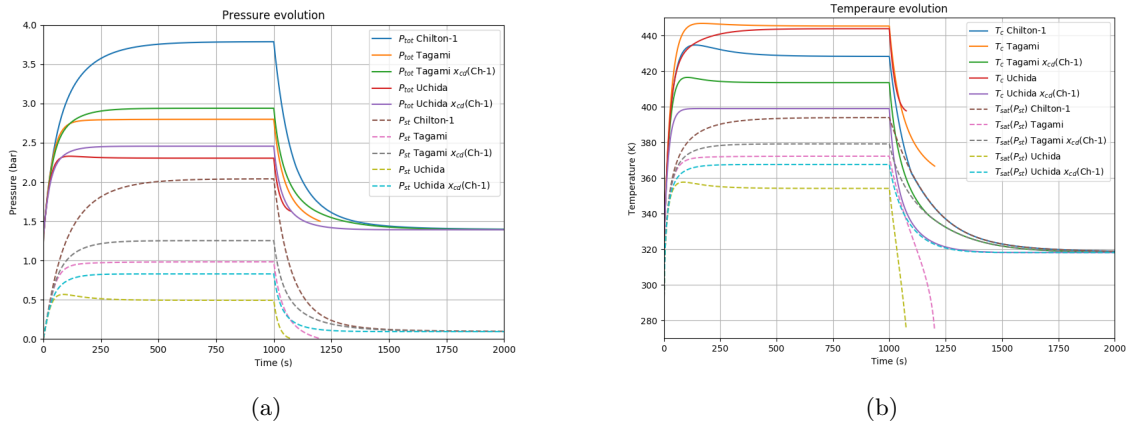


Figure 3.4: (a) Total pressure P_{tot} (bar) evolution and steam partial pressure P_{st} (bar) evolution (dashed lines) in the containment building, where $P_{st} = P_{tot} - P_{air}$ and $P_{air} = p_0 = 1.2 \text{ bar} = \text{const.}$ Gas mixture temperature T_c (K) evolution and saturation temperature at the steam partial pressure $T_{sat}(P_{st})$ (K) evolution (dashed lines).

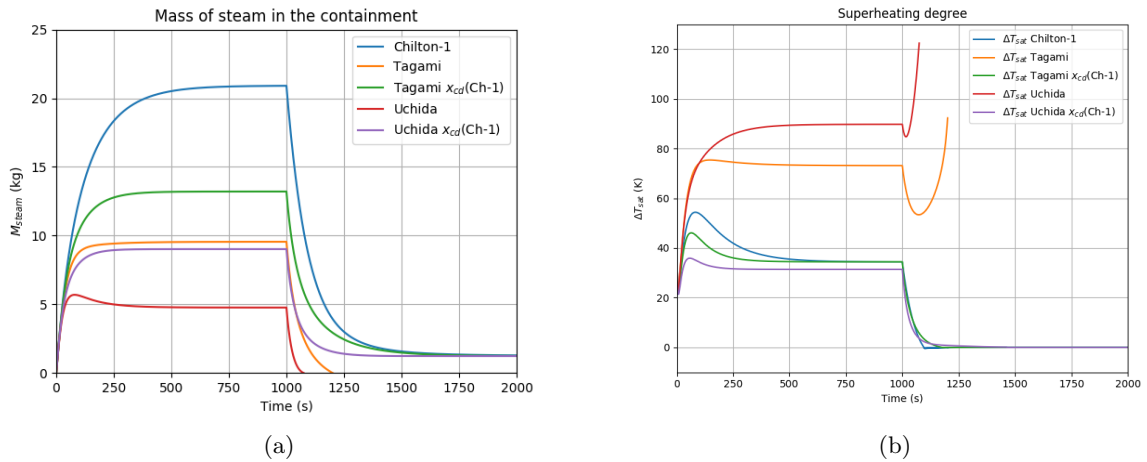


Figure 3.5: (a) Mass of steam M_{st} (kg) evolution in the containment. (b) Superheating degree ΔT_{sat} (K) evolution in the containment.

With both formulations (Uchida and Tagami), two types of condensation ratios x_{cond} were used: the historical (conservative) 92/8 repartition ($x_{\text{cond}} = 0.92$, see subsection 2.3.2) and the repartition calculated by one-way calculations using the Chilton-1 formulation $x_{\text{cond}}(\text{Ch-1})$ (condensation ratio maps, see section 2.6) through an interpolation process. In figures 3.4 and 3.5, in addition to the results just mentioned, it has also been added the result obtained with the mechanistic model (only Chilton-1) for a quick comparison.

From the figures shown above it can be clearly seen, first of all, that the Tagami and Uchida models (both with the 92/8 repartition and the $x_{\text{cond}}(\text{Ch-1})$ map) provide a higher condensation contribution than that calculated with the reference mechanistic model (Chilton-1): the maximum pressure reached (figure 3.4 (a)) in the containment using Chilton-1 is clearly higher than that reached using Tagami and Uchida; the mass of steam present in the containment (figure 3.5 (a)) reaches higher values using Chilton-1 than using Tagami and Uchida (this means precisely that for the latter the condensation is more effective).

Comparing the use of the 92/8 repartition with the use of the $x_{\text{cond}}(\text{Ch-1})$ map (considering the Tagami and Uchida models), it can be seen that, as would be expected, the use of the 92/8 repartition provides a higher condensation contribution than the use of the map, so much so that a few seconds after stopping steam injection ($t > 1000$ s) it appears that the mass of steam in the containment (figure 3.5 (a)) is completely condensed using the 92/8 repartition.

3.3 Main case study: MSLB simulation with spray activation and wall condensation

This section presents the main case study of this work: Main Steam Line Break (MSLB) simulation. The case study considers the occurrence of a rupture in the main steam line inside the containment building of a Pressurized Water Reactor (PWR). The injection of steam due to the rupture causes a superheated atmosphere (mixture of air and superheated steam) to form inside the containment, resulting in an increase in pressure and temperature. As mitigation systems, two driving phenomena are considered to control the evolution of pressure and temperature: the heat and mass transfers between the superheated atmosphere and the walls of the containment (wall condensation) and the heat and mass transfers between the superheated atmosphere and the liquid water droplets injected by the Containment Spray System (CSS).

The following list summarises the complete configuration of the case study. This configuration was created by considering data found in the literature.

-• Containment [14]

- Initial pressure: $P_0 = 0.98$ bar (only air in the containment $\rightarrow P_{\text{air},0} = P_0$)
- Initial temperature: $T_0 = 322$ K
- Volume: $V = 47\,500$ m³
- Elevation and inner radius: $H = 55$ m $R_i = 19$ m

-• Steam injection [6]

- Injection pressure: $P_{\text{st},\text{inj}} = 4$ bar
- Injection temperature: $T_{\text{st},\text{inj}} = 473.15$ K
- Injection (breach) enthalpy : $h_{\text{br}} = h(P_{\text{st},\text{inj}}, T_{\text{st},\text{inj}})$

- Injection mass flow rate

$$\dot{M}_{\text{br}} = 3500 \text{ kg/s} \quad \text{if } 0 < t < t_{\text{st,inj}}$$

$$\dot{M}_{\text{br}} = 0 \text{ kg/s} \quad \text{otherwise}$$

-• Spray injection

- Spray system activates when $P > 2 \text{ bar}$ [14]
- Injection mass flow rate
 1. Configuration 1: No spray activated
 2. Configuration 2: Spray mass flow rate $\rightarrow \dot{M}_{\text{sp}} = 280 \text{ kg/s}$ [3]
- Initial droplet temperature: $T_{\text{d},0} = 293.15 \text{ K}$
- Initial droplet diameter: $d_0 = 1 \text{ mm}$
- Initial droplet velocity: $v_0 = 15 \text{ m/s}$
- Falling height for the droplets: $D_{\text{fall}} = 20 \text{ m}$

-• Spray injection models

- Mechanistic model: Spray model (from One-drop model) M1
- Historical (conservative) model (92/8 repartition)

$$W_{\text{tot-sp}} = \dot{M}_{\text{sp}} \cdot C_{\text{p,sp}} \cdot (T_{\text{sat}}(P_{\text{steam}}) - T_{\text{sp},0}) \quad \text{with} \quad T_{\text{sp},0} = T_{\text{d},0} \quad (3.49)$$

$$W_{\text{lat-sp}} = 0.92 \cdot W_{\text{tot-sp}} \quad W_{\text{sens-sp}} = W_{\text{tot-sp}} - W_{\text{lat-sp}}$$

- Historical model (x_{spray} MAPS)

$$W_{\text{tot-sp}} = \dot{M}_{\text{sp}} \cdot C_{\text{p,sp}} \cdot (T_{\text{sat}}(P_{\text{steam}}) - T_{\text{sp},0}) \quad \text{with} \quad T_{\text{sp},0} = T_{\text{d},0} \quad (3.50)$$

$$W_{\text{lat-sp}} = x_{\text{spray}} \cdot W_{\text{tot-sp}} \quad W_{\text{sens-sp}} = W_{\text{tot-sp}} - W_{\text{lat-sp}}$$

-• Wall condensation [5]

- Wall temperature: $T_{\text{w}} = 45 \text{ °C} = \text{constant}$
- Wall surface: $S = 2\pi R_i(R_i + H) = 8834 \text{ m}^2$
- Mechanistic models: COPAIN-1, COPAIN-2,3
- Historical (conservative) models (92/8 repartition): Tagami, Uchida
- Historical models (x_{cond} MAPS): Tagami, Uchida

-• Simulation timing

- Total simulation time: $t_{\text{end}} = 2000 \text{ s}$
- Time-step: $\Delta t = 0.01 \text{ s}$
- Stop of steam injection: $t_{\text{st,inj}} = 20 \text{ s}$

3.3.1 Mechanistic models for spray and wall condensation

Here the MSLB simulation results obtained using mechanistic models for spray injection (M1) and wall condensation (COPAIN-1 and COPAIN-2,3) are shown. Each graph shows both the results where there is CSS activation and those where there is no activation (wall condensation only), to get a clear picture of the contribution due to CSS activation.

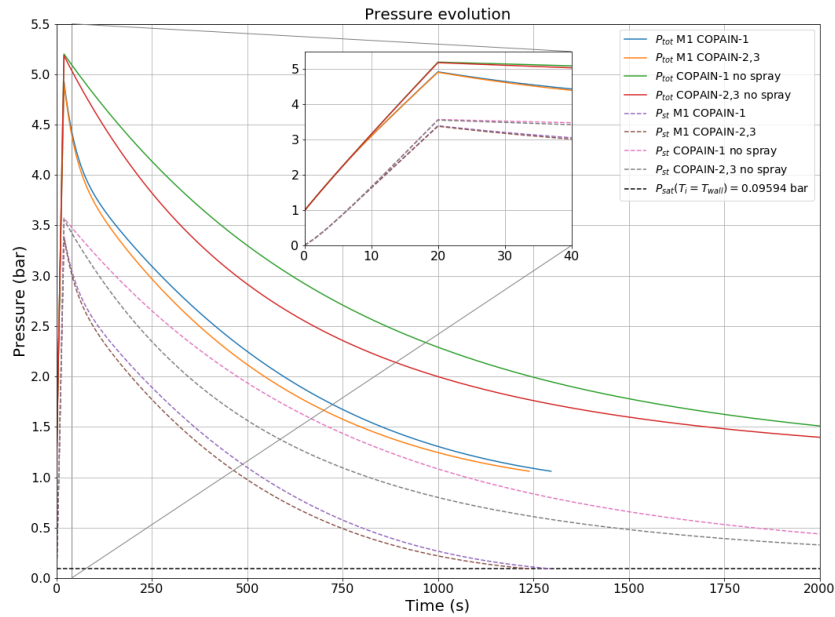


Figure 3.6: Pressure evolution.

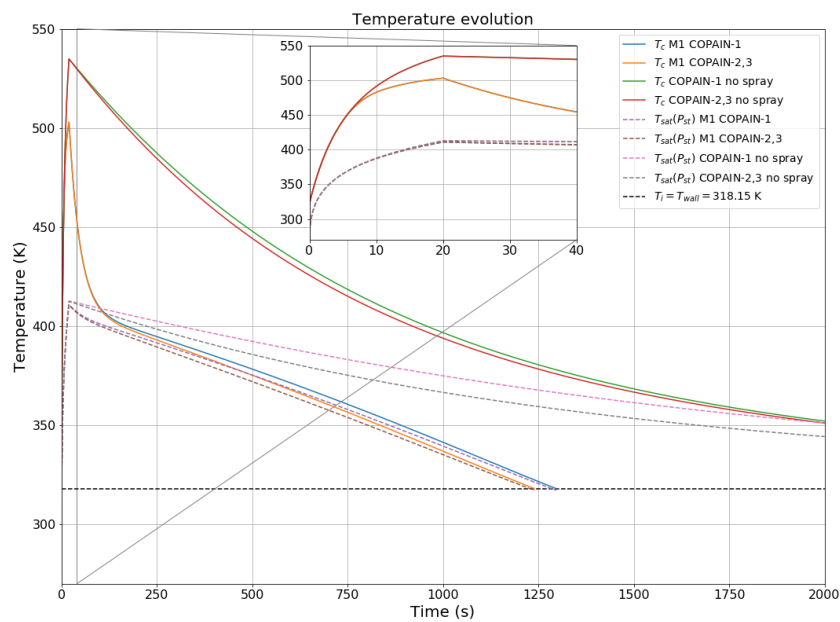


Figure 3.7: Temperature evolution.

Figures 3.6 and 3.7 represent the pressure and temperature evolution in the containment during the MSLB simulation, respectively. Steam is injected into the containment from $t = 0$ to $t = 20$ s and it is clearly seen that this causes a sudden increase in pressure and temperature in this time interval. For $t > 20$ s both pressure and temperature start to decrease and one can clearly see the difference between the case in which the CSS is activated (blue and orange lines) and the case in which only the wall condensation effect is considered (red and green lines): the activation of the CSS, which occurs when the pressure in the containment reaches 2 bar, leads to lower peak values of P and T at $t = 20$ s than in the case in which it is not activated, and subsequently leads to a faster reduction of P and T , as one would expect.

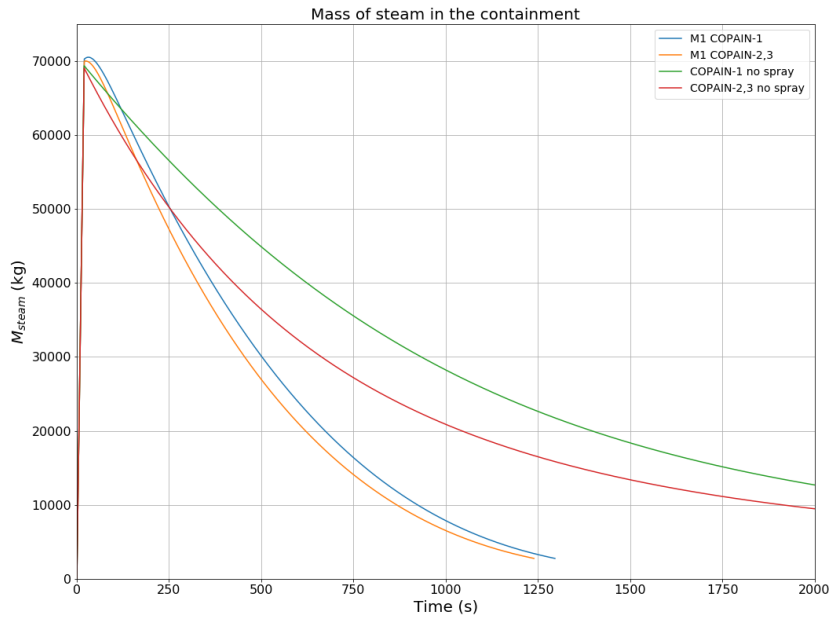


Figure 3.8: Mass of steam evolution.

It can be seen that in the case where CSS activation is considered the simulation ends at $t \approx 1250$ s, this is because at this instant the temperature in the containment reaches the saturation temperature at the steam pressure which has in turn reached the containment wall temperature ($T \approx T_{\text{sat}}(P_{\text{st}}) \approx T_w$). In addition, at this point, almost all of the steam mass in the containment is condensed (see figure 3.8).

In figure 3.8, it can be seen that during the first 200-250 seconds of the simulation something unexpected happens: the case with CSS activation is less effective in removing (condensing) the steam than the case without CSS activation, even when the steam injection is stopped ($t = 20$ s) the amount of steam continues to increase for a few moments and then decreases again. Then, for $t > 200$ s, the case with CSS activation returns to being more effective in removing the steam which, as already mentioned, is almost completely condensed at $t \approx 1250$ s. The effect found in the first 200-250 seconds is due to the fact that at the beginning of the CSS injection a negative spray condensation flow rate is induced (see figure 3.9 (a)): in this time interval you have that most of the injected droplets are vaporizing causing therefore an increase in the amount of steam in the containment; afterwards, continuing the spray injection, you have that the condensation flow rate returns to positive values, thus starting again to remove (condense) steam from the containment.

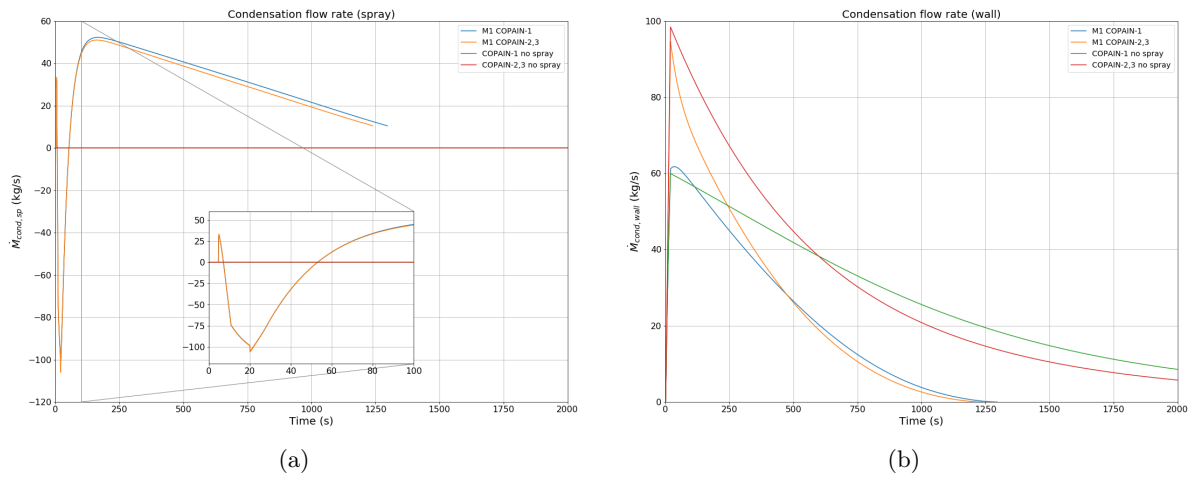


Figure 3.9: (a) Condensation flow rate due to the spray. (b) Condensation flow rate due to the wall.

Figures 3.10 and 3.11 show respectively the latent and sensible power exchanged by the containment gas mixture (air + steam) with both the CSS spray and the containment walls. With regard to the latent power due to the spray (figure 3.10 (a)) it can be seen that it follows the trend imposed by the relative condensation mass flow rate (figure 3.9 (a)) and dominates the heat transfer with respect to the relative sensible power (figure 3.11 (a)). With regard to the heat exchange between the gas mixture and the containment walls, it can be clearly seen that the latent fraction (figure 3.10 (b)) dominates over the sensible fraction (figure 3.11 (b)). To confirm these conclusions, figure 3.12 shows the total values of latent and sensible heat exchanged by the containment gas mixture with both the CSS spray and the containment walls, both when the CSS is activated and when only wall condensation is considered. These overall values are obtained by integrating the respective powers over all the simulation duration.

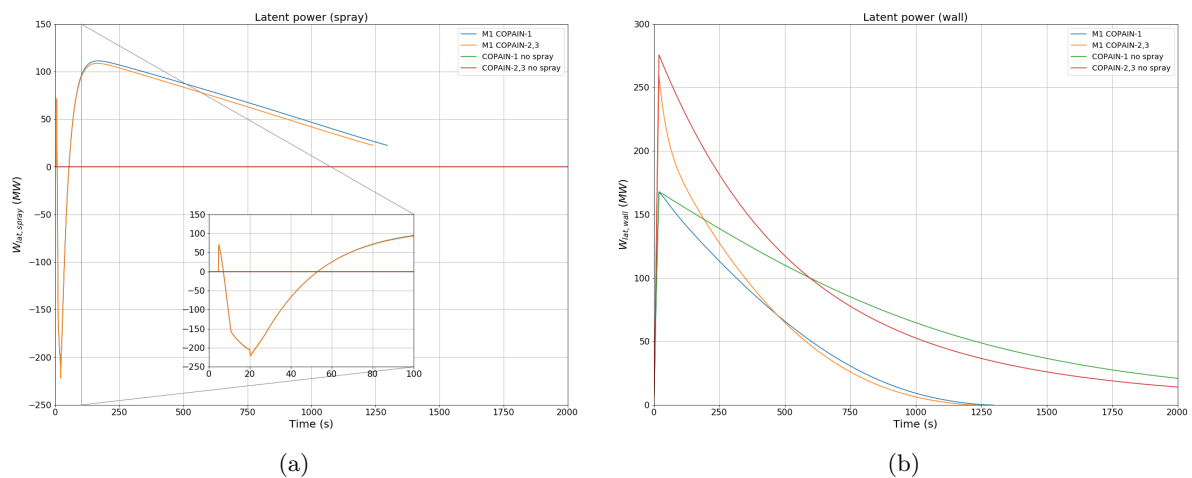


Figure 3.10: (a) Latent power exchanged due to the spray. (b) Latent power exchanged due to the wall.

3.3. Main case study: MSLB simulation with spray activation and wall condensation 101

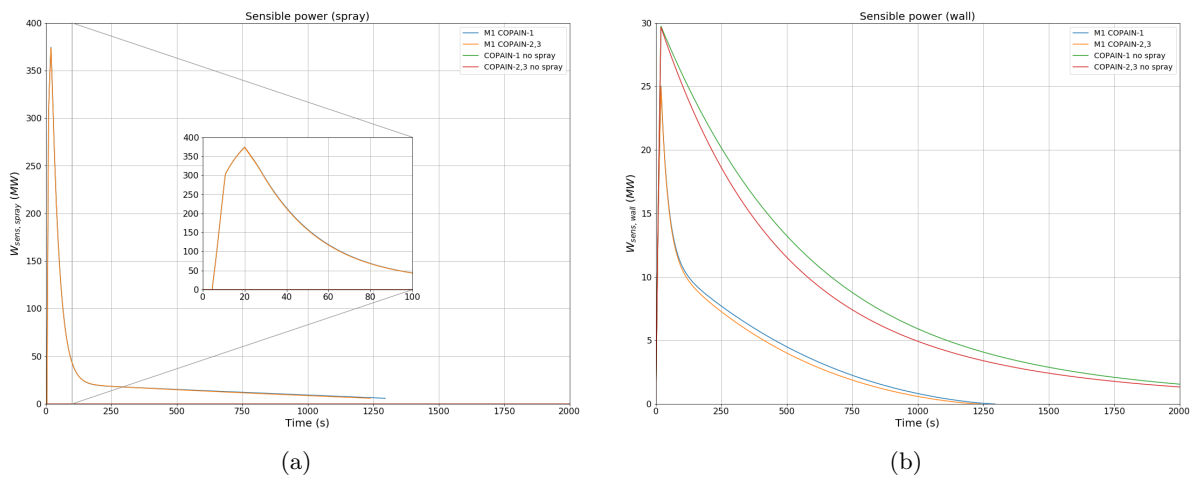


Figure 3.11: (a) Sensible power exchanged due to the spray. (b) Sensible power exchanged due to the wall.

As a final comment, it can be seen from figure 3.12 that, in the case with CSS activation, the total latent heat exchanged is almost equally divided between the spray and the wall and instead, as one would expect, in the case without CSS activation, almost the same amount of total latent heat is exchanged only through wall condensation. As regard the total sensible heat, the fraction exchanged through wall condensation is small with respect to the fraction exchanged with the spray and increases in the case without CSS activation.

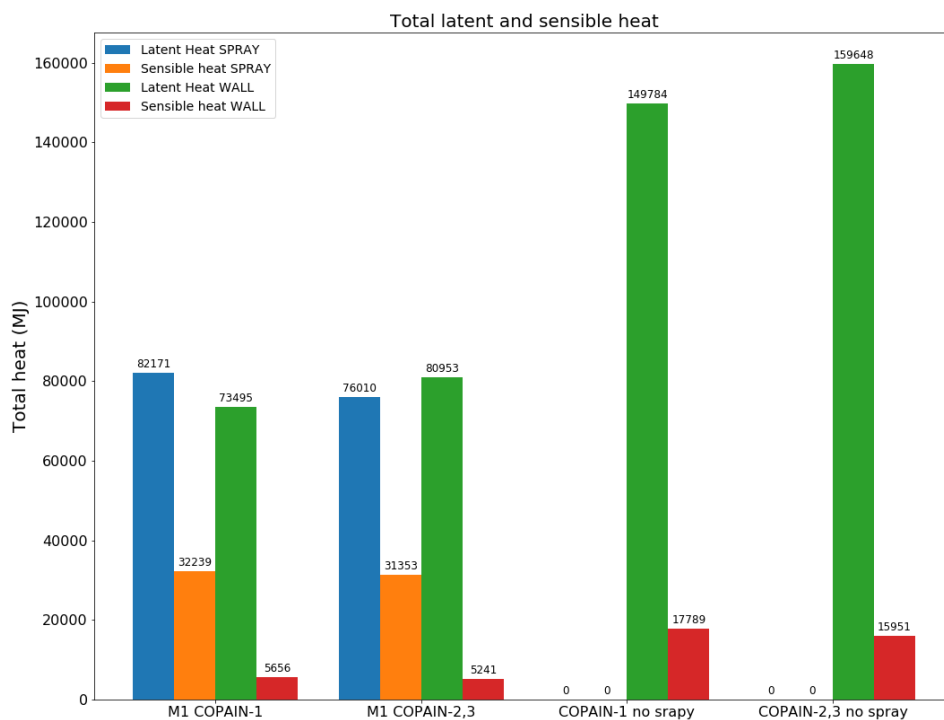


Figure 3.12: Total latent and sensible heat exchanged for the spray and for the wall.

3.3.2 Historical (conservative) models for spray and wall condensation using the 92/8 repartition

Here the MSLB simulation results obtained using the historical models for spray injection and wall condensation (Tagami and Uchida) with the 92/8 repartition are shown. Each graph shows both the results where there is CSS activation and those where there is no CSS activation.

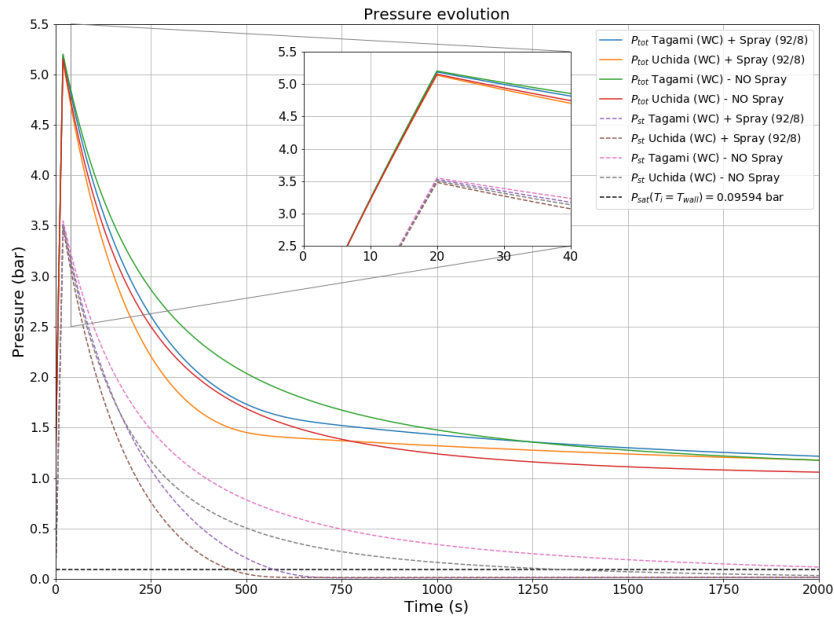


Figure 3.13: Pressure evolution.

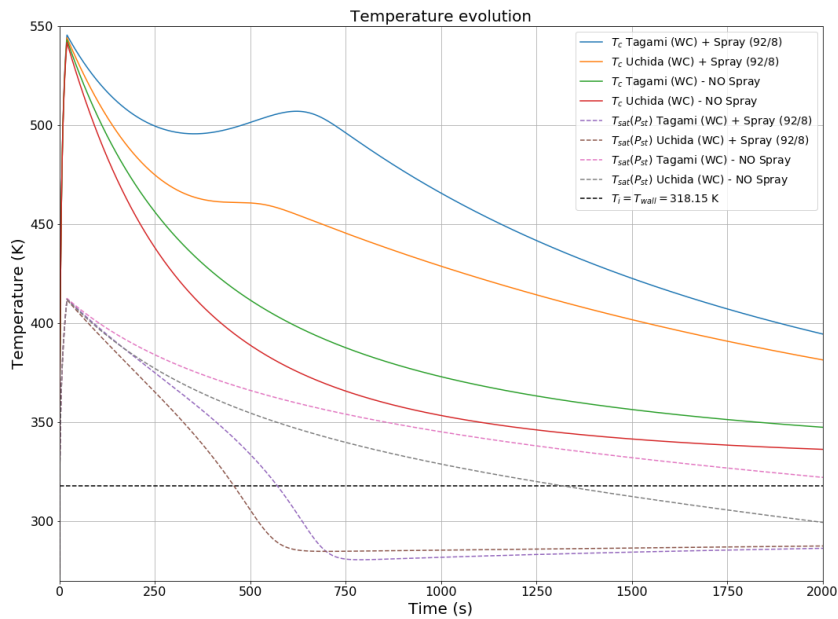


Figure 3.14: Temperature evolution.

Figures 3.13 and 3.14 show respectively the pressure and temperature evolutions inside the containment during the simulation. The use of the 92/8 heat flux repartition leads to not trivial results: the activation of the CSS does not bring a clear benefit on lowering the pressure and temperature compared to the case where CSS is not activated. These results reflect the conservative nature of the models used. With regard to temperature evolution, it can even be seen that higher peak temperatures are reached in the case of CSS activation than in the case where CSS is not activated during both the initial steam injection phase ($t \leq 20$ s) and the subsequent phase. Activation of the CSS leads to a faster reduction (condensation) of the amount of steam M_{steam} from the containment, as seen from figure 3.15, and this leads to a rapid reduction of the steam partial pressure P_{st} (figure 3.13) and a consequent rapid reduction of the saturation temperature at steam partial pressure $T_{\text{sat}}(P_{\text{st}})$ (figure 3.14). The latter, between 500 and 750 seconds, becomes lower than the spray injection temperature ($T_{\text{sp},0} = T_{\text{d},0} = 293.15$ K), making the total power $W_{\text{tot-sp}}$ (eq. 3.49) exchanged between the spray and the containment atmosphere become negative. This total power is divided into a latent ($W_{\text{lat-sp}}$, see fig. 3.17 (a)) and a sensible ($W_{\text{sens-sp}}$, see fig. 3.18 (a)) contribution, according to the 92/8 repartition, and consequently both become negative when $T_{\text{sat}}(P_{\text{st}}) < T_{\text{sp},0}$. A negative $W_{\text{lat-sp}}$ therefore results in a negative condensation flow rate due to the spray $\dot{M}_{\text{cd-sp}}$ (see fig. 3.16 (a)), which is calculated as follows:

$$\dot{M}_{\text{cd-sp}} = \frac{W_{\text{lat-sp}}}{h(P_{\text{steam}}, x = 1) - h(P_{\text{tot}}, x = 0)} \quad (3.51)$$

where x is the steam quality. Finally, $\dot{M}_{\text{cd-sp}} < 0$ means that the droplets injected by the CSS are vaporizing, causing a slight increase in the amount of steam present in the containment (see fig. 3.15). This explains the particular behaviour of the temperature evolution in the containment shown in figure 3.14.

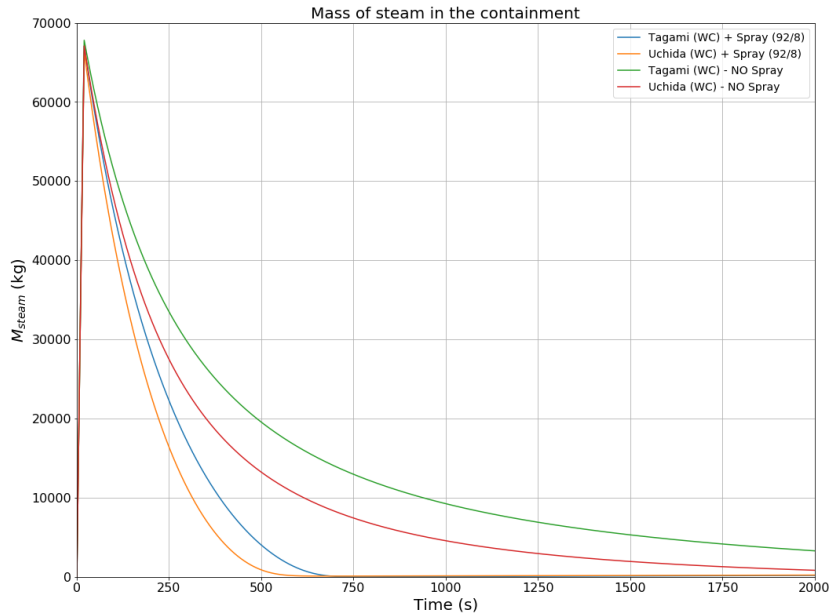


Figure 3.15: Mass of steam evolution.

Regarding the power exchanged between the containment walls and the gaseous mixture, one

proceeds by calculating the total heat flux q_w by means of the Tagami and Uchida correlations (see subsection 2.3.2) and dividing it into latent ($q_{cd} = 0.92 \cdot q_w$) and sensible ($q_{cv} = 0.08 \cdot q_w$) contributions according to the 92/8 repartition, then the relative powers, W_{lat-w} and W_{sens-w} , are calculated, knowing the heat exchange surface S , as follows:

$$W_{lat-w} = q_{cd} \cdot S \quad W_{sens-w} = q_{cv} \cdot S \quad (3.52)$$

The time evolution of W_{lat-w} and W_{sens-w} is shown in figures 3.17 (b) and 3.18 (b) respectively. By comparing with the analogous powers exchanged for the spray, it can be clearly seen that the contribution due to condensation on the walls (both latent and sensible) is clearly higher than that due to the interaction with the spray droplets. This is even clearer from the summary graph in figure 3.19, which shows the total (integral) amount of latent and sensible energy exchanged between the containment atmosphere and both the spray and the walls.

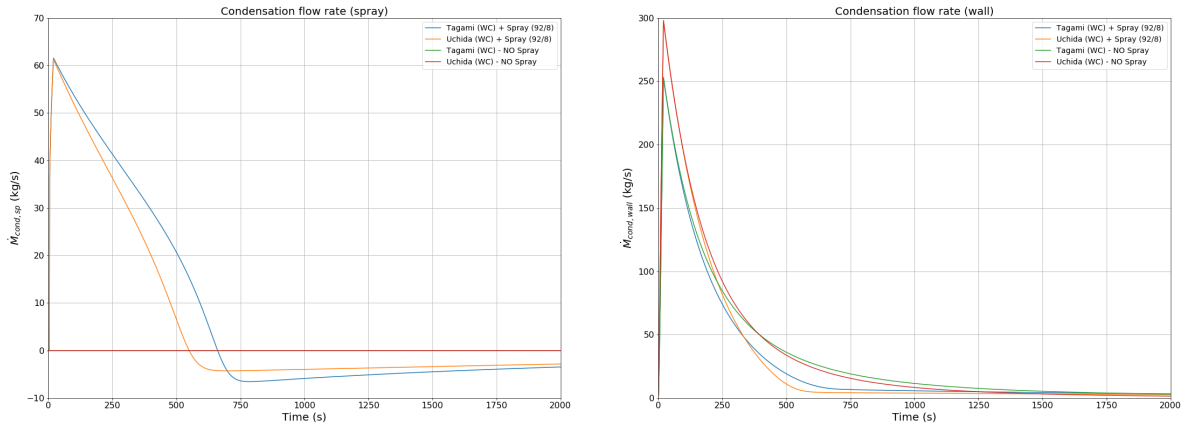


Figure 3.16: (a) Condensation flow rate due to the spray. (b) Condensation flow rate due to the wall.

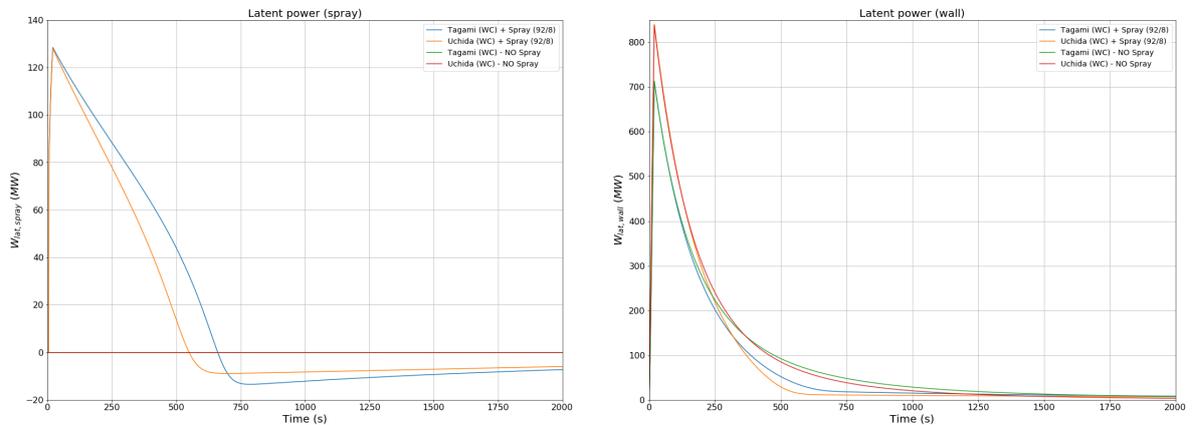


Figure 3.17: (a) Latent power exchanged due to the spray. (b) Latent power exchanged due to the wall.

3.3. Main case study: MSLB simulation with spray activation and wall condensation 105

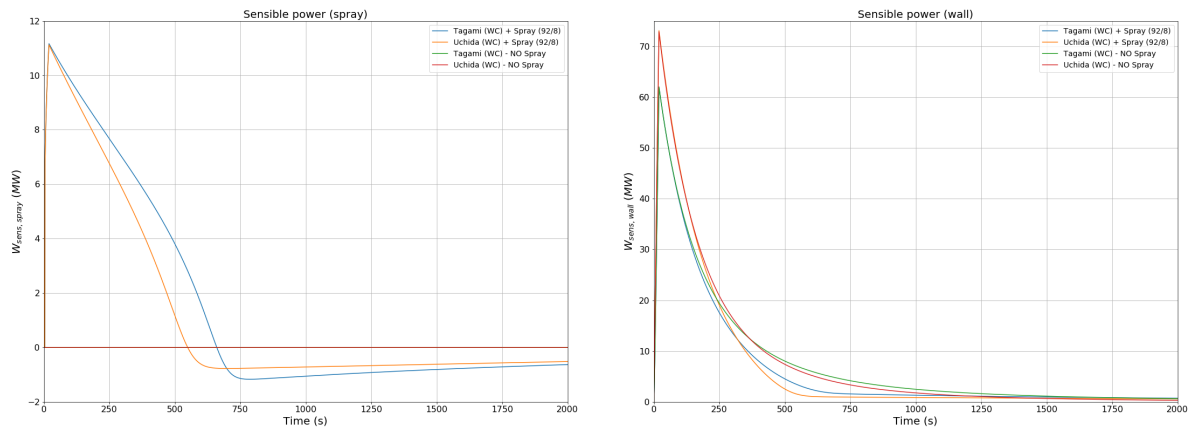


Figure 3.18: (a) Sensible power exchanged due to the spray. (b) Sensible power exchanged due to the wall.

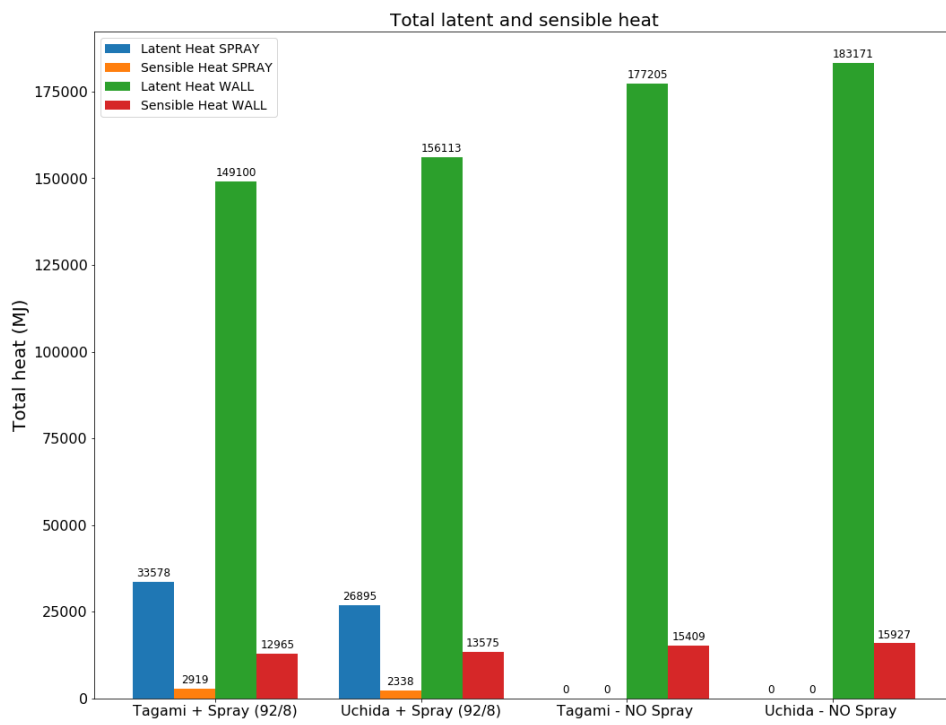


Figure 3.19: Total latent and sensible heat exchanged for the spray and for the wall.

3.3.3 Historical models for spray and wall condensation using the MAPS

This subsection presents the MSLB simulation results obtained using the historical models for CSS and Wall Condensation, as in the previous subsection, but this time the repartition between latent and sensible contribution is done using the repartition MAPS (x_{spray} and x_{cond} MAPS) obtained as described in section 1.6 for CSS and in section 2.6 for wall condensation.

The one used here represents a kind of hybrid approach as it uses the historical models for the calculation of the total powers exchanged between the CSS and the containment atmosphere (eq. 3.50) and between the walls and the containment atmosphere (Tagami and Uchida), while the repartition MAPS were obtained using the mechanistic models (M1 for the CSS and COPAIN for the wall condensation). In addition, the MAPS used here were obtained using two different formulations for the mass diffusion coefficient: D_v-1 and $D_v-2,3$.

Figures 3.20 and 3.21 show respectively the pressure and temperature evolution during the simulation.

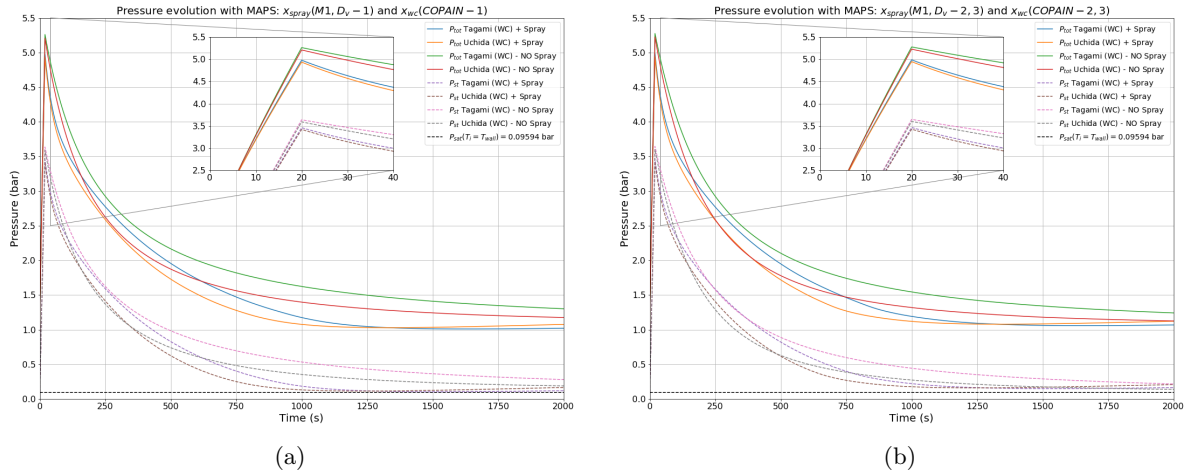


Figure 3.20: Pressure evolution using repartition maps: (a) D_v-1 , (b) $D_v-2,3$.

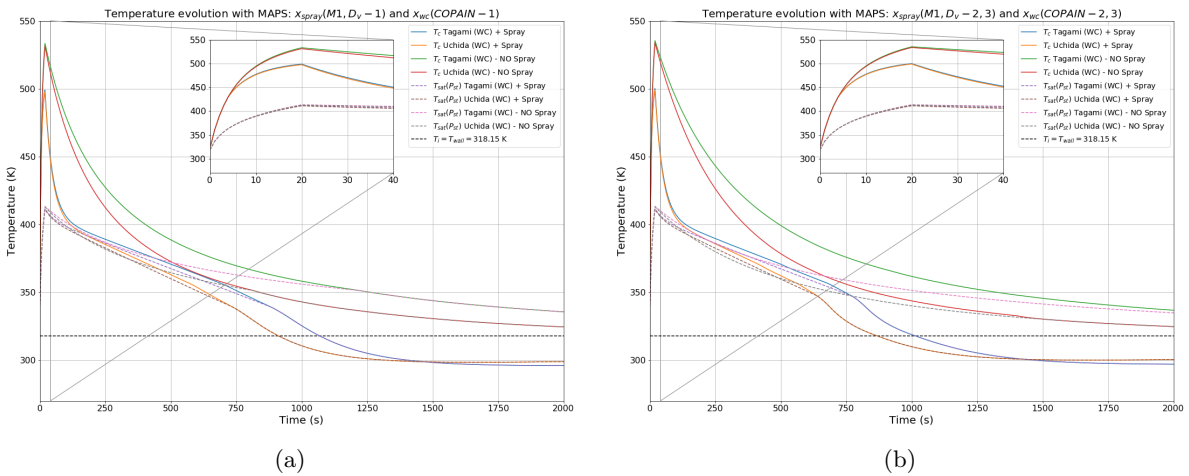


Figure 3.21: Temperature evolution using repartition maps: (a) D_v-1 , (b) $D_v-2,3$.

In this case it is clear that activating the CSS has a beneficial effect in lowering the pressure and temperature in the containment, although less beneficial than in the case where only the mechanistic models without the MAPS were used (subsection 3.3.1), but more beneficial than in the case where the historical models with the 92/8 assumption were used (subsection 3.3.2).

The following figures, similarly to the two previous subsections, show the time evolution of other important quantities: steam mass, condensation flow rate, latent and sensible powers due to both CSS and Wall Condensation.

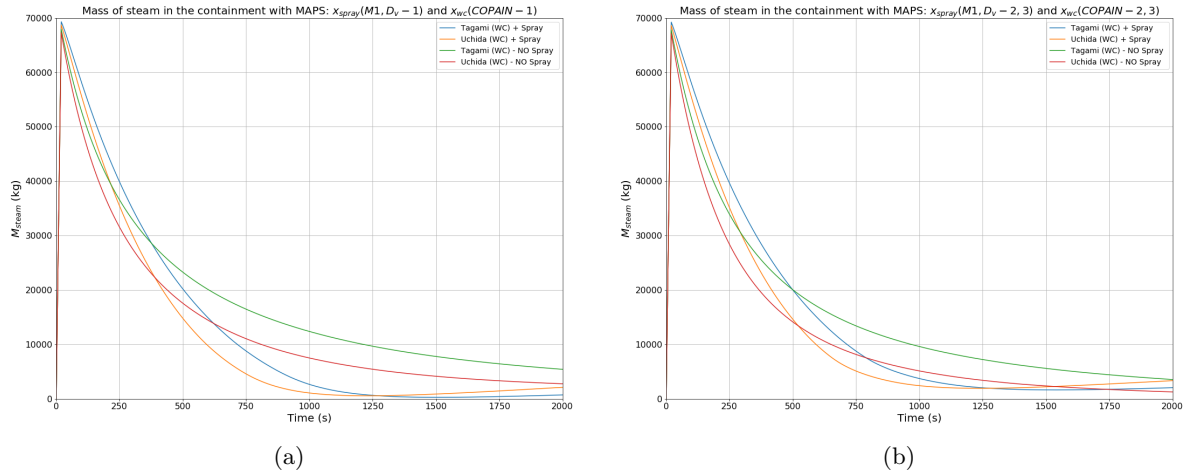


Figure 3.22: Mass of steam evolution using repartition maps: (a) D_V-1 , (b) $D_V-2,3$.

Once the total power exchanged due to CSS (W_{tot-sp}) is calculated using eq. 3.50, it is divided into latent and sensible contributions according to x_{spray} obtained through the MAPS. These maps, as explained in section 1.6, are 3D look-up tables of the type $x_{spray}(P, P_{air}, \Delta T_{sat})$: you can at each time-step of the simulation calculate x_{spray} knowing $P(t)$, $P_{air}(t)$ and $\Delta T_{sat}(t)$ (calculated solving the balance equations) by 3D interpolation.

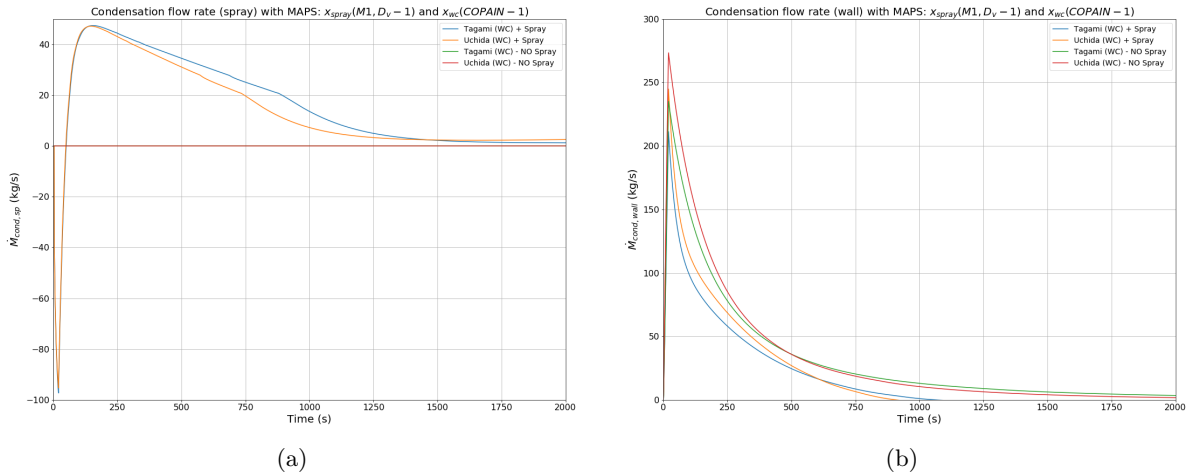


Figure 3.23: Condensation mass flow rate due to (a) the spray and to (b) the wall. Use of repartition maps with D_V-1 .

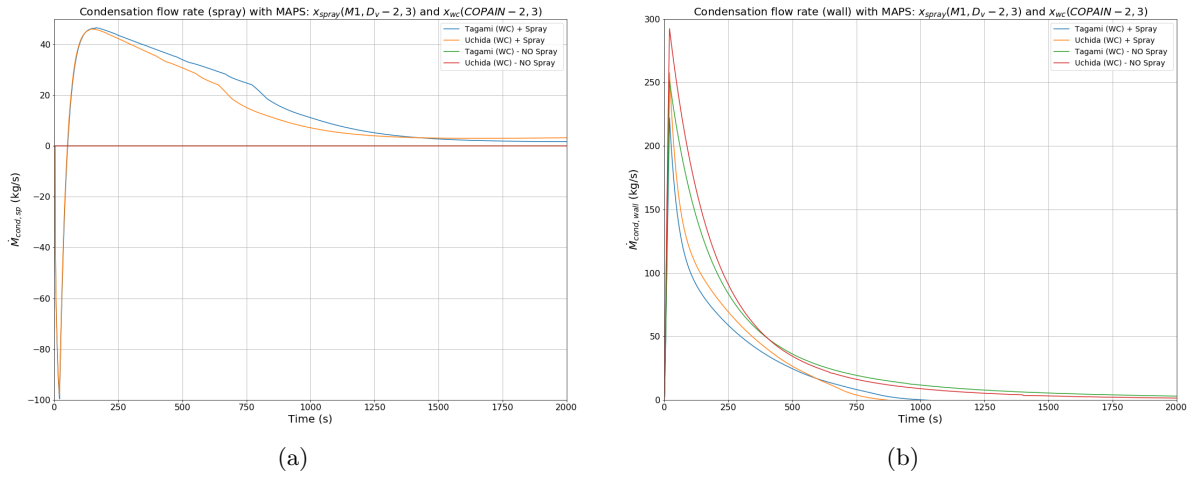


Figure 3.24: Condensation mass flow rate due to (a) the spray and to (b) the wall. Use of repartition maps with $D_v-2,3$.

A similar procedure is carried out for the calculation of the total power changed between the walls and the containment atmosphere ($W_{\text{tot-w}}$) and the use of x_{COND} MAPS to divide it in latent and sensible contributions.

Once $W_{\text{lat-sp}}$ and $W_{\text{lat-w}}$ (shown in figures 3.25, 3.26, 3.27 and 3.28) have been calculated, the respective condensation flow rates $\dot{M}_{\text{cd-sp}}$ and $\dot{M}_{\text{cd-w}}$ (shown in figures 3.23 and 3.24) can be derived using equation 3.51.

Finally, figures 3.29 and 3.30 show the total amounts of latent and sensible energy exchanged during the whole simulation in the case with and without CSS activation. It can be seen, as would be expected given the hybrid nature of the approach followed here, that the results are somewhere in between those of the previous two subsections (see figures 3.12 and 3.19 for comparison).

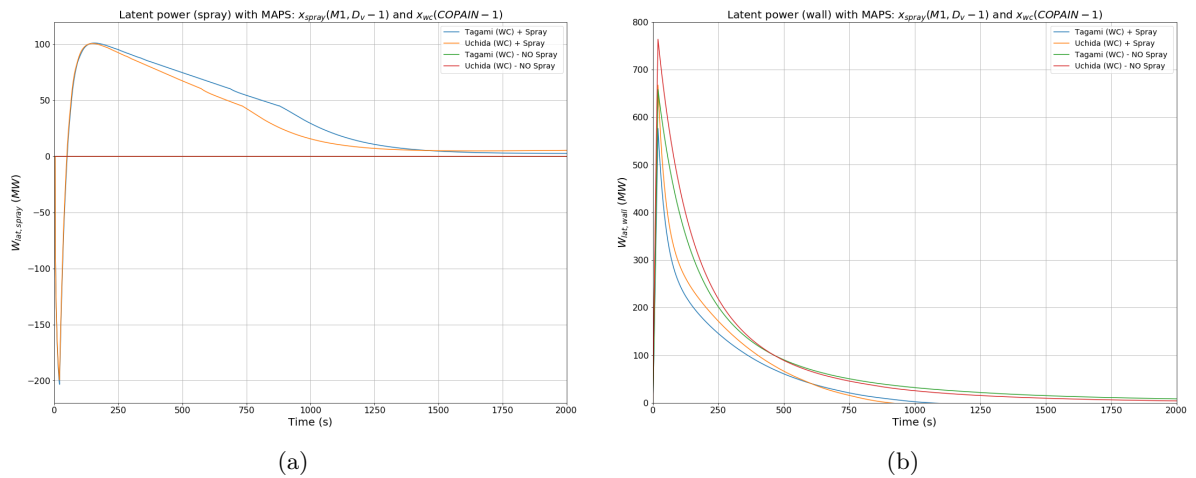


Figure 3.25: Latent power exchanged due to (a) the spray and to (b) the wall. Use of repartition maps with D_v-1 .

3.3. Main case study: MSLB simulation with spray activation and wall condensation 109

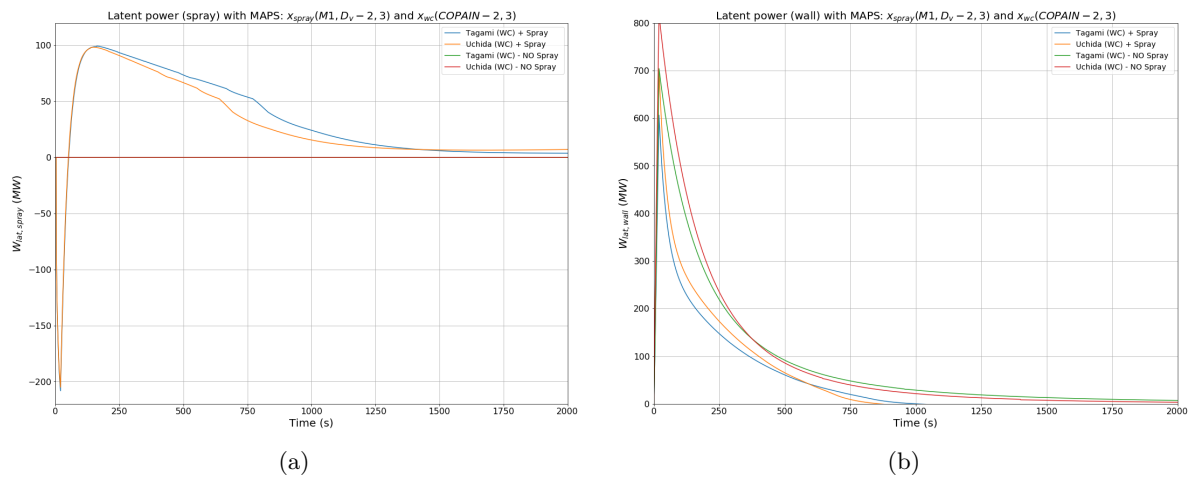


Figure 3.26: Latent power exchanged due to (a) the spray and to (b) the wall. Use of repartition maps with D_v -2,3.

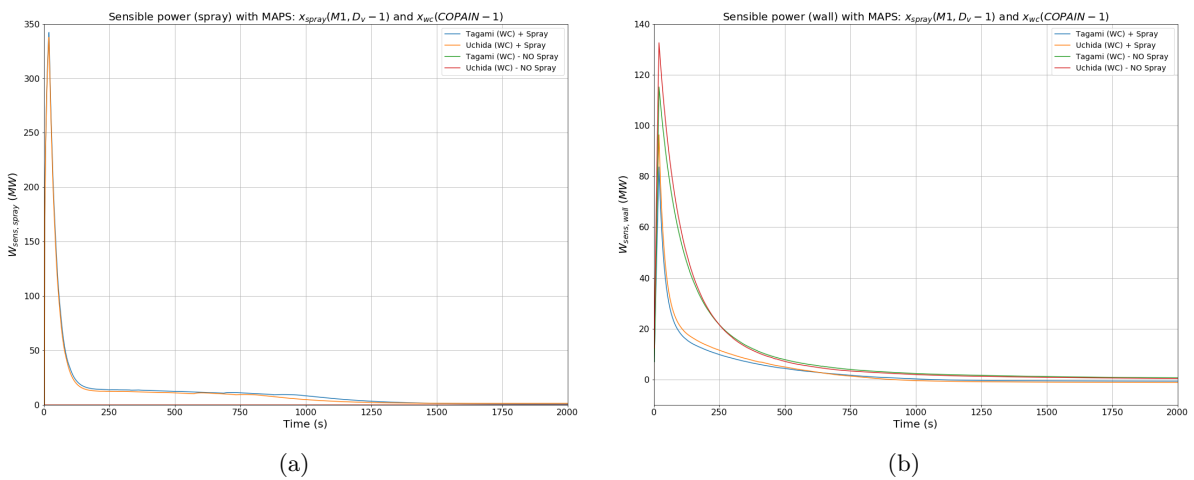


Figure 3.27: Sensible power exchanged due to (a) the spray and to (b) the wall. Use of repartition maps with D_v -1.

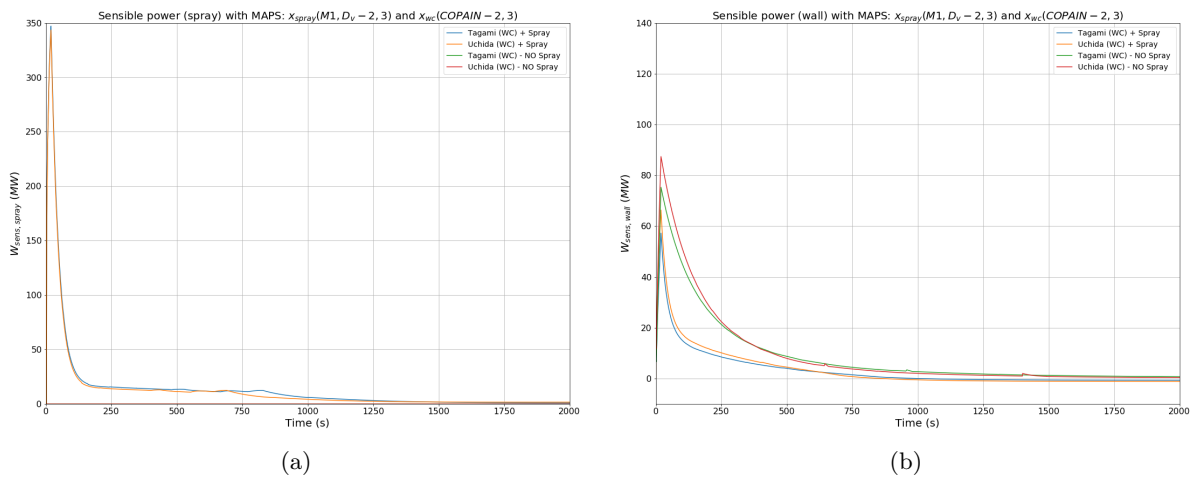


Figure 3.28: Sensible power exchanged due to (a) the spray and to (b) the wall. Use of repartition maps with $D_V-2,3$.

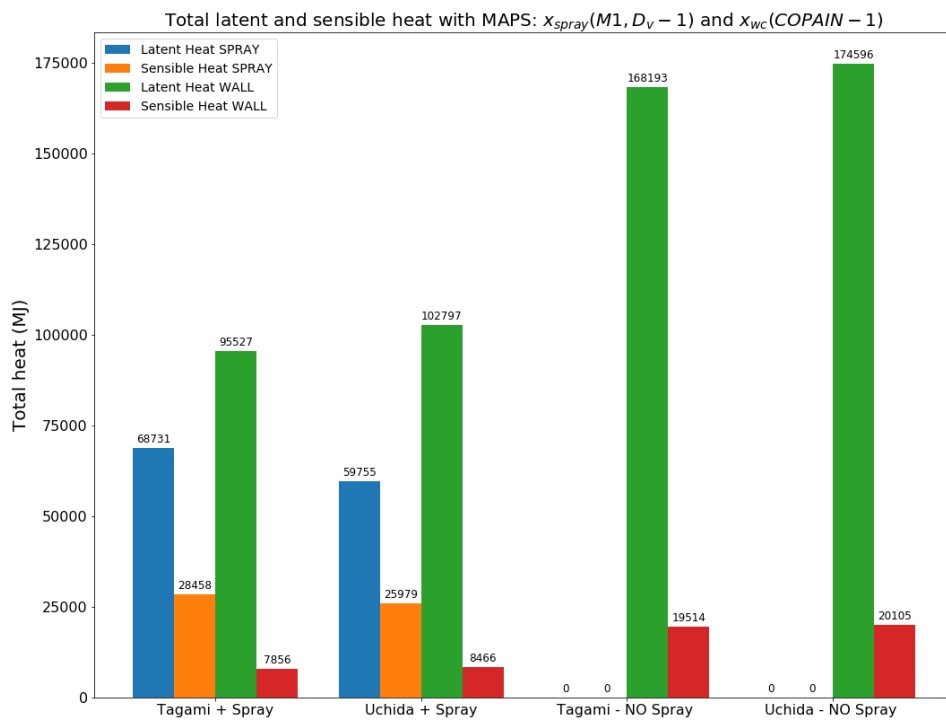


Figure 3.29: Total latent and sensible heat exchanged using the repartition maps with D_V-1 .

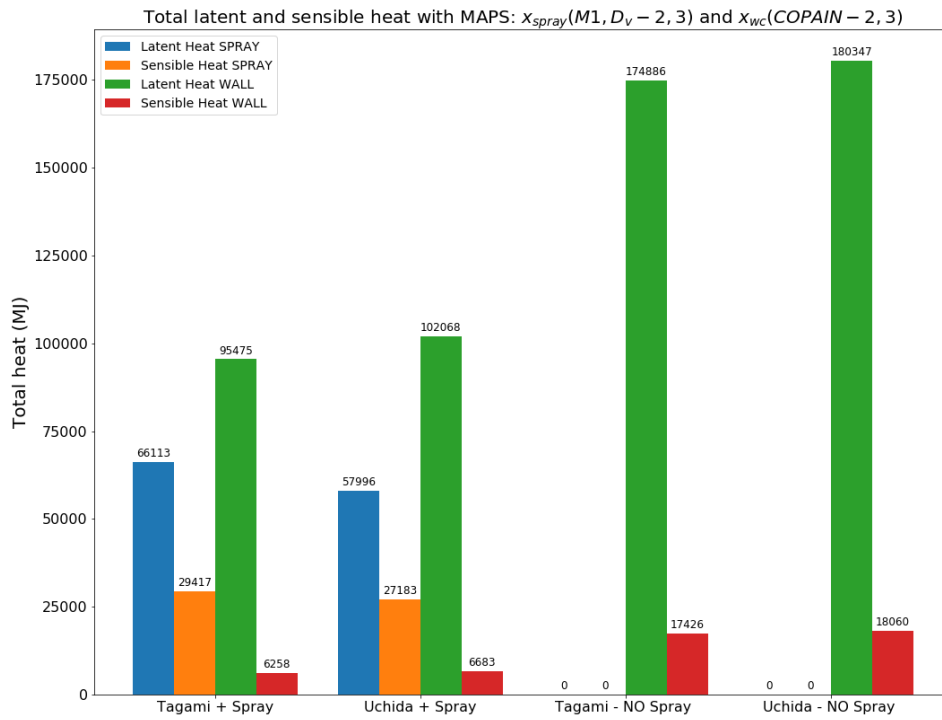


Figure 3.30: Total latent and sensible heat exchanged using the repartition maps with D_v -2,3.

Conclusions

The analysis carried out on the mechanistic models for the Containment Spray System (CSS) in chapter 1 and for the Wall Condensation (WC) in chapter 2 made it possible to assess the Heat and Mass (H&M) transfers between the containment superheated atmosphere and both the spray droplets and the containment walls. It was possible to quantify the ratio between latent and sensible contribution and it was seen that the latent one is almost always higher than the sensible one. For both CSS and WC, the models chosen were carefully validated by reproducing results found in the literature: the *Bestion-Lopez* [3] results for CSS and the *Benteboula-Dabbene: Test-1* [5] results for WC. In addition, experimental data obtained at the IRSN CARAIDAS facility [4] were reproduced for the One-drop model (CSS). Finally, an Uncertainty Quantification (UQ) analysis was carried out on the One-drop model, using the data on the uncertainty of the initial droplet diameter provided in [4]: the analysis showed that the uncertainty about the initial drop diameter produces a larger statistical error for smaller initial diameters ($d_0 \approx 300 \mu\text{m}$) and atmospheric conditions leading to fast vaporization (high total pressure and/or high gas mixture temperature with low relative humidity).

The development of the 0D Containment model in chapter 3 allowed numerical simulations of a Main Steam Line Break (MSLB) in a Pressurized Water Reactor (PWR) to be carried out. The CSS and WC models analyzed in the previous two chapters were effectively coupled to the 0D Containment model and it was therefore possible to assess their ability to mitigate the effects of the accident. It has been shown that, after stopping the steam injection, even the WC (passive mechanism) alone is capable of bringing about a substantial reduction in pressure and temperature in the containment, returning them almost to pre-accidental values after 2000 seconds. As would be expected, the activation of CSS leads to an even faster and more pronounced mitigation effect, except where historical models are used with the conservative 92/8 assumption (subsection 3.3.2), since in this particular case it was observed that the activation of the CSS has a negative effect on the temperature evolution (see figure 3.14).

The assessment of the 0D Containment model proposed in chapter 3 lacks reference data, which would be needed to refine the comparison between the various sub-models applied to describe the H&M exchanges between the superheated atmosphere of the containment, the CSS drops and the containment walls. An interesting perspective for this work could be to further assess the 0D Containment model in relation either with experimental reference data if available (they could not be found in the open literature) and/or with 2D or 3D Computational Fluid Dynamics (CFD) simulations. The 0D Containment model, if proved relevant enough, would provide an attractive basis for uncertainty quantification studies, following the strategy

applied in chapter 1 for the spray sub-model only.

As an additional perspective, further study of the phenomena (and associated physical models) that have been neglected in this work could allow for an even more accurate description and characterisation of the H&M transfers between the superheated atmosphere, the CSS drops and the containment walls. For example, one could study the *Liquid-vapor separation at the break (flashing)*, which is one of the main phenomena governing the evolution of pressure and temperature in the containment (as said in the introduction). In addition, one could study the other forces acting on the drops during their fall (Lift force, Magnus effect, Basset force), the conduction inside the drops and the interaction phenomena between the drops (multiple-drop phenomena like drop-drop collisions). Regarding the WC, one could study the effect of the resistance of the liquid film forming on the walls of the containment. These studies could lead to more precise predictions, but not profoundly different from those obtained in this work.

Finally, a further perspective that could substantially affect the predictions obtained in this work would be to model the heat transfer phenomena along the wall thickness by considering a time-varying wall temperature (instead of considering it constant as done in this work). This can be achieved by applying, for example, a 1D transient heat conduction equation to the wall thickness, with appropriate boundary conditions.

Appendix A

Derivation of mixture model equations

The following is a summary of the approach adopted by the authors in [6] to obtain analytical expressions of the temporal evolution of pressure and temperature, $P(t)$ and $T(t)$, in the containment following a MSLB (eq. 3.48). The case considered is the one where there is only injection of superheated steam into the containment through a breach and no mitigation effect (e.g. CSS activation and/or Wall Condensation), here called *Configuration 0*.

The main assumption of this model is to consider the mixture of air and superheated steam as if it is a perfect gas of superheated steam, hence the name *Mixture model*.

A PWR containment building of volume V is considered, whose initial (pre-accident) pressure and temperature conditions are P_0 and T_0 . The gas mixture is characterised by a ratio of heat capacities at constant pressure and constant volume $\gamma = C_p/C_v$ and a specific enthalpy h given by the relation:

$$h(T) = C_p T + h_0 \quad (\text{A.1})$$

where h_0 is a specific enthalpy reference value.

\dot{M}_{br} and h_{br} are the steam injection mass flow rate and specific enthalpy respectively, assumed constant during the entire injection time interval.

The pressurization of the containment is the result of an enthalpy input by the superheated steam entering the containment through the breach. The containment is therefore an open transient system to which an energy equation in integral form is applied, assuming that all the quantities are uniform in the containment at a time t .

Let's start by writing the following energy balance equation in integral form applied to the containment volume (see [6] for details):

$$\frac{d}{dt} \int_{V(t)} \rho \left(u + \frac{1}{2} v^2 + \Phi \right) dV = \Delta \left[\left(h + \Phi + \frac{1}{2} \frac{\langle v^3 \rangle}{\langle v \rangle} \right) \dot{M} \right] + Q - W \quad (\text{A.2})$$

Assuming that the kinetic and potential energy terms in front of the enthalpy terms can be neglected and that there are no thermal losses through boundaries for the control volume ($Q = 0$), the following equation can be obtained:

$$\frac{d}{dt}(Mh) - V \frac{dP}{dt} = \dot{M}_{\text{br}} h_{\text{br}} \quad (\text{A.3})$$

where M is the gas mixture mass. Considering the specific enthalpy expression A.1 and the perfect gas law, the equation A.3 can be written as follows:

$$\frac{d}{dt}(Mh) = \frac{\gamma}{\gamma - 1} V \frac{dP}{dt} + h_0 \frac{dM}{dt} \quad (\text{A.4})$$

The mass balance equation can be written as:

$$\frac{dM}{dt} = \dot{M}_{\text{br}} \quad (\text{A.5})$$

which gives:

$$\frac{d}{dt}(Mh) = \frac{\gamma}{\gamma - 1} V \frac{dP}{dt} + h_0 \dot{M}_{\text{br}} \quad (\text{A.6})$$

Replacing the term $d(Mh)/dt$ with its expression in the energy equation A.3, one can write:

$$\frac{dP}{dt} = \frac{\gamma - 1}{V} \dot{M}_{\text{br}} (h_{\text{br}} - h_0) \quad (\text{A.7})$$

The analytical expression of the pressure temporal evolution $P(t)$ can be obtained by integrating the equation above:

$$P(t) = \frac{\gamma - 1}{V} (h_{\text{br}} - h_0) \dot{M}_{\text{br}} t + P_0 \quad (\text{A.8})$$

In order to determine the temperature evolution $T(t)$, let's write the perfect gas equation:

$$P(t)V = M(t)C_p \frac{\gamma - 1}{\gamma} T(t) \quad (\text{A.9})$$

Since \dot{M}_{br} is constant, one can write:

$$M(t) = M_0 + \dot{M}_{\text{br}} t \quad (\text{A.10})$$

where M_0 can be obtained from:

$$P_0 V = M_0 C_p \frac{\gamma - 1}{\gamma} T_0 \quad (\text{A.11})$$

Finally, the the analytical expression of the temperature evolution $T(t)$ can be written as follows:

$$T(t) = \frac{P(t)}{\frac{P_0}{T_0} + \dot{M}_{\text{br}} \frac{C_p}{V} \frac{\gamma - 1}{\gamma} t} \quad (\text{A.12})$$

Bibliography

- [1] H. Karwat, J. Bardelay, T. Hashimoto, G. W. Koroll, M. Krause, J. L'Heriteau, P. Lundstroem, A. Notafrancesco, P. Royl, B. Schwinges, et al. Soar on containment thermal-hydraulics and hydrogen distribution-prepared by an oecd/nea group of experts. Technical report, Organisation for Economic Co-Operation and Development-Nuclear Energy Agency, 1999.
- [2] R. Murray and K. E. Holbert. *Nuclear energy: an introduction to the concepts, systems, and applications of nuclear processes*. Elsevier, 2015.
- [3] D. Bestion and T. Lopez. A mechanistic spray model for lumped parameter reactor containment modeling. In *18th International Topical Meeting on Nuclear Reactor Thermal Hydraulics, NURETH 2019*, pages 6551–6563, 2019.
- [4] J. Malet, T. Gelain, S. Mimouni, G. Manzini, S. Arndt, W. Klein-Hessling, Z. Xu, M. Povilaitis, L. Kubisova, Z. Parduba, S. Paci, N. B. Siccama, and M. H. Stempniewicz. Spray Model Validation On Single Droplet Heat And Mass Transfers For Containment Applications – Sarnet-2 Benchmark. *Nureth-14*, 1, 2011.
- [5] S. Benteboula and F. Dabbene. Modeling of wall condensation in the presence of noncondensable light gas. *International Journal of Heat and Mass Transfer*, 151:119313, 2020.
- [6] J. M. Delhaye. Chap 5 : Rappels sur les équations des écoulements monophasiques. In *Thermohydraulique des réacteurs*, chapter 5. EDP sciences, 2013.
- [7] NRC. Interim Staff Position on Environmental Qualification of Safety-Related Electrical Equipment. *Nureg-0588*, 1981.
- [8] R. S. Miller, K. Harstad, and J. Bellan. Evaluation of equilibrium and non-equilibrium evaporation models for many-droplet gas-liquid flow simulations. *International Journal of Multiphase Flow*, 24(6):1025–1055, 1998.
- [9] S. Mimouni, J. S. Lamy, J. Lavieville, S. Guieu, and M. Martin. Modelling of sprays in containment applications with A CMFD code. *Nuclear Engineering and Design*, 240(9):2260–2270, 2010.

-
- [10] S. Marelli and B. Sudret. UQLab: a framework for uncertainty quantification in MATLAB. In *Proc. 2nd Int. Conf. on Vulnerability, Risk Analysis and Management (ICVRAM2014)*, Liverpool, United Kingdom, 2014.
- [11] P. Errante, C. Corre, S. Makhlouf, and Ecole Centrale De Lyon. Uncertainty Quantification for the Eulerian-Lagrangian simulation of evaporating sprays. In *ICLASS 2018*, Chicago, Illinois (USA), 2018.
- [12] S. Marelli and B. Sudret. UQLab user manual – Polynomial chaos expansions. Technical report, Chair of Risk, Safety and Uncertainty Quantification, ETH Zurich, Switzerland, 2019. Report # UQLab-V1.3-104.
- [13] J. C. de la Rosa, A. Escrivá, L. E. Herranz, T. Cicero, and J. L. Muñoz-Cobo. Review on condensation on the containment structures. *Progress in Nuclear Energy*, 51(1):32–66, 2009.
- [14] M. Dehjourian, M. Rahgoshay, R. Sayareh, G. Jahanfarnia, and A. S. Shirani. Effect of Spray System on Fission Product Distribution in Containment During a Severe Accident in a Two-Loop Pressurized Water Reactor. *Nuclear Engineering and Technology*, 48(4):975–981, 2016.

Acknowledgements

I would like to thank very much my supervisors at the ECL-LMFA laboratory, Professor Christophe Corre and Ph. D. Cristina Ghitiu, who have allowed me to carry out this challenging work by guiding and supporting me with the utmost effectiveness and availability. I would also like to thank Professor Cristina Bertani, my supervisor at PoliTO, who effectively followed and supported my work remotely.

Finally, I would like to thank my family and friends for their constant support throughout the years that have brought me to this accomplishment.

